2017

Evaluating Models for Metallic Honeycomb Structures

Ziv Arzt
Lehigh University

Evaluating Models for Metallic Honeycomb Structures

by

Ziv Arzt

Presented to the Graduate and Research Committee

of Lehigh University

in Candidacy for the Degree of

Master of Science

in

Mechanical Engineering and Mechanics

Lehigh University

April 2017

This thesis is accepted and approved in partial fulfilment of the requirements for the degree of Master of Science in Mechanical Engineering.

_____
Date

_____
Prof. Natasha Vermaak, Thesis Advisor

_____
Prof. D. Gary Harlow, Chairperson of
Department of Mechanical Engineering and Mechanics

Acknowledgements

I would first like to thank my advisor Professor Natasha Vermaak for guiding me through my research, and providing excellent feedback and direction. Prof. Vermaak, I really appreciate your support on this work, and I also appreciate the amount of time you have taken to advise me in order to help me develop as a professional. To my parents, Eema and Abba, I cannot thank you enough for the encouragement you have given me while writing this thesis, and for the emotional and financial support you have provided me over my years as a student and scholar. Finally, I would like to thank my roommates for picking me up when I needed a boost, and certainly for distracting me whenever I needed a break over the course of my time at Lehigh.

Contents

List of Tables

List of Figures

Abstract

Sandwich panels with metallic honeycomb cores have been utilized in many industrial applications where structures with high specific modulus or stiffness to weight ratios are required, most notably in the aerospace industry. Sandwich panels with square honeycomb cores have been found to exhibit a slightly higher strength to weight ratio than their more common hexagonal counterparts, and are also easier to manufacture when high core densities are required. The majority of research on square honeycomb sandwich panels has been aimed at characterizing the structure's dynamic blast performance, as well as its response to out-of-plane shear, bending, and in-plane/out-of-plane compression. In this work, several analytical models for the failure of metallic square honeycomb structures under three-point-bending loading are evaluated. Failure modes of interest include face-buckling, face-yielding, core-buckling, and core-yielding. In contrast to traditional models, in which the moment is resisted entirely by the face sheets and the shear is resisted entirely by the core, several alternative analytical models are assessed. These account for the axial stress caused by the bending moment in the core as well as the face sheets, and for the shear in the face sheets. Accounting for the portion of the moment resisted by the core becomes especially important as the relative core density increases. Finite element analysis is used to verify and compare with the analytical models. Post-processing of the finite element models is focused on determining when local yielding and buckling occur in the structure, and on analyzing the effects of local failure on the global force-displacement behavior of the honeycomb structure. A parametric study with a range of honeycomb geometries is conducted in order to assess how accurately the analytical models predict failure. The intent is to develop simplified analytical models that reliably predict the onset of failure for a broad range of loading levels, geometries, and relative densities. These analytical models are then incorporated in structural optimization protocols to aid designers in selecting combinations of materials and geometries under competing performance constraints.

Chapter 1

Introduction

Sandwich structures consist of at least two parallel face sheets, with core sections occupying the spaces between the face sheets. Traditionally, the core section of the sandwich structure is much lighter and less stiff than the face sheets. As a result, sandwich structures are able to exhibit very high strength to weight ratios when compared to uniform plates [2–5]. Recent advances in manufacturing technology have increased the availability of sandwich structures, leading to their wide use in the aerospace industry [6, 7]. Honeycomb structures are a subset of sandwich structures, in which the core section is made up of hollow cells with thin vertical walls. Several types of honeycomb structures are shown in Figure 1.1. Currently, the most widely available types of honeycomb structures are composed of hexagonal core cells. Aluminum and Nomex hexagonal cores can be manufactured at a lower cost than their square and triangular counterparts through the use of an expansion manufacturing process. In the expansion process, thin strips of the core material are stacked, bonded together, and then pulled apart in order to form the hexagonal cell shape [1]. Square and triangular honeycomb cores on the other hand, have traditionally been manufactured by machining and slotting together individual strips of the core material, and then brazing the assembly [1, 8, 9]. Currently, additive manufacturing approaches aimed at expanding design freedom and reducing the production cost of cellular structures are being explored [10–13].

Optimizations involving analytical failure models for various sandwich structures have shown that honeycomb structures are the most weight efficient structure in three-point-bending applications. Furthermore, studies have shown that square honeycomb panels are slightly more weight efficient than hexagonal honeycombs panels [2,14,15]. This thesis will evaluate the assumptions made by traditional analytical models

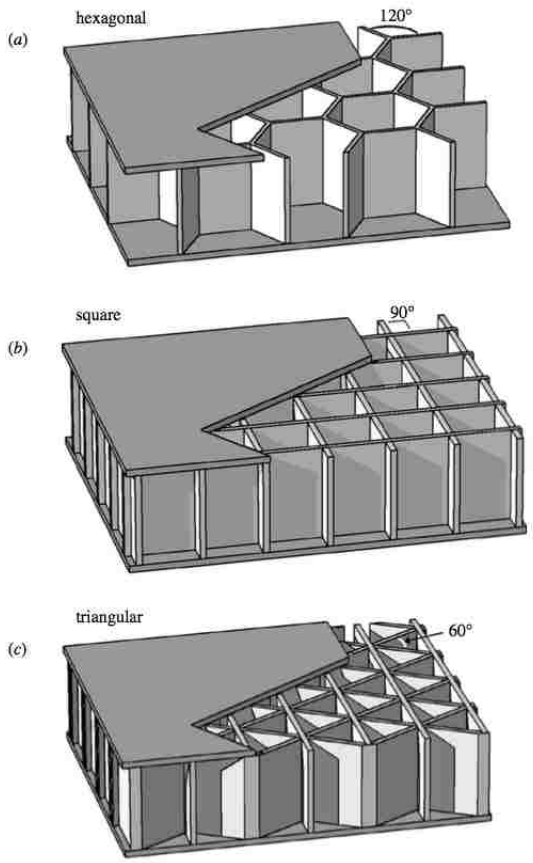

Figure 1.1: Examples of three types of honeycomb sandwich panels: (a) hexagonal honeycomb, (b) square honeycomb and (c) triangular honeycomb [1].

that predict the failure of square honeycomb structures under three-point-bending. The goal is to generate a modified analytical model that more accurately characterizes the failure of square honeycomb sandwich structures under three-point-bending over as broad of a range of geometry and loading as possible. This improved accuracy is critical to the assessment of square honeycomb panels because they are often used in applications where higher relative core densities are required. It is at these higher core densities where the traditional decoupled models become non-conservative. At the same time, the proposed modified model should be tractable: allowing for physical design insight by avoiding unnecessary complexity. The intent is to use the proposed model in optimization protocols to identify promising, near-optimal, structures that can be further fine-tuned with detailed finite element analysis. In order to assess the performance of the models, optimization results for the traditional and proposed modified models will be compared to the results of broad parametric finite element studies.

The proposed analytical model formulated in this work interrogates assumptions commonly made

about the stresses in the honeycomb structure, as well as what constitutes the failure of the structure. Traditional models for square honeycomb structures, under combined shear and bending, decouple the loading condition by assuming that the bending moment is entirely resisted by the face sheets, and the shear is entirely resisted by the core [2, 3, 16]. Furthermore it is often assumed that the shear and axial stress are uniform across the face and core, respectively. While these decoupled models are useful in predicting the strength of honeycomb structures over a broad loading range, it will be shown that they have a tendency to overestimate the strength of the square honeycomb structure. The model proposed in this thesis will use Euler-Bernoulli beam theory in order to account for the sandwich core's resistance to bending and the shear caused by the loading in the core. The proposed model will consider the same four failure modes found in most square honeycomb analysis: face yielding, core yielding, face buckling, and core buckling [2, 3, 16]. However, instead of treating face and core members as simply supported for the buckling criteria, a first step towards accounting for rotational constraints imposed in the structure is proposed in this work. It should be noted that other failure mechanisms such as core indentation failure, explored by Petras and Sutcliffe [17] could be included, but are beyond the scope of this work.

The need to create a more accurate analytical model for square honeycomb structures is motivated by the unique way that the structure is manufactured, as well as the potential applications where a square honeycomb structure would be necessary. It has been shown that the sizing of a square honeycomb panel can be optimized by selecting a geometry that causes at least three of the four failure modes considered to become active [3]. However, when manufacturing constraints, such as minimum thickness for the face sheets and core members are considered, many of the proposed optimum geometries become impractical. As the core of the structure becomes thicker than what is strictly necessary to carry the load, the core begins to play a more active role in resisting the bending moment and restraining the faces from buckling, and the assumptions about the stresses and buckling conditions made by the traditional decoupled model become less valid. In addition, it is important to consider the cases where a square honeycomb panel might be utilized, especially considering its usually high manufacturing cost when compared to a hexagonal honeycomb. The first case is when a very large load must be sustained by the structure. In this case, a hexagonal honeycomb may not be able to withstand the load. For example, hexagonal honeycombs manufactured via expansion processes cannot produce cores with high enough relative density [1], and therefore cannot withstand high shear loads. Ongoing studies are determining the role of additive

manufacturing approaches in the low-cost mass production and use of square and hexagonal honeycomb sandwich structures [10]. The second case where square honeycomb structures may be utilized is when a very low strength to weight ratio is required. As square honeycombs have been shown to be 10-15% more weight efficient than hexagonal core honeycombs, the accuracy of the analytical models predicting structural failure is critical for design decisions.

Chapter 2

Model Geometry and Loading

In this work, a square honeycomb panel under three-point-bending is examined using analytical and finite element approaches. In order to compare the approaches, the geometry of the structure is defined by four unique design variables. For a prescribed load, these design variables can then be optimized in order to minimize structural weight. This section will define the pertinent geometric parameters and present them in non-dimensional form so that structures of different scale can be compared. Finally, non-dimensional weight and strength indexes will be introduced so that the performance of different panels can also be compared.

2.1 Square Honeycomb Panel Geometry

The dimensions for a square honeycomb panel are shown in Figure 2.1. The thicknesses of the face sheet and core materials are denoted as t_f and t_c, respectively. It should be noted that the height of the core, H_c, is measured as the distance between the inner faces of the face sheets. The cell width, L_c, on the other hand, is the distance between the mid-planes of two adjacent core walls. The aspect ratio of the honeycomb cells, ξ is:

$$\xi = \frac{L_c}{H_c}, \tag{2.1}$$

and it will be useful particularly when considering the buckling failure criteria.

In order to completely characterize the geometry of the honeycomb structure, the loading condition

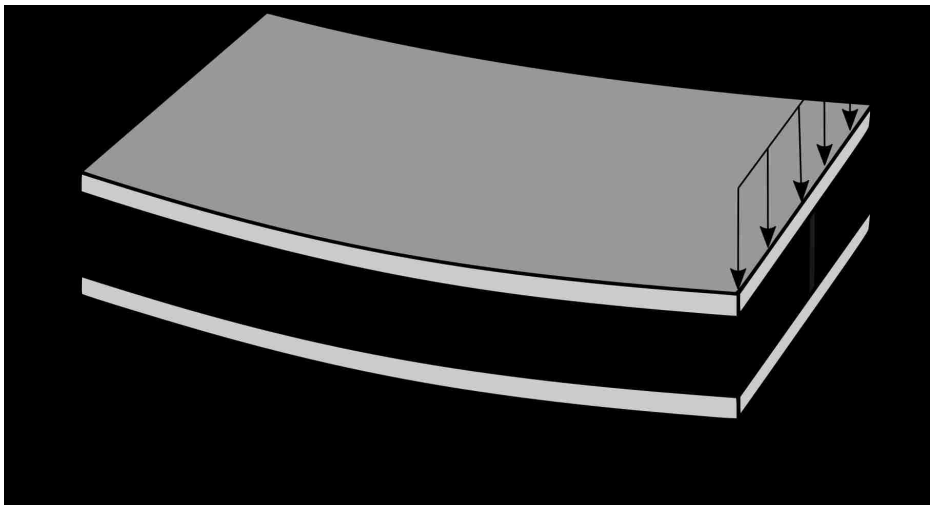

Figure 2.1: Half-symmetry view of square honeycomb panel under three-point-bending loading.

must also be considered. The analytical models presented in this work derive the stresses in a honeycomb panel under combined shear and bending. One way to achieve the combined loading is to subject the panel to a three-point-bend test. A diagram of a three-point-bend test is shown in Figure 2.2. The span of the honeycomb panel, S, is defined as the distance between the two supports. The three-point-bending load is applied as a line load at the middle of the panel, a distance $S/2$ from the left hand support.

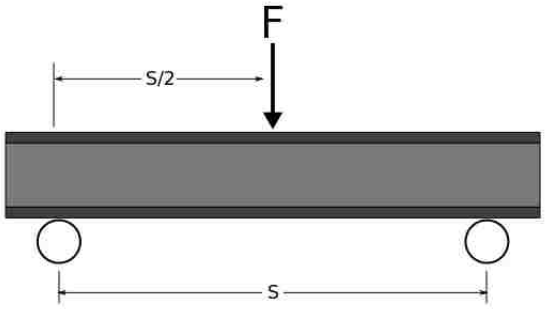

Figure 2.2: Three-point-bending loading.

The finite element results and analytical models both utilize the symmetric loading condition and the cross-sectional symmetry of the square honeycomb panel in order to simplify the analysis. A symmetric section of the panel cross-section of unit cell width is highlighted in Figure 2.3. Note that to simplify the analysis, the symmetric section is defined so that the face sheet extends a distance of $L_c/2$ on either side of the core, making it symmetric about a vertical and horizontal axis.

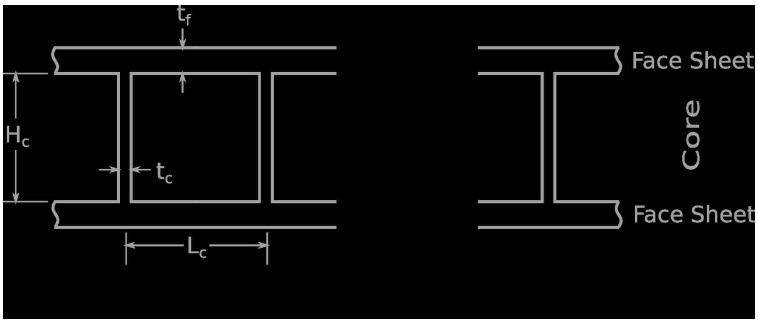

Figure 2.3: Cross-sectional view of honeycomb panel indicating dimensions of honeycomb analysis cell.

2.2 Normalization of Honeycomb Panel Loading

To compare the specific strength or strength to weight ratio of various panel geometries, the dimensions of the structure must be normalized with respect to a characteristic length scale. The characteristic length scale for the loading condition, l, is defined as the ratio of the maximum bending moment per unit width to the maximum shear force per unit width of the panel. The maximum moment in the panel will occur at the load line, a distance $S/2$ from the supports. Figure 2.4 shows a free body diagram for the three-point bend test. Using symmetry and summing the forces in the vertical direction, it is clear that the support reactions will both be equal to one half of the applied shear load. In Figure 2.5, a section-cut is made at the load line in Figure 2.4 in order to determine the internal forces acting on the panel.

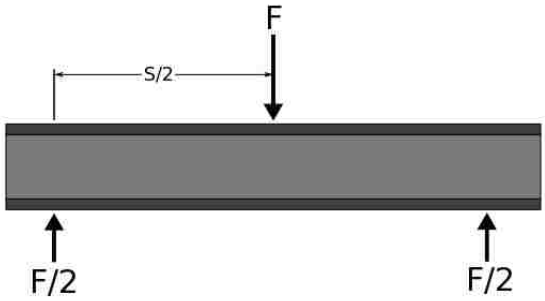

Figure 2.4: Three-point-bending free body diagram.

Summing the moments and the forces in the vertical direction, the maximum internal shear force and bending moment can be determined as follows:

$$V_{max} = \frac{F}{2}, \tag{2.2}$$

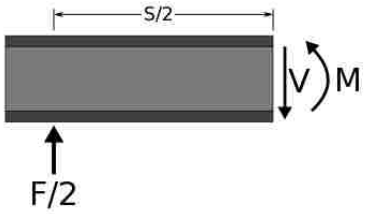

Figure 2.5: Three-point-bending free body diagram with section cut to determine maximum internal forces.

$$M_{max} = \frac{FS}{4}. \tag{2.3}$$

As a result, the characteristic length scale can be expressed:

$$l = \frac{M_{max}}{V_{max}} = \frac{S}{2}. \tag{2.4}$$

It is important to note that in order to compare various honeycomb geometries, F, V and M, are all loads per unit width of the panel.

2.3 Derivation of Non-Dimensional Weight and Performance Indexes

As panels analyzed in this work are, for simplicity, made from a single material, the non-dimensional weight index can be obtained by dividing the total material volume of a given panel by the surface area of the panel, and then dividing again by the characteristic length scale. The non-dimensionality of this parameter can be shown as follows:

$$\Psi = \frac{(Volume)}{(Area)(Length)} = \frac{(Length)^3}{(Length)^3} = Dimensionless. \tag{2.5}$$

Figure 2.6 shows the dimensions of a unit cell of a square honeycomb panel. Accounting for the material removed in order to allow the core sections to fit together, the volume contribution of the core is:

$$\overline{V}_{core} = 2t_c H_c L_c - t_c^2 H_c. \tag{2.6}$$

The subtracted $t_c^2 H_c$ term accounts for the material removed in forming the slots on overlapping core members. As the core sheet thickness is much smaller than the cell width for all practical geometries, the

effect of the removed core material will be neglected in the final formulation of the weight index for the structure.

The volume contribution of the face sheets is:

$$\overline{V}_{face} = 2t_f L_c^2. \tag{2.7}$$

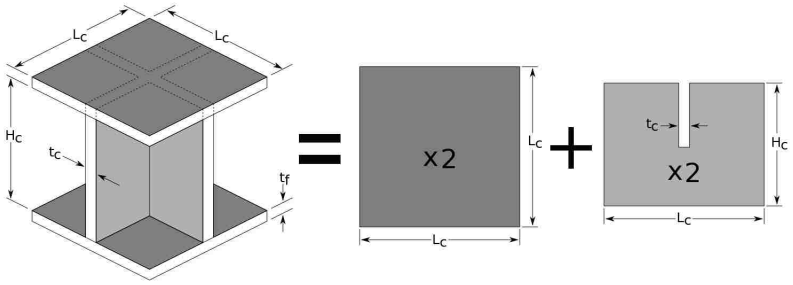

Figure 2.6: Dimensions of square honeycomb unit cell.

Noting that the area of the unit cell is L_c^2, the weight index can be expressed as:

$$\Psi = \frac{\overline{V}_{face}}{L_c^2 l} + \frac{\overline{V}_{core}}{L_c^2 l} = \frac{2t_f}{l} + \frac{2t_c H_c}{L_c l}, \tag{2.8}$$

where the first term accounts for the contribution of the face sheets, and the second term accounts for the contribution of the core.

The pertinent load index, Π, for sandwich panels subject to shear and bending is given by [18] as:

$$\Pi = \frac{V_{max}^2}{EM_{max}}, \tag{2.9}$$

where E is the modulus of elasticity of the panel material. The dimensionality of the load index is:

$$\frac{V^2}{EM} = \frac{(\frac{force}{length})^2}{(\frac{force}{length^2})(\frac{force \cdot length}{length})} = Dimensionless. \tag{2.10}$$

Recalling that the characteristic length scale for the problem is $l = \frac{M_{max}}{V_{max}}$, equation (2.9) can be used to express M and V in terms of Π and l as follows:

$$V = \Pi E l, \tag{2.11}$$

$$M = \Pi E l^2. \tag{2.12}$$

Equations (2.11) and (2.12) will be useful when determining the non-dimensional failure load for the structure in terms of the loading condition and panel geometry. Finally, the displacement at the mid-point of the honeycomb panel can be normalized as:

$$\delta_{norm} = \frac{\delta'}{S}, \tag{2.13}$$

where δ' is the vertical y-displacement at the midpoint of the panel (see Figure 2.1). This term will be used when determining the global force-displacement response of the structure using finite element analysis.

Chapter 3

Derivation of Analytical Models

There are many computational techniques that can be used to analyze the three-point-bending performance of metallic honeycomb structures. Some of these include finite element and homogenization approaches [16, 19–21]. For design purposes, analytical models can provide promising geometries for further development. They may also allow for structural insight and the identification of design guidelines. In this work, analytical models are developed that can be used in concert with more detailed finite element analysis for design tuning.

This work compares a traditional decoupled modeling approach to a more detailed Euler-Bernoulli beam theory based modeling approach. The Euler-Bernoulli model is then simplified to identify a model that balances accuracy with simplicity for analytical structural insight. The simplified Euler-Bernoulli approach is also of interest for efficient optimization purposes.

Although the models make different assumptions about the structural mechanics and stress distributions in the structure, they all consider the same failure modes, and define failure as the onset of plastic yielding or buckling of the face sheet and core members. This chapter will first define the failure modes and present the common assumptions that are shared between the models. Based on these definitions and descriptions, the traditional decoupled model, a proposed Euler-Bernoulli model, and a simplified Euler-Bernoulli model will be presented. Finally, failure mechanism maps will be used in order to compare the models.

3.1 Failure Modes and Common Assumptions

Four failure criteria will be considered in all of the models: core yielding, face yielding, core buckling, and face buckling. In this work, less common failure modes such as core indentation and face sheet delamination, will be ignored for the following reasons. In order to neglect core indentation as a failure mode, it is assumed that the three-point-bending supports have a radius large enough to distribute the load over a sufficiently large area so as to not cause local yielding. In order to neglect the face delamination failure mode, it is assumed that the braze joint between the core and face sheets is at least as strong as the base material for the structure.

3.1.1 Yielding

A von Mises yield criterion will be used, and it will be assumed that the structure has failed when yielding first occurs at any point in the structure. The face sheets and core members are thin relative to the other dimensions of the structure, so a plane stress condition is assumed. In cases of plane stress, where there are shear stresses and only one axial stress component, the von Mises criterion simplifies to:

$$\sigma^2 + 3\tau^2 = \sigma_Y^2, \tag{3.1}$$

where σ is the axial stress at the location of interest, τ is the shear stress, and σ_Y is the yield stress for the material.

3.1.2 Buckling

For the buckling failure criteria, it will be assumed that the face and core sections of the structure are made up of many smaller thin rectangular plates. The boundaries of these plates are determined by the intersections of the face sheets and core members. As a result of the geometry of the structure, local plates on the face sheets have dimensions $L_c \times L_c$, while the local plates in the core section have dimensions $L_c \times H_c$. Local plates for the face sheet and core section are highlighted in Figure 3.1. Structural failure is considered to have occurred when any local plate in either the face sheet or core section of the structure has buckled.

Thin rectangular plates subjected to axial stress will buckle when the maximum axial stress at the

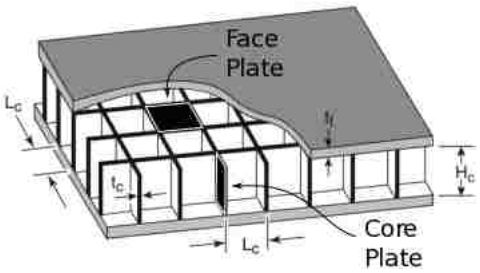

Figure 3.1: Location of face and core plates used in buckling criteria.

mid-plane of the plate reaches a certain threshold stress, σ_{cr}, where σ_{cr} is defined by [22]:

$$\sigma_{cr} = K_b \frac{\pi^2 E}{12(1-\nu^2)} \left(\frac{t}{b}\right)^2. \tag{3.2}$$

Similarly, if the plate is subjected to a shear load, it will buckle when the shear stress reaches a certain threshold stress, τ_{cr}, where τ_{cr} is defined by [22]:

$$\tau_{cr} = K_s \frac{\pi^2 E}{12(1-\nu^2)} \left(\frac{t}{b}\right)^2. \tag{3.3}$$

In equations (3.2) and (3.3), K_b and K_s are buckling coefficients, E is the elastic modulus of the material, ν is Poisson's ratio for the material, t is the thickness of the plate, and b is the length of the loaded edges of the plate. Diagrams for both loading cases are shown in Figure 3.2. The buckling coefficient is dependent on the boundary conditions and aspect ratio of the plate.

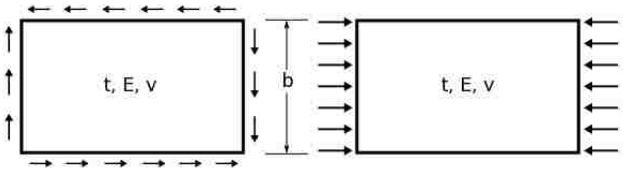

Figure 3.2: Loading of rectangular plate under uniform shear (left), and uniform compressive stress (right).

If a thin plate is subjected to combined axial and shear loading, it will not buckle as long as [22]:

$$\left(\frac{\sigma_{max}}{\sigma_{cr}}\right)^2 + \left(\frac{\tau_{max}}{\tau_{cr}}\right)^2 \leq 1. \tag{3.4}$$

In each model, failure loads corresponding to each of the failure modes will be derived in terms of

parameters relating to the structure geometry and loading conditions. Globally, the structure is considered to have failed when the lowest of the four failure loads is applied to the structure. It is important to note that because all failure loads are calculated independently, there will be no coupling of the failure modes. As a result, conservative assumptions must be made when developing the models.

3.2 Traditional Decoupled Modeling Approach

Typical decoupled models for the failure of sandwich structures under three-point-bending assume that the bending moments are entirely resisted by the face sheets, and the shear load is entirely resisted by the core. Furthermore, in this work it will be assumed that the axial stress caused by the moments is uniformly distributed across the face sheets, and the shear stress caused by the shear load is uniformly distributed across the core. Figure 3.3 schematically depicts the stresses that act on a panel of unit cell width as dictated by the decoupled model.

Decoupled models for sandwich panels are commonly presented in the literature, and are also commonly used in industry to provide a first estimate for sandwich panel strength. For example, Allen [23] presented decoupled models for sandwich panels and described cores of low stiffness as “antiplane,”, meaning that they are unable to support a compressive load. Wicks and Hutchinson [2] used decoupled models in order to optimize truss and honeycomb core panels under three-point-bending.

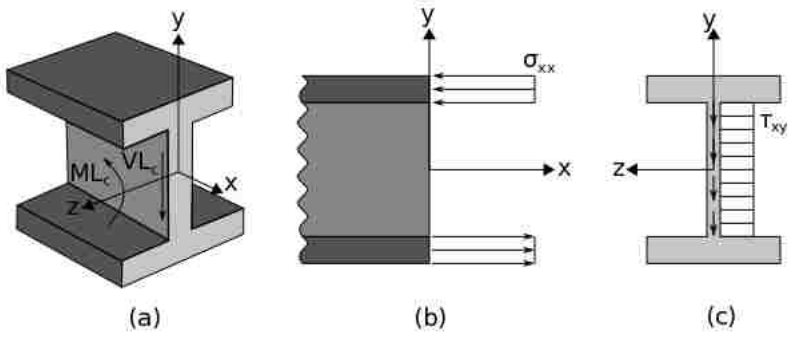

Figure 3.3: Internal force and moment acting on honeycomb panel (a), and resulting axial (b) and shear (c) stress distributions given by the decoupled model.

For convenience, Tables 3.1 and 3.2 summarize the stresses and non-dimensional failure constraints predicted by the decoupled model. A full derivation of the decoupled model failure loads is included in Appendix A.

Axial stress in face sheets	Axial stress in core	Shear stress in face sheets	Shear stress in core
$\sigma_f = \frac{M}{t_f(H_c+t_f)}$	0	0	$\tau_c = \frac{VL_c}{t_c H_c}$

Table 3.1: Face sheet and core stresses for decoupled model.

Face Yielding	Core Yielding	Face Buckling	Core Buckling
$\Pi \frac{l^2}{\epsilon_Y t_f(H_c+t_f)} \leq 1$	$\Pi \frac{\sqrt{3}L_c l}{\epsilon_Y t_c H_c} \leq 1$	$\Pi \frac{3l^2(1-\nu^2)L_c^2}{t_f^3(H_c+t_f)\pi^2} \leq 1$	$\Pi \frac{12lL_c(1-\nu^2)H_c}{K_s t_c^3 \pi^2} \leq 1$

Table 3.2: Failure constraints for decoupled model.

The advantages of the decoupled model are that it results in simple failure constraint calculations, and that it allows for a clear understanding of how the geometry of the square honeycomb structure determines which failure mode is active. For example, given a loading condition and a maximum allowable core height, a designer could use the decoupled model to immediately determine the appropriate range for material yield strain. The simple relationships in the decoupled model also make it apparent that:

- increasing the face sheet thickness decreases the likelihood of face sheet yielding and buckling
- increasing the core member thickness decreases the likelihood of core yielding and buckling
- increasing the cell width increases the likelihood of face sheet and core buckling

While these relationships are intuitive and are present in all of the analytical models, they are most clearly identified by examining the failure constraints proposed by the traditional decoupled model.

The clarity and simplicity provided by the decoupled model are a result of the assumptions made in the analysis. While the simplifying assumptions are often warranted, important structural trends can be lost. For example, with the decoupled model assumptions, the face sheet yielding criterion does not depend on the cell width. In reality, however, reducing the cell width will increase the cross-sectional area moment of inertia of the structure, which will increase both its strength and stiffness. Although the traditional decoupled model is an excellent starting point for design, a more detailed model with modified assumptions about the structural mechanics can be more accurate and useful for optimizing the geometry of the structure, without resorting to full finite element calculations.

3.3 Euler-Bernoulli Coupled Modeling Approach

Instead of relying on the traditional decoupled model to characterize the structure, a more detailed model using Euler-Bernoulli beam theory can be implemented to more accurately predict failure. Although the Euler-Bernoulli analysis adds a significant amount of complexity to the model, it is appropriate because the resulting failure constraints can still be expressed in closed form, and thus the model can still be easily implemented in an optimization scheme. The Euler-Bernoulli approach has also previously been applied in modeling sandwich structures with diamond prismatic cores [15].

The Euler-Bernoulli model predicts axial and shear stresses both in the face sheets and the core, and thus the level of stress in the structure is "coupled" with the dimensions of both the face sheets and the core. One way to think of this from a design point of view is to consider a structure that fails due to core yielding. If the traditional decoupled model is applied, the only way to increase the strength of the structure is to increase the amount of material comprising the core. This is the only option because core yielding is assumed to be caused solely by the shear load, which is uniformly carried by the core. If a "coupled" model is considered, however, the strength of the structure could also be improved by increasing the amount of material in the face sheets. Increasing the amount of material in the face sheets will decrease axial stress in the core (a stress component that was not previously captured by the decoupled model), which will increase the core yielding load and thus increase the strength of the structure. It is not, however, obvious whether dedicating more material to the face sheets or the core will be the most optimal way to strengthen the structure, and in fact, the most optimal solution will likely be a combination of the two. The advantage of using a more detailed "coupled" model in this way is that an optimization scheme can be used to identify the choice that may no longer be intuitive to a designer.

One of the key assumptions of Euler-Bernoulli beam theory is that the panel under three-point-bending acts as one beam, and that all cross-sections remain plane and perpendicular to the longitudinal axis of the beam during deformation [24]. In many sandwich panel analyses [23], these assumptions are not relevant because the core is much less stiff than the face sheets, causing shear deformation which is not allowed to occur in the Euler-Bernoulli model.

In justifying the use of the Euler-Bernoulli model, it is important to consider the square honeycomb geometry, as well as the scope of this work. First of all, the traditional slotting and brazing process used to manufacture square honeycomb structures lends itself well to producing structures of relatively high

core density, when compared to other honeycomb structures. In addition, this work assumes that the core and face sheets have equivalent material properties, which is not the case when foam core structures or hexagonal Nomex core structures are considered. Both of these assumptions result in square honeycomb cores that will be much stiffer than the cores of other structures, allowing them to carry a significant axial load and making them less likely to deform under shear. Finally, the Euler-Bernoulli model is appropriate in the context of this work because only the strength of the structure, and not the stiffness, is being considered. Although the Euler-Bernoulli model is not a conservative measure in determining the stiffness of the structure [23], it is however conservative in determining the loads that will cause initial structural failure by yielding or buckling [15].

Figure 3.4 depicts the axial and shear stress distributions across the face sheets and core predicted by the Euler-Bernoulli "coupled" model. The axial stress is linearly distributed across the entire cross-section. The shear stress is parabolically distributed across the core and linearly distributed across the face sheets. In accordance with the plane stress condition assumed for the face sheets and core, the xy shear component will be neglected in the face sheets, and the xz shear component will be neglected in the core. This assumption is justified because the in-plane shear components are several orders of magnitude higher than the out of plane components.

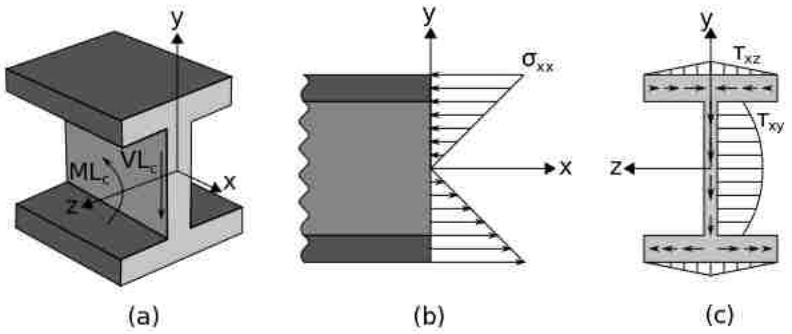

Figure 3.4: Internal force and moment acting on honeycomb strip (a), and resulting axial (b) and shear (c) stress distributions given by the Euler-Bernoulli "coupled" model.

As shown in Figure 3.4, the shear stress evaluated at the edges of the face sheets in the honeycomb panel of unit cell width is equal to zero. When considering the shear flow through a much wider honeycomb panel, this assumption still holds true because of the symmetry of the panel. In other words, the zero value of shear at the edges of the unit cell width panel occurs not necessarily because the edges are assumed to be free surfaces, but because there is no shear flow between adjacent symmetrical unit cells when the panel

is loaded. This concept is schematically illustrated in Figure 3.5.

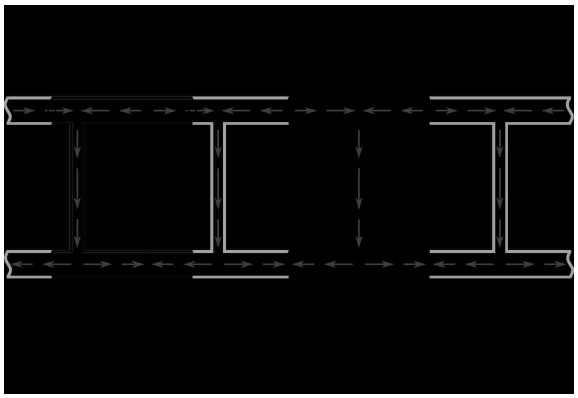

Figure 3.5: Schematic of shear flow through the cross-section of honeycomb panel under three-point-bending.

In order to calculate the axial stress in the face sheets and core, the area moment of inertia of the honeycomb panel of unit cell width must be determined. The contribution of the core moment of inertia can be expressed as:

$$I_{zz,c} = \frac{1}{12} t_c H_c^3. \tag{3.5}$$

Using the parallel axis theorem, the contribution from one of the face sheets is:

$$I_{zz,f} = \frac{1}{12} L_c t_f^3 + t_f L_c \left(\frac{H_c + t_f}{2} \right)^2, \tag{3.6}$$

where the first term accounts for the stiffness of a face sheet about its local centroidal axis (shown in Figure 3.6), and the whole expression accounts for the stiffness of the face sheet about the centroidal axis of the entire structure. For practical square honeycomb geometries however, t_f is very small in comparison to L_c, and the first term in equation (3.6) can be neglected. Neglecting the first term in equation (3.6) and accounting for the contribution of both face sheets, the moment of inertia of the entire cross-section of a square honeycomb analysis cell can be approximated as:

$$I_{zz} = \frac{1}{12} t_c H_c^3 + t_f L_c \frac{(H_c + t_f)^2}{2}. \tag{3.7}$$

The axial stress in a given cross-section due to bending is:

$$\sigma_{xx} = \frac{-M_z y}{I_{zz}}, \tag{3.8}$$

where M_z is the moment applied to the cross section and y is the distance from the point of interest on the cross-section to the neutral axis, which is shown in Figure 3.6. The maximum axial stress in the core can then be found by evaluating y at $H_c/2$. The maximum axial stress for the face sheets can be found by evaluating y at $H_c/2 + t_f$. The average axial stress in the face sheets can be found by evaluating y at $(H_c + t_f)/2$.

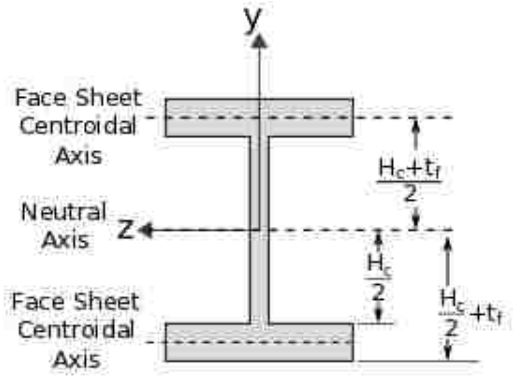

Figure 3.6: Locations of face sheet centroidal and neutral axes.

The total moment applied to the honeycomb panel of unit cell width is ML_c. As a result, the total moment being applied to the cross section is: $M_z = ML_c$.

Recognizing that the total moment applied to the panel of unit cell width is $M_z = ML_c$, and evaluating y at $H_c/2$, the maximum axial stress in the core is:

$$\sigma_{max,core} = \frac{ML_c H_c}{2I}. \tag{3.9}$$

Evaluating y at $H_c/2 + t_f$, the maximum axial stress in the face sheets is:

$$\sigma_{max,face} = \frac{ML_c\left(\frac{H_c}{2} + t_f\right)}{I}. \tag{3.10}$$

Evaluating y at $(H_c + t_f)/2$, the axial stress at the mid-plane of the face sheets is:

$$\sigma_{mid-plane,face} = \frac{ML_c\,(H_c + t_f)}{2I}. \tag{3.11}$$

The shear stress for an Euler-Bernoulli beam is calculated as [24]:

$$\tau = \frac{VQ}{It}. \tag{3.12}$$

In equation (3.12), τ is the shear stress at a point of interest, V is the total shear load acting on the beam, Q is the first moment of the area of the portion of the cross-section above the point of interest with respect to the neutral axis, I is the area moment of inertia for the entire cross-section, and t is the cross-sectional thickness at the point of interest.

The first moment of area, Q, is defined:

$$Q = \int y dA = \sum \overline{y} A. \tag{3.13}$$

When the cross-section is made up of simple shapes, as is the case for the square honeycomb, the summation expression on the right is more convenient to use. For each shape, $\overline{y}$ is the distance between the axis of interest (in this case, the neutral axis) and the centroid of the shape, and A is the area of the shape.

When evaluating the shear in the core, the moment of area above the point of interest has a core contribution and a face contribution, as shown in Figure 3.7. When evaluating the shear at a position y on the cross-section, the distance between the neutral axis and the centroid of the contributing core area is $\overline{y}_c = y + \frac{\frac{H_c}{2} - y}{2} = \frac{H_c}{4} + \frac{y}{2}$. The distance between the neutral axis and the centroid of the contributing face sheet area is, $\overline{y}_f = \frac{H_c + t_f}{2}$. The areas of the core and face sheet contributions are $(\frac{H_c}{2} - y)t_c$ and $t_f L_c$, respectively.

Using equation (3.13) and simplifying the expression, the moment of area above a section-cut on the core becomes:

$$\begin{aligned} Q_c &= \left(\frac{H_c}{4} + \frac{y}{2}\right)\left(\frac{H_c}{2} - y\right) t_c + \frac{H_c + t_f}{2} t_f L_c \\ &= \left(\frac{H_c^2}{8} + \cancel{\frac{yH_c}{4}} - \cancel{\frac{yH_c}{4}} - \frac{y^2}{2}\right) t_c + \frac{H_c + t_f}{2} t_f L_c \end{aligned}$$

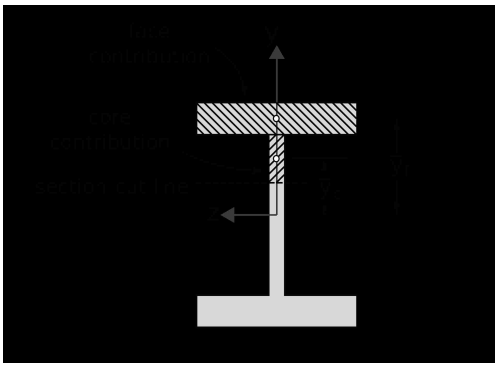

Figure 3.7: First moment of area for a core cross-section-cut.

$$= \frac{t_c}{2}\left(\frac{H_c^2}{4} - y^2\right) + \frac{1}{2}t_f L_c \left(H_c + t_f\right). \tag{3.14}$$

Noting that the thickness of the section-cut is t_c, and the total shear load acting on the cross-section is VL_c, equation (3.12) can be used to express the shear stress in the core:

$$\tau_c = \frac{VL_c}{2I}\left[\frac{H_c^2}{4} - y^2 + L_c\frac{t_f}{t_c}\left(H_c + t_f\right)\right]. \tag{3.15}$$

The core shear attains its maximum at the neutral axis of the panel $(y = 0)$, and is minimized at the interface between the core and face sheets $\left(y \pm \frac{H_c}{2}\right)$.

For a section-cut made through the face sheet, the area moment of inertia only has a face contribution, as shown in Figure 3.8. For a section-cut made a distance z from the vertical axis, the distance between the centroid of the contributing face sheet area and the neutral axis is $\overline{y}_f = \frac{H_c + t_f}{2}$. The contributing face sheet area is, $A_f = t_f\left(\frac{L_c}{2} - z\right)$. Using equation (3.13), the first moment of area for a face sheet section-cut can be expressed:

$$Q_f = t_f\left(\frac{H_c + t_f}{2}\right)\left(\frac{L_c}{2} - z\right). \tag{3.16}$$

Noting that the thickness of the face sheet section-cut is t_f, and the total shear load acting on the cross-section is VL_c, equation (3.12) can be used to express the shear stress in the core:

$$\tau_f = \frac{VL_c}{I}\left(\frac{H_c + t_f}{2}\right)\left(\frac{L_c}{2} - z\right). \tag{3.17}$$

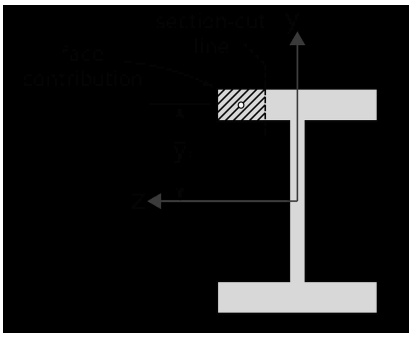

Figure 3.8: First moment of area for a face sheet cross-section-cut.

The face shear attains its maximum at the interface with the longitudinal core members ($z = 0$), and is minimized midway through the core cells $\left(z \pm \frac{L_c}{2}\right)$.

As the axial stress in the core increases away from the neutral axis and the shear stress decreases, it is unclear where the maximum von Mises stress in the core will occur. As a result, the core yield criterion will need to be checked for all positions along the core. Using the von Mises yield criterion from equation (3.1), as well as the core axial stress and shear stress given by equations (3.8) and (3.15), respectively, the core yield criterion can be formulated:

$$\left(\frac{ML_c y}{I}\right)^2 + 3\left\{\frac{VL_c}{2I}\left[\frac{H_c^2}{4} - y^2 + L_c\frac{t_f}{t_c}\left(H_c + t_f\right)\right]\right\}^2 \leq \sigma_Y^2, \quad \text{for } 0 \leq y \leq \tfrac{H_c}{2}. \tag{3.18}$$

Using equation (2.12) for M, (2.11) for V, Hooke's law for σ_Y, and simplifying, the core yield criterion is:

$$\left(\frac{\Pi \cancel{E} l^2 L_c y}{I}\right)^2 + 3\left\{\frac{\Pi \cancel{E} l L_c}{2I}\left[\frac{H_c^2}{4} - y^2 + L_c\frac{t_f}{t_c}\left(H_c + t_f\right)\right]\right\}^2 \leq \left(\cancel{E}\epsilon_Y\right)^2, \quad \text{for } 0 \leq y \leq \tfrac{H_c}{2} \tag{3.19}$$

Dividing both sides by ϵ_Y^2 and factoring out $\left(\frac{\Pi l^3 L_c}{\epsilon_Y I}\right)^2$ allows the equation to be expressed in non-dimensional form:

$$\left(\frac{\Pi l^3 L_c}{\epsilon_Y I}\right)^2 \left\{\left(\frac{y}{l}\right)^2 + \frac{3}{4}\left[\frac{H_c^2}{4l^2} - \frac{y^2}{l^2} + \frac{L_c}{l^2}\frac{t_f}{t_c}\left(H_c + t_f\right)\right]^2\right\} \leq 1, \quad \text{for } 0 \leq y \leq \tfrac{H_c}{2}. \tag{3.20}$$

Noting that the core will first yield when the expression on the left hand side is maximized across the range

of y, the core yielding criterion for the coupled model can be expressed:

$$\left(\frac{\Pi l^3 L_c}{\epsilon_Y I}\right) \max_{0\leq y\leq \frac{H_c}{2}} \left\{ \left(\frac{y}{l}\right)^2 + \frac{3}{4}\left[\frac{1}{4}\left(\frac{H_c}{l}\right)^2 - \left(\frac{y}{l}\right)^2 + \left(\frac{L_c}{l}\right)\left(\frac{t_f}{t_c}\right)\frac{(H_c+t_f)}{l}\right]^2 \right\}^{\frac{1}{2}} \leq 1. \quad (3.21)$$

In the Euler-Bernoulli "coupled" model, the maximum von Mises stress in the face sheet occurs at the top surface of the face sheet, directly over the longitudinal core members. Referring to Figure 3.4, the corresponding zy coordinates on the cross-section of a panel of unit cell width are $(0, \frac{H_c}{2}+t_f)$. Using the von Mises criterion (3.1), and equations (3.10) and (3.17) to evaluate the axial and shear stress, the face sheet yielding criterion can be expressed:

$$\left[\frac{ML_c\left(\frac{H_c}{2}+t_f\right)}{I}\right]^2 + 3\left[\frac{VL_c}{I}\left(\frac{H_c+t_f}{2}\right)\left(\frac{L_c}{2}\right)\right]^2 \leq \sigma_Y^2. \quad (3.22)$$

Using equation (2.12) for M, (2.11) for V, Hooke's law for σ_Y, and simplifying, the core yield criterion is:

$$\left[\frac{\Pi \cancel{E} l^2 L_c\left(\frac{H_c}{2}+t_f\right)}{I}\right]^2 + 3\left[\frac{\Pi \cancel{E} l L_c}{I}\left(\frac{H_c+t_f}{2}\right)\left(\frac{L_c}{2}\right)\right]^2 \leq \left(\cancel{E}\epsilon_Y\right)^2. \quad (3.23)$$

Dividing both sides by ϵ_Y^2, factoring out $\left(\frac{\Pi l^3 L_c}{\epsilon_Y I}\right)^2$, and taking the square root of both sides allows the face yield criterion to be expressed in non-dimensional form:

$$\left(\frac{\Pi l^3 L_c}{\epsilon_Y I}\right)\left\{\left[\frac{\frac{H_c}{2}+t_f}{l}\right]^2 + \frac{3}{4}\left[\left(\frac{H_c+t_f}{2l}\right)\left(\frac{L_c}{l}\right)\right]^2\right\}^{\frac{1}{2}} \leq 1. \quad (3.24)$$

In order to simplify the face buckling calculation while maintaining a conservative approach, the shear stress in the face sheets will be treated as constant, with a value equal to the maximum face sheet shear stress. The axial stress will be evaluated at the mid-plane of the face sheet, as presented in equation (3.11). Recalling that the face is composed of plates with dimension $L_c \times L_c$, the critical axial stress and shear stress can be calculated using equations (3.2) and (3.3):

$$\sigma_{cr} = K_b \frac{\pi^2 E}{12(1-\nu^2)}\left(\frac{t_f}{L_c}\right)^2, \quad (3.25)$$

$$\tau_{cr} = K_s \frac{\pi^2 E}{12(1-\nu^2)} \left(\frac{t_f}{L_c}\right)^2. \tag{3.26}$$

Using equation (3.4), the face buckling constraint is:

$$\left[\frac{6ML_c^3\left(H_c+t_f\right)\left(1-\nu^2\right)}{EIK_b\pi^2 t_f^2}\right]^2 + \left[\frac{3VL_c^4\left(1-\nu^2\right)\left(H_c+t_f\right)}{EIK_s\pi^2 t_f^2}\right]^2 \leq 1. \tag{3.27}$$

Using equation (2.12) for M, (2.11) for V, the face buckling criterion becomes:

$$\left[\frac{6\Pi\cancel{E}l^2L_c^3\left(H_c+t_f\right)\left(1-\nu^2\right)}{\cancel{E}IK_b\pi^2 t_f^2}\right]^2 + \left[\frac{3\Pi\cancel{E}lL_c^4\left(1-\nu^2\right)\left(H_c+t_f\right)}{\cancel{E}IK_s\pi^2 t_f^2}\right]^2 \leq 1. \tag{3.28}$$

Factoring out the term $\left[\frac{6\Pi L_c^3\left(H_c+t_f\right)\left(1-\nu^2\right)l^2}{I\pi^2 t_f^2}\right]^2$ leads to:

$$\left[\frac{6\Pi L_c^3\left(H_c+t_f\right)\left(1-\nu^2\right)l^2}{I\pi^2 t_f^2}\right]^2 \left[\left(\frac{1}{K_b}\right)^2 + \left(\frac{L_c}{2K_s l}\right)^2\right] \leq 1. \tag{3.29}$$

Taking the square root of both sides yields the final expression for the face buckling criterion:

$$\Pi\frac{3\left(1-\nu^2\right)}{\pi^2}\frac{L_c^3\left(H_c+t_f\right)l^2}{It_f^2}\left[\left(\frac{1}{K_b}\right)^2 + \left(\frac{L_c}{2K_s l}\right)^2\right]^{\frac{1}{2}} \leq 1, \tag{3.30}$$

where for a simply supported square plate with uniform axial and shear loads, $K_b = 4$, and $K_s = 9.35$ (see equation (A.10)).

Just like the face buckling criterion, the core buckling condition is simplified by assuming that that the shear stress in the core is constant with a value equal to the maximum value predicted by the Euler-Bernoulli "coupled" model. Recalling that the core is composed of plates with dimension $L_c \times H_c$, equations (3.2) and (3.3) can be used to calculate the critical axial and shear stress for the core buckling criteria:

$$\sigma_{cr} = K_b \frac{\pi^2 E}{12(1-\nu^2)} \left(\frac{t_c}{H_c}\right)^2, \tag{3.31}$$

$$\tau_{cr} = K_s \frac{\pi^2 E}{12(1-\nu^2)} \left(\frac{t_c}{H_c}\right)^2. \tag{3.32}$$

Using equation (3.9) for the maximum axial stress in the core, equation (3.15) evaluated at $y = 0$ for the

shear stress in the core, and equation (3.4) for buckling under a combined shear and axial load, the core buckling criterion can be expressed:

$$\left[\frac{12\left(1-\nu^2\right)ML_cH_c^3}{2EIK_b\pi^2t_c^2}\right]^2+\left\{\frac{12\left(1-\nu^2\right)VL_cH_c^2}{2EIK_s\pi^2t_c^2}\left[\frac{H_c^2}{4}+L_c\frac{t_f}{t_c}\left(H_c+t_f\right)\right]\right\}^2\leq 1. \tag{3.33}$$

Using equation (2.12) for M, (2.11) for V, the core buckling criterion becomes:

$$\left[\frac{6\left(1-\nu^2\right)\Pi\cancel{E}l^2L_cH_c^3}{\cancel{E}IK_b\pi^2t_c^2}\right]^2+\left\{\frac{6\left(1-\nu^2\right)\Pi\cancel{E}lL_cH_c^2}{\cancel{E}IK_s\pi^2t_c^2}\left[\frac{H_c^2}{4}+L_c\frac{t_f}{t_c}\left(H_c+t_f\right)\right]\right\}^2\leq 1. \tag{3.34}$$

Factoring out the term $\left[\frac{6\Pi L_cH_c^2\left(1-\nu^2\right)l^3}{I\pi^2t_c^2}\right]^2$ leads to:

$$\left[\frac{6\Pi L_cH_c^2\left(1-\nu^2\right)l^3}{I\pi^2t_c^2}\right]^2\left\{\frac{1}{K_b^2}\left(\frac{H_c}{l}\right)^2+\frac{1}{K_s^2}\left[\left(\frac{H_c}{2l}\right)^2+\frac{L_c}{l}\frac{t_f}{t_c}\frac{\left(H_c+t_f\right)}{l}\right]^2\right\}\leq 1. \tag{3.35}$$

Taking the square root of both sides yields the final expression for the core buckling criterion:

$$\Pi\frac{6\left(1-\nu^2\right)}{\pi^2}\frac{L_cH_c^2l^3}{It_c^2}\left\{\frac{1}{K_b^2}\left(\frac{H_c}{l}\right)^2+\frac{1}{K_s^2}\left[\frac{1}{4}\left(\frac{H_c}{l}\right)^2+\left(\frac{L_c}{l}\right)\left(\frac{t_f}{t_c}\right)\frac{\left(H_c+t_f\right)}{l}\right]^2\right\}^{\frac{1}{2}}\leq 1. \tag{3.36}$$

Unlike the face plates which are always square for the structure, the aspect ratio of the core plates changes with the geometry of the structure. Equation (A.10) can still be used to evaluate K_s. K_b is given by [22]:

$$K_b=\begin{cases}23.9, & \text{if } \xi\geq 2/3,\\ \left(\frac{\pi}{4\xi}\right)^2\frac{\left[1+\xi^2\right]\left[1+4\xi^2\right]\left[1+9\xi^2\right]}{\left\{\left[1+\xi^2\right]^2\left(\frac{6}{25}\right)^2+\left[1+9\xi^2\right]^2\left(\frac{2}{9}\right)^2\right\}^{\frac{1}{2}}}, & \text{if } \xi<2/3,\end{cases} \tag{3.37}$$

where ξ is the cell aspect ratio, given by equation (2.1).

3.4 Simplifications to the Euler-Bernoulli "Coupled" Approach

The level of complexity introduced by the "coupled" Euler-Bernoulli approach can be reduced by making simplifications to the model that are appropriate within the context of the square honeycomb structure.

In particular, the role of the shear stress in the face sheets and the shear stress distribution across the core will be examined. Simplifying the Euler-Bernoulli "coupled" model also allows for a more efficient optimization protocol, and for the relationships between the design variables and failure constraints to be more clearly identified.

Figure 3.9a shows the contribution of the shear stress to the von Mises stress in the face sheets. H_c was fixed at one tenth of the panel span for the plot, but it was found that the results are relatively insensitive to H_c. As the square cell size L_c, increases, the shear stress makes up a larger portion of the von Mises stress. A non-dimensional cell width of $L_c/l = 0.4$ is required for the shear stress to constitute at least 10% of the von Mises stress. However this value of L_c/l represents an extreme case because it reduces the entire span of the structure to only 5 cells. The implication is that for practical honeycomb geometries, the shear stress in the face sheets does not play a significant enough role to warrant the complexity it adds to the model.

Comparison of the decoupled model and Euler-Bernoulli "coupled" model in Figure 3.9 also shows that the parabolic shear stress distribution in the core can be replaced with a uniform distribution in order to simplify the model. Figure 3.9b uses the decoupled model results in order to normalize the minimum and maximum core shear stresses predicted by the Euler-Bernoulli "coupled" model. The structure is assumed to be cuboidal ($L_c = H_c$), and a range of face sheet and core thicknesses are shown. As the core member thickness to face sheet thickness ratio t_c/t_f increases, the minimum shear stress decreases and the maximum shear stress increases. However, neither deviate far from the decoupled model, with a non-dimensional value of 1.0 in Figure 3.9b. Increasing the face-sheet-thickness-to-cell-width ratio t_f/L_c has the effect of decreasing both the minimum and maximum shear relative to the decoupled model results. This trend results from the fact that the decoupled model does not account for the shear load supported by the face sheets. In Figure 3.9b, the minimum shear stress is of more concern than the maximum because it occurs at the top and bottom of the core member, where yielding most often first occurs. Thus, simplifying the parabolic Euler-Bernoulli shear stress distribution by using a uniform distribution is a conservative measure. With a uniform shear stress distribution, the von Mises stress no longer needs to be sampled across the entire core in order to determine the maximum, which significantly reduces computation time.

The stresses that result from the simplified Euler-Bernoulli "coupled" model are summarized in Table 3.3. Equation (3.8) from the Euler-Bernoulli "coupled" model derivation is used to evaluate the axial

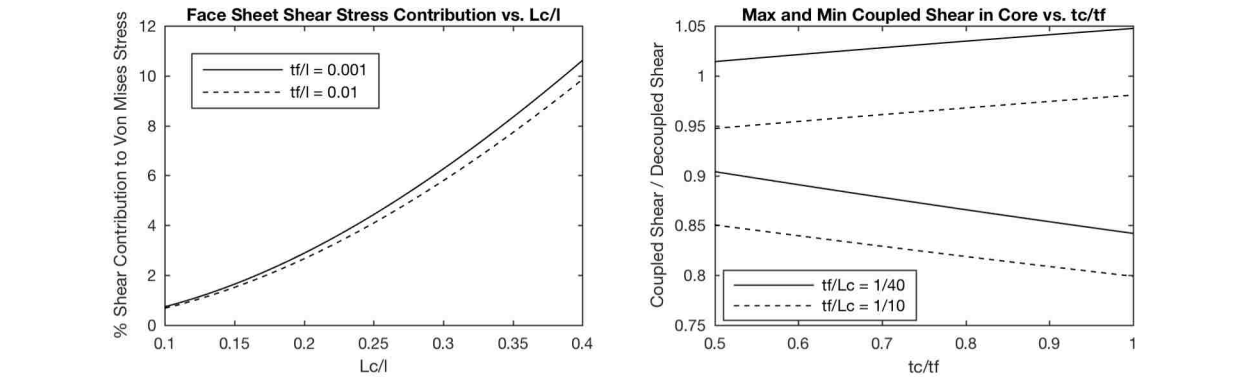

Figure 3.9: (a) Shear stress contribution to the von Mises stress in the face sheet, and (b) minimum and maximum cross-sectional core shear values normalized by the decoupled model results (b). The analysis in (a) assumes a cell height of $l/20$, and (b) assumes a cuboidal ($H_c = L_c$) structure.

stress in the face sheets and core, and equation (A.3) from the decoupled model derivation is used to evaluate the shear stress in the face sheets. The corresponding stresses are shown on the honeycomb unit cell in Figure 3.10.

Axial stress in face sheets	Axial stress in core	Shear stress in face sheets	Shear stress in core
$\sigma_f = \frac{-ML_c y}{I}$	$\sigma_c = \frac{-ML_c y}{I}$	0	$\tau_c = \frac{VL_c}{t_c H_c}$

Table 3.3: Face sheet and core stresses for simplified Euler-Bernoulli model.

As the simplified Euler-Bernoulli model neglects the shear stress in the face sheets, only one axial stress component is present, and the face sheets will yield when the axial stress exceeds the yield stress. Evaluating σ as the maximum axial stress in the face sheets given by equation (3.10), using Hooke's law to set $\sigma_Y = E\epsilon_Y$, using equation (2.12) for M, and dividing through by $E\epsilon_Y$, the face yielding criterion can be expressed:

$$\Pi \frac{l^2 L_c \left(\frac{Hc}{2} + t_f\right)}{I\epsilon_Y} \leq 1. \tag{3.38}$$

The shear stress in the core given by equation (A.3) and the maximum axial stress in the core given by equation (3.9) can be used in the von Mises yield criterion (3.1) in order to define the core yield criterion

Figure 3.10: Internal force and moment acting on honeycomb cell (a), and resulting axial (b) and shear (c) stress distributions given by the simplified Euler-Bernoulli "coupled" model.

for the simplified coupled model:

$$\frac{M^2 L_c^2 H_c^2}{4I^2} + 3\frac{V^2 L_c^2}{t_c^2 H_c^2} \leq \sigma_Y^2. \tag{3.39}$$

Using Hooke's law to set $\sigma_Y = E\epsilon_Y$, dividing through by $E\epsilon_Y$, using equation (2.11) for V, and using equation (2.12) for M, the core yield criterion becomes:

$$\frac{\Pi^2 l^2 L_c^2}{\epsilon_Y^2}\left[\frac{l^2 H_c^2}{4I^2} + \frac{3}{t_c^2 H_c^2}\right] \leq 1. \tag{3.40}$$

Multiplying through by $\frac{l^4}{l^4}$ in order to non-dimensionalize the terms in equation (3.40) and taking the square root of both sides allows the core yielding criterion to be expressed:

$$\Pi\frac{L_c}{\epsilon_Y l}\sqrt{\frac{l^6 H_c^2}{4I^2} + \frac{3l^4}{t_c^2 H_c^2}} \leq 1. \tag{3.41}$$

As only the axial stress is accounted for in the face sheets, the calculation of the face sheet buckling failure constraint is similar to that of the decoupled model. Using the axial stress at the mid plane of the face sheets given by equation (3.11), and substituting $K_b = 4$, $b = L_c$, and $t = t_f$ into equation (3.2), the face sheet buckling criterion is:

$$\frac{M L_c \left(H_c + t_f\right)}{2I} \leq \frac{\pi^2 E}{3\left(1-\nu^2\right)}\left(\frac{t_f}{L_c}\right)^2. \tag{3.42}$$

Using equation (2.12) for M, and dividing both sides by the right hand term gives the final expression for the face sheet buckling criterion:

$$\Pi \frac{l^2 L_c^3 \left(H_c + t_f\right)}{2 I t_f^2} \frac{3\left(1-\nu^2\right)}{\pi^2} \leq 1. \tag{3.43}$$

As the simplified Euler-Bernoulli model predicts both shear and axial stress components in the core, the combined buckling equation (3.4) can be used to formulate the core buckling criterion. Substituting equations (3.11), (A.3) and (3.25) into equation (3.4), the core buckling criterion can be expressed:

$$\left(\frac{M L_c H_c}{2I}\right)^2 \left(\frac{12\left(1-\nu^2\right) H_c^2}{K_b \pi^2 E t_c^2}\right)^2 + \left(\frac{V L_c}{t_c H_c}\right)^2 \left(\frac{12\left(1-\nu^2\right) H_c^2}{K_s \pi^2 E t_c^2}\right)^1 \leq 1, \tag{3.44}$$

where K_b can be evaluated using equation (3.37) and K_s can be evaluated using equation (A.10). Substituting equations (2.12) and (2.11) in for M and V, the core buckling failure criterion becomes:

$$\Pi \frac{L_c 12\left(1-\nu^2\right) H_c}{\pi^2 t_c^2} \left[\frac{l^4 H_c^4}{4 I^2 K_b^2} + \frac{l^2}{t_c^2 K_s^2}\right]^{\frac{1}{2}}. \tag{3.45}$$

For the remainder of this work, the simplified Euler-Bernoulli "coupled" model will be referred to as the *proposed model*. Stresses and failure constraints for the decoupled model, Euler-Bernoulli "coupled" model, and proposed model are shown in Tables 3.4 and 3.5. In Table 3.5, K_b and K_s can be evaluated using equations (3.37) and (A.10), respectively. Also, it should be noted that the terms on left hand sides of the inequalities are referred to as *failure constraint activity levels*. A failure mode is considered to be activated if its corresponding failure constraint activity level is equal to one.

	Decoupled Model	Euler-Bernoulli "Coupled" Model	Proposed Model
σ_f	$\frac{M}{t_f(H_c+t_f)}$	$\frac{-ML_cy}{I}$	$\frac{-ML_cy}{I}$
σ_c	0	$\frac{-ML_cy}{I}$	$\frac{-ML_cy}{I}$
τ_f	0	$\frac{VL_c}{I}\left(\frac{H_c+t_f}{2}\right)\left(\frac{L_c}{2}-z\right)$	0
τ_c	$\frac{VL_c}{t_cH_c}$	$\frac{VL_c}{2I}\left[\frac{H_c^2}{4}-y^2+L_c\frac{t_f}{t_c}\left(H_c+t_f\right)\right]$	$\frac{VL_c}{t_cH_c}$

Table 3.4: Face sheet and core stresses for all analytical models.

	Decoupled Model	Euler-Bernoulli "Coupled" Model	Proposed Model
Face Yielding	$\Pi\frac{l^2}{\epsilon_Y t_f(H_c+t_f)} \leq 1$	$\Pi\frac{l^3L_c}{\epsilon_Y I}\sqrt{\left(\frac{\frac{H_c}{2}+t_f}{l}\right)^2+\frac{3}{4}\left[\left(\frac{H_c+t_f}{2l}\right)\left(\frac{L_c}{l}\right)\right]^2} \leq 1$	$\Pi\frac{l^2L_c\left(\frac{Hc}{2}+t_f\right)}{I\epsilon_Y} \leq 1$
Core Yielding	$\Pi\frac{\sqrt{3}L_cl}{\epsilon_Y t_cH_c} \leq 1$	$\left(\frac{\Pi l^3L_c}{\epsilon_Y I}\right)\max\limits_{0\leq y\leq\frac{H_c}{2}}\sqrt{\left(\frac{y}{l}\right)^2+\frac{3}{4}\left[\frac{1}{4}\left(\frac{H_c}{l}\right)^2-\left(\frac{y}{l}\right)^2+\left(\frac{L_c}{l}\right)\left(\frac{t_f}{t_c}\right)\frac{\left(H_c+t_f\right)}{l}\right]^2} \leq 1$	$\Pi\frac{L_c}{\epsilon_Y l}\sqrt{\frac{l^6H_c^2}{4I^2}+\frac{3l^4}{t_c^2H_c^2}} \leq 1$
Face Buckling	$\Pi\frac{3l^2(1-\nu^2)L_c^2}{t_f^3(H_c+t_f)\pi^2} \leq 1$	$\Pi\frac{3\left(1-\nu^2\right)}{\pi^2}\frac{L_c^3\left(H_c+t_f\right)l^2}{It_f^2}\sqrt{\left(\frac{1}{K_b}\right)^2+\left(\frac{L_c}{2K_sl}\right)^2} \leq 1$	$\Pi\frac{l^2L_c^3\left(H_c+t_f\right)}{2It_f^2}\frac{3\left(1-\nu^2\right)}{\pi^2} \leq 1$
Core Buckling	$\Pi\frac{12lL_c(1-\nu^2)H_c}{K_st_c^3\pi^2} \leq 1$	$\Pi\frac{6\left(1-\nu^2\right)}{\pi^2}\frac{L_cH_c^2l^3}{It_c^2}\sqrt{\frac{1}{K_b^2}\left(\frac{H_c}{l}\right)^2+\frac{1}{K_s^2}\left[\frac{1}{4}\left(\frac{H_c}{l}\right)^2+\left(\frac{L_c}{l}\right)\left(\frac{t_f}{t_c}\right)\frac{\left(H_c+t_f\right)}{l}\right]^2} \leq 1$	$\Pi\frac{L_c12\left(1-\nu^2\right)H_c}{\pi^2t_c^2}\sqrt{\frac{l^4H_c^4}{4I^2K_b^2}+\frac{l^2}{t_c^2K_s^2}}$

Table 3.5: Failure constraints for all analytical models.

3.5 Comparison of Analytical Model Results

Up to this point, the differences between the proposed and decoupled models have been explained, but it is unclear how the models compare when predicting structural failure. One way to compare the models is to construct failure maps. Failure maps for sandwich structures with honeycomb and diamond prismatic cores have been previously developed by Petras and Sutcliffe [25], and Valdevit et al. [15]. The failure maps presented in this work are similar to those constructed by Valdevit et al., because the structural weight for each map is held constant.

The following section presents failure maps for the decoupled and proposed models in Figures 3.11-3.12. As there are many design variables related to geometry and loading, failure maps are restricted to cases where constant weight is imposed for ease of understanding. Holding both the non-dimensional weight Ψ and cell height H_c constant allows for the failure map to be visualized in two dimensional space. The face sheet thickness t_f is varied along the x-axis, and the core thickness t_c is varied along the y-axis. As a result of the weight and cell height being held constant, the cell width L_c can be calculated as a function of t_f and t_c. As t_f and t_c are increased, L_c increases in order to respect the constant structural weight constraint.

In the failure maps presented in Figures 3.11-3.12, two independent geometric parameters, t_c/l and t_f/l, are varied while H_c/l is fixed at 0.2 and the weight index is held at 0.035. Over this range of t_c/l and t_f/l, the boundaries of failure mechanisms, or the transitions between failure mechanisms are shown by solid black lines. At these lines, two or more failure constraint activity levels from Table 3.5 have values of unity, indicating multiple active failure mechanisms. On either side of these failure boundaries, only one mechanism is active in a region. The darkened region around the failure mechanism borders represents conditions where two or three failure modes are at least 90% active (see Table 3.5). Superimposed over the failure mechanism maps are contours of constant load.

Some key results are highlighted by the decoupled model failure map in Figure 3.11. As the core sheet thickness t_c is increased, the cell width L_c of the structure increases, and the structure is prone to face buckling. For smaller face sheet thicknesses t_f, the structure is more prone to core buckling. As the face sheet thickness t_f is decreased beyond a certain level, the face sheets are no longer capable of supporting the bending moment, and face yielding becomes more likely. If the face sheets are sufficiently thick and the structure is not at risk of face or core buckling, then core yielding failure mode is active.

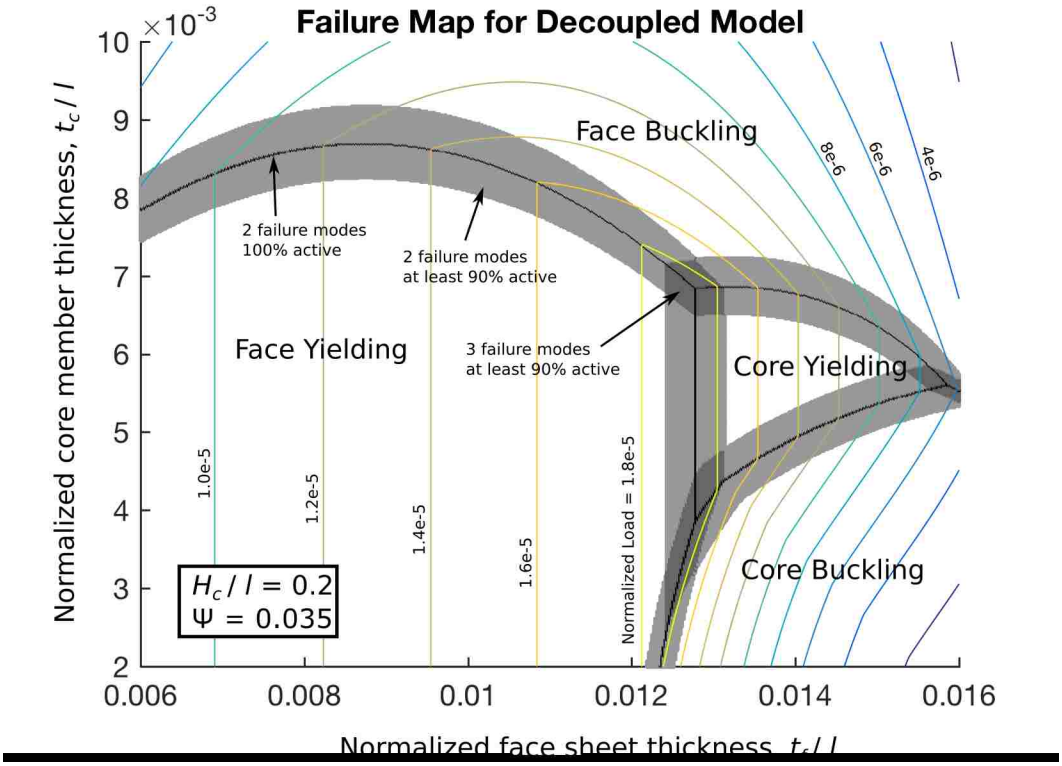

Figure 3.11: Constant weight failure map for decoupled model.

The failure zones on the proposed model map (Figure 3.12) differ significantly from the zones on the decoupled model map. Most notably, the core buckling and yielding zones are expanded because the axial stress in the core is accounted for by the proposed model (see Table 3.4). In addition, the shaded area indicating zones where multiple failure modes are close to being active, between the core and face yielding failure regimes, is larger for the proposed model. The enlarged shaded area is a result of the "coupled" effects of the model. For example, consider a point at the intersection of the face and core yielding regimes for both models. As the face sheet thickness is increased, the face sheet area for the cross-section of the structure increases. At the same time, the distance between the top of the face sheet and top of the core also increases. For the proposed model, these two effects compete against each other in determining what failure mode is active. Increasing the face sheet cross-sectional area allows for the axial load to be distributed over a larger area, reducing the chance of face yielding. As a linear axial stress distribution is predicted, increasing the distance between the top of the core and the outer surface of the face sheet also increases the difference between the maximum face sheet and core axial stresses. The increased difference between the face sheet and core axial stress causes the face sheet yielding mode

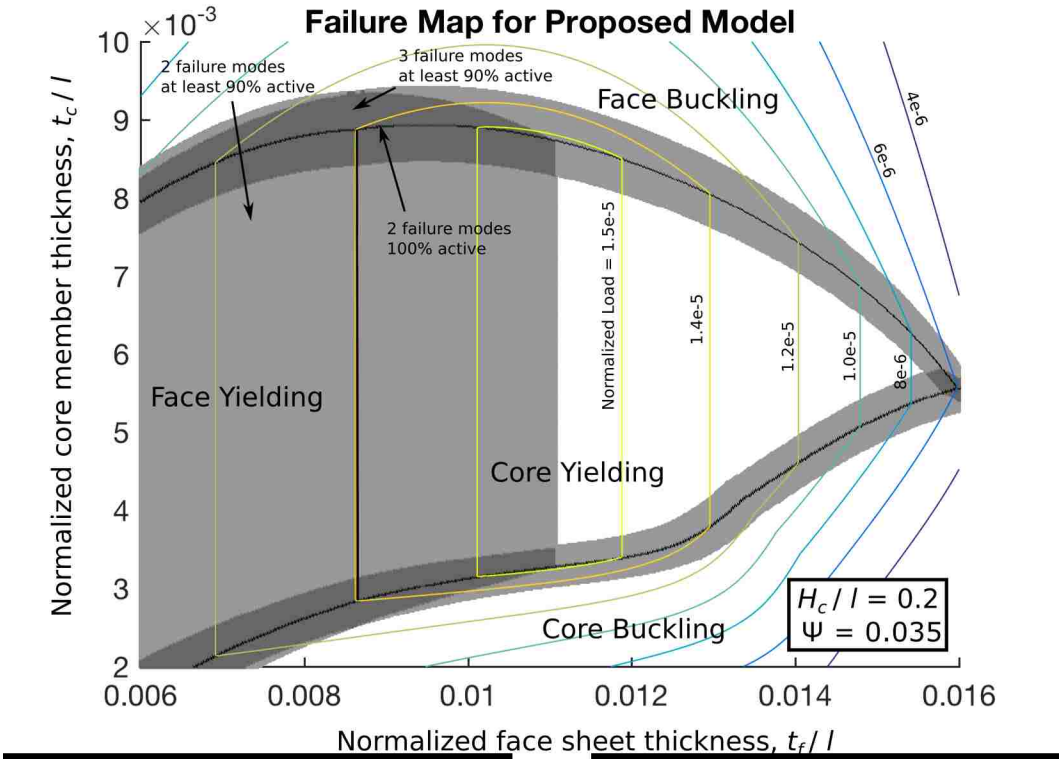

Figure 3.12: Constant weight failure map for proposed model.

to remain at an almost active level for a significant portion of the core yielding regime. In contrast, the decoupled model does not account for the core's resistance of the bending moment, and thus the effect of the difference in the maximum face sheet and core axial stress is not captured. As a result, the decoupled model predicts a sharper transition from face yielding to core yielding dominated failure as the face sheet thickness t_f is increased.

The models also show significant differences in terms of which structural geometry can support the largest load. The decoupled model predicts a maximum non-dimensional load of roughly 1.8×10^{-5}, while the proposed model predicts a maximum non-dimensional load of 1.5×10^{-5}. The decoupled model also predicts optimal face sheet thicknesses that are larger than those predicted by the proposed model for the same non-dimensional weight index. The "coupled" nature of the proposed model is also demonstrated in the determination of where the largest load-bearing geometries lie, in comparison to the decoupled model. For the decoupled model, the optimal geometry is at the intersection of the face and core yielding zones. This is because the face yielding failure mode is independent of the core thickness, and the core yielding failure mode is independent of the face sheet thickness. For the proposed model, the optimal

geometry is in the middle of the core yielding regime. Even though core yielding is the only active failure mode, further decreasing the face sheet thickness will not result in a more efficient structure, because the area moment of inertia of the structure would be reduced.

Chapter 4

Comparison With Finite Element Results

In order to compare the analytical models presented in this work, it is important to recognize that while the predicted failure modes are the same for all of the models, the behavior of the structure after and during failure may be different. For example, the traditional decoupled model assumes that the bending moment is entirely resisted by the face sheets, and that the resulting normal stress is evenly distributed across the face sheets. Under these assumptions, as the structure is loaded and the normal stress exceeds the yield stress, the cross-section will no longer be able to support any additional moment, and a sudden collapse failure mechanism will occur. The proposed model, on the other hand, predicts a linear stress distribution across the face sheets and core. When the face yielding failure criterion for the model is met and the outer surfaces of the face sheets yield, the unyielded portion of the face sheets and core will continue to resist the internal bending moment. The result will not be a sudden structural collapse, but rather a gradual decrease in stiffness until the structure eventually collapses when the entire cross-section has yielded.

Finite element analysis (FEA) is a useful tool in verifying analytical results, however it can be difficult to determine the precise point at which failure occurs. One approach is to compare the peak load that the panel is able to sustain from the finite element results to the analytically predicted failure load. This comparison can be problematic because the post-buckling strength and post-initial-yielding stiffness of the panels may cause the FEA peak load to be higher than the failure loads identified by the analytical models. Valdevit et al. [15] address this issue by analytically approximating the post-buckling strength of the plates making up a diamond prismatic core honeycomb structure, but they acknowledge that such approximations are only valid when yielding failure modes are not active. As the analytical models in this work are used to

optimize the panel geometry, both buckling and yielding failure modes will likely be active for the panels of interest. As a result, in this work, simple approximations for post-buckling strength are not utilized in the analytical models, and new approaches for characterizing failure in the finite element model will be explored.

4.1 Finite Element Model

Reduced integration four node shell elements (S4R) were used to construct the model in the commercial finite element package ABAQUS. A honeycomb panel of unit cell width, with two half-cells on either side was modeled. Quarter symmetry was utilized in order to reduce the size of the model. The symmetry conditions were applied along the face coinciding with the load line at the midspan of the panel, and along one of the sides of the panel, as shown in Figure 4.1. In order to simulate a panel of infinite width, a generalized plane strain condition was applied to the nodes along side of the panel without the symmetry constraint. The generalized plane strain boundary condition constrains all of the nodes along the side of the panel to have the same displacement in the z-direction. The span of the panel and support roller diameter were selected in accordance with ASTM guidelines, as 150 mm and 25 mm, respectively [26]. The support rollers were modeled as rigid analytical surfaces in contact with the panel. Hard contact with a friction coefficient of 0.02 was used in the ABAQUS model. In order to simplify the analysis, the load was modeled by controlling the displacement of the line of nodes on the top face sheet at the midspan of the panel. Linear elastic-perfectly-plastic material properties $E = 70$ GPa, $\sigma_Y = 490$ MPa and $\nu = 0.3$ were used in order to model a typical high strength aluminum. A representative python job file is given in Appendix B.

A mesh convergence study was run in order to determine the appropriate mesh size for the model. The model geometry was selected so that all four failure modes are active, with $H_c/l = 0.103$, $L_c/l = 0.094$, $t_f/l = 0.0041$ and $t_c/l = 0.0019$. In order to accurately capture the buckling failure modes it is important that there are enough elements per unit cell width and height. The model was meshed with rectangular elements with an aspect ratio as close as possible to unity. Element side lengths ranging from $L_c/5$ to $L_c/40$ were tested, and a comparison of the force vs. displacement results are shown in Figure 4.2.

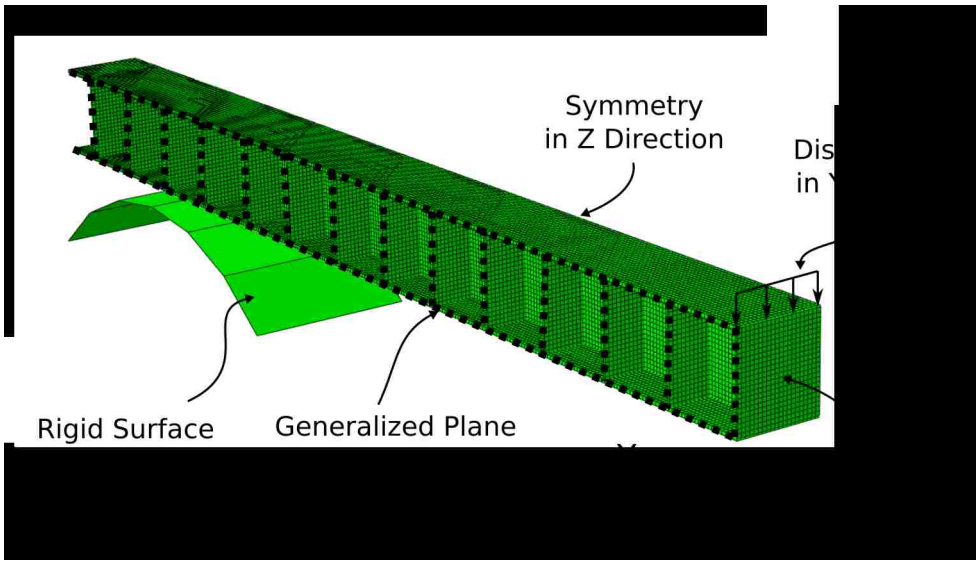

Figure 4.1: Boundary conditions and mesh size used in finite element model.

The percent error in a measured value is defined:

$$\%Error = \frac{x_{measured} - x_{accepted}}{x_{accepted}} \times 100. \tag{4.1}$$

Taking the peak load for the model with the most refined mesh as the accepted value, the error in the peak loads for all of the less refined meshes can be calculated. A precent error comparison in Figure 4.3 shows how the peak load decreases as the mesh is refined. Based on Figures 4.2 and 4.3, an element width of $L_c/20$ was chosen as sufficiently accurate for the purposes of this work. In cases where the core height is less than the cell width, the elements are set to a width of $H_c/20$ in order to accurately capture the core buckling failure mode.

In a typical simulation of a structure with a cell aspect ratio close to unity and a span of 10 cells, roughly 8,000 elements are required. However, the number of elements required drastically increases when the cell aspect ratio is far from unity, or when there are many cells across the span of the panel. In cases when more than 50,000 elements are required, the mesh size was increased within the range $L_c/20 - L_c/10$ in order to reduce the computational cost of the simulation.

The generalized plane strain and symmetry boundary conditions along the edges of the honeycomb panel allow for buckling to occur, but the effect of the generalized plane strain condition on the buckling load is not immediately clear. In order to investigate the panel edge boundary conditions, a unit cell study

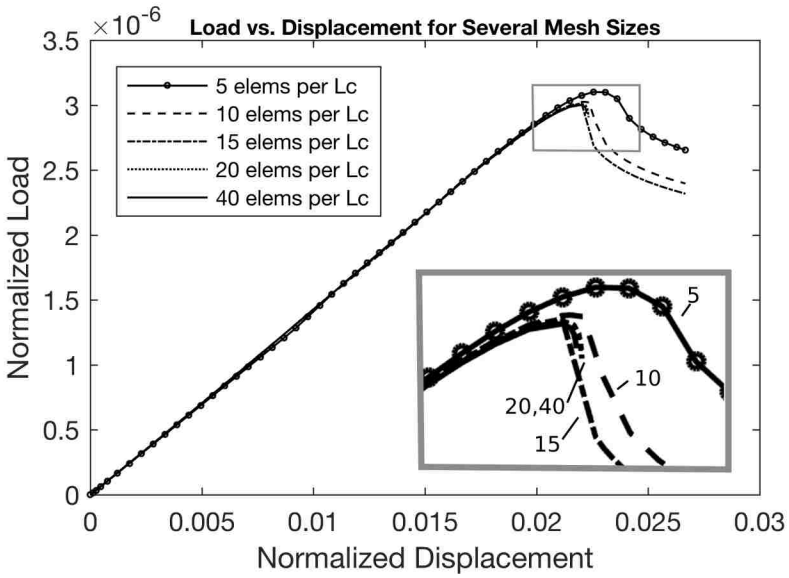

Figure 4.2: Load vs. displacement plot for mesh refinement study.

was also performed on structures that are expected to fail by face buckling. In the study, panels with one to five complete unit cells along the panel width were modeled. Figure 4.4 shows a half-symmetry schematic of the panels that were modeled. The dashed lines on Figure 4.4 indicate the quarter-symmetry lines for the panel under three-point-bending. As before, the single unit cell panel uses quarter symmetry to model a panel with one complete cell and one half cell on either side. The free edges of the panel are modeled with a generalized plane strain constraint. The five cell panel consists of five full cells with a half cell on either side. The results of the cell study are shown in Figure 4.5.

Analysis of the cell study shows that the buckling load increases with the number of cells. This result is expected because Timoshenko [22] has shown that thin plates simply supported on three sides with one free edge have lower buckling loads than plates with four simply supported edges. While the generalized plane strain condition at the edges of the half cells does not allow for completely free movement, the buckling load for those cells is certainly lower than that of the full cells and cells modeled with the symmetry constraint (u3=ur1=ur2=0). As the number of full cells through the width of the structure increases, the generalized plane strain half-cells make up a smaller portion of the structure, which causes the buckling load to increase.

Although the face buckling load is impacted by the number of cells modeled through the width of the panel (see Figure 4.5), using a single unit cell panel ensures conservative results while lowering the

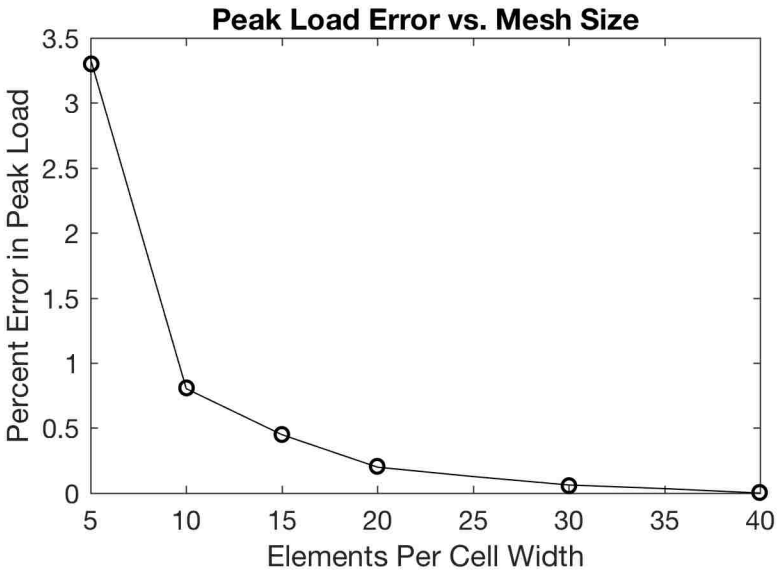

Figure 4.3: Percent difference between peak load different mesh densities.

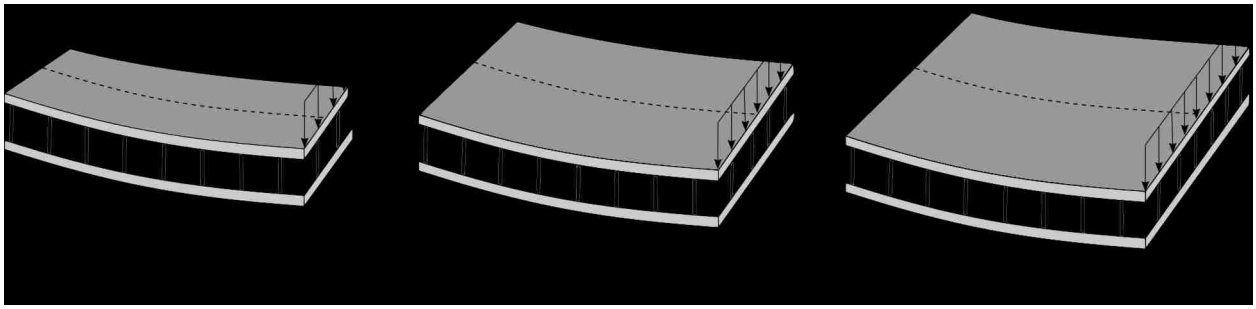

Figure 4.4: Schematic of panels tested in unit cell study.

computational cost of the simulation. For both of these reasons, panels of unit cell width are used in the parametric studies presented in this work. However, it would be prudent for a designer to consider multiple cells in finite element simulations when selecting and refining a final geometry.

With these baseline parameters relating to mesh size, symmetry, and boundary conditions for the finite element model determined, the following sections describe the FEA post-processing procedure for "failure" detection. In order to monitor the square honeycomb panel as it is loaded, the von Mises stresses at all integration points and nodal deflections for every loading step were collected. In addition, the vertical component of the reaction force at the support was monitored to assess the global force-deflection behavior of the panel. The stress, deflection, and force data were used in a post-processing routine (Appendix B) to determine the failure load and mechanism experienced by the panel.

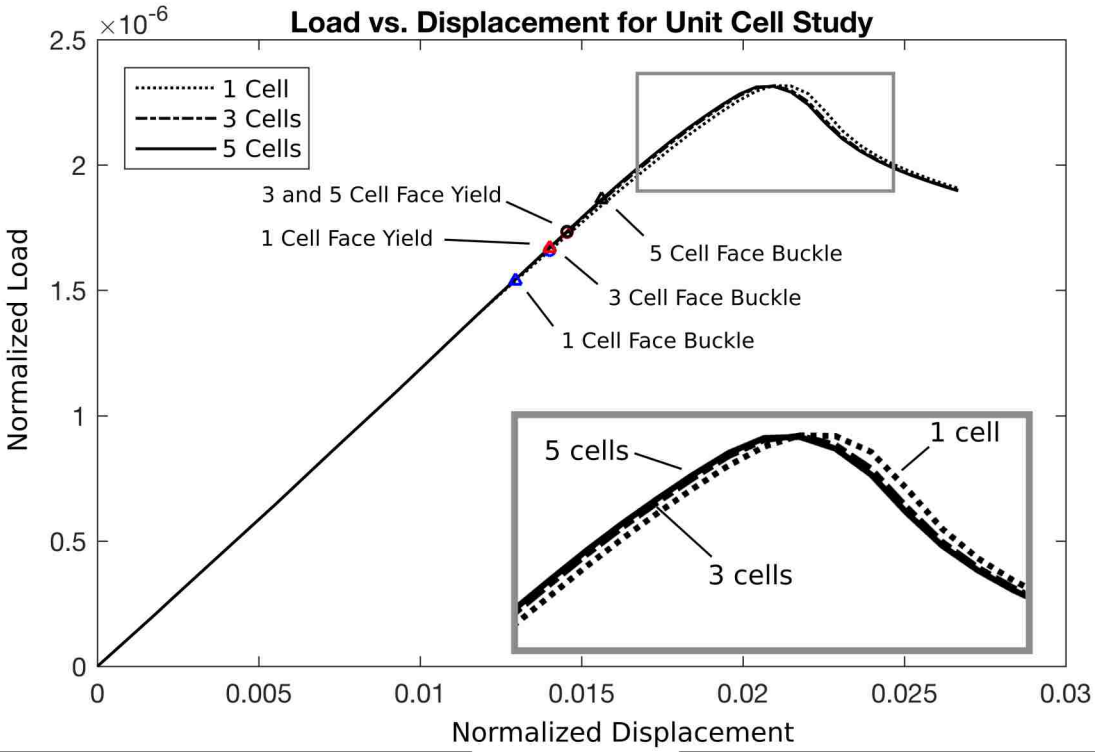

Figure 4.5: Normalized load vs. displacement plot for unit cell study.

4.2 Defining Failure in the Finite Element Model

In order to compare the analytical models to the finite element results, finite element failure thresholds must be developed that detect exactly when the simulated sandwich panel has failed. In this work, failure in the analytical models is considered as the first instance of yielding or buckling. In order to determine when failure has occurred in the FEA, both the global force-displacement behavior of the panel and the local stress in the panel are monitored. In order for the panel to still be considered pre-failure at any point in the finite element simulation, the force-displacement behavior must be linear, all face and core nodes must remain in plane, and all integration points (excluding those near stress concentrations) must remain unyielded. If any of these conditions are violated, the simulated structure is considered to have failed. The failure load for the panel then corresponds to the first load that initiates any of these failure criteria.

In order to determine when the force-displacement behavior of the structure deviates from linearity, either an offset method or a slope method can be utilized. The offset method involves fitting a line through a linear portion of the data and checking for the first time that the data differs from the projected line by a certain percentage. The slope method involves calculating the slope of a linear portion of the data and

comparing it to the slope between each set of two successive data points. While the offset method is less sensitive to sudden changes in slope than the slope method, the offset method has the advantage that it is also less sensitive to noise in the data, making it the standard in the analysis of experimental results. In a finite element simulation, however, where noise is negligible, the slope method can be used to more accurately determine when the presence of yielding or buckling has caused the panel to deviate from global linear force-displacement behavior.

In applying the slope method to the finite element results, thresholds were introduced in order to determine both the original slope, and how much of a deviation constitutes a significant change in slope. The original slope of the force-displacement data was calculated by running a linear regression through a set of data points at the beginning of the simulation, where the load applied was far below the peak load. The first data point corresponding to a force above 10% of the peak load on the panel, along with the four subsequent data points were used in the linear regression. Data points corresponding to forces lower than 10% of the peak load were not included in order to eliminate any non-linearities that may have occurred when the panel was making initial contact with the three-point-bending support at the beginning of the simulation. In cases where yielding occurred in the model before the calculation of the initial slope, the set of data points for the linear regression was truncated and a new regression was run.

Based on non-linearities that may result from yielding o buckling in the panel, sliding between the panel and support, or numerical rounding errors, a threshold of a 20% deviation from the original slope was chosen to represent failure. The 20% threshold was chosen because it is not sensitive to non-linearities that arise from sliding between the sample and support or rounding error. These are behaviors that are not accounted for in the analytical models. At the same time, the 20% slope deviation threshold is triggered by both yielding and buckling.

In addition to using the global force-displacement results to monitor failure, the displacement data from all of the nodes for every step of the simulation were analyzed in order to determine if buckling failure had occurred on a local level. Face sheet and core members of the panel were considered to have buckled if the relative out-of-plane displacement for any node exceeded one tenth of the sheet thickness. As the entire panel translates vertically during the three-point-bending loading, the relative out-of-plane displacement for the face sheet nodes was calculated by comparing the true displacement of each node to a projected displacement. Before the onset of yielding, the displacement for a given face sheet node in the

vertical (y) direction is directly proportional to the load applied to the structure. As a result, the projected displacement for a given face sheet node can be determined by running a linear regression on that node's force-displacement results for steps in the simulation before the onset of yielding. Because the structure does not experience a significant displacement in the horizontal (z) direction as a result of the loading condition, the projected out of plane displacement for the nodes on the longitudinal core members is zero.

The yielding failure modes can be checked on a local level by monitoring the von Mises stress at all integration points of the model, however it is important to neglect areas containing stress concentrations and localized loading effects. The finite element model has one main stress concentration, which manifests itself along the load line, at the intersection of the face sheet and longitudinal core member. Figure 4.6 shows a contour plot of the von Mises stress over the top face sheet; it is seen that the stress concentration is highly localized. The von Mises stresses for the integration points on the top face sheet next to the longitudinal core interface are shown in Figure 4.7. From Figure 4.7 it is clear that there are two factors contributing to the elevated stress level at the load line: (i) the connection with the lateral core members, and (ii) the localized loading effects. In order to evaluate the effectiveness of the analytical models without higher order local loading application effects in the FEA, a strategy of post-processing the FEA results for comparison is needed. As a first comparison approach, post-processing is used to filter out the localized loading effects, while maintaining the effect of the core connection. This is done because the local load application effects are seen as a numerical artifact of how the load is applied and not a physical characteristic that the analytical models are unable to capture.

In order to determine the contribution of the localized loading effects to the von Mises stress in the FEA, the projected stress for each integration point was calculated based on the stress at other corresponding integration points further away from the load. The corresponding integration points started a distance L_c from the point of interest, and were uniformly spaced with a distance of L_c between each point. In this way, the group of integration points used to calculate the projected stress were all spaced the same distance away from the closest lateral core member, ensuring that the effects of the lateral core member interaction would not be lost. As the stress concentration is the strongest directly over the longitudinal core member, only the integration points next to the longitudinal core member intersection were analyzed. Although the stress distribution across the top face sheet is expected to be quadratic in the x-direction, it has been shown that the axial stress dominates the shear stress on the face sheets, so the relationship between stress and

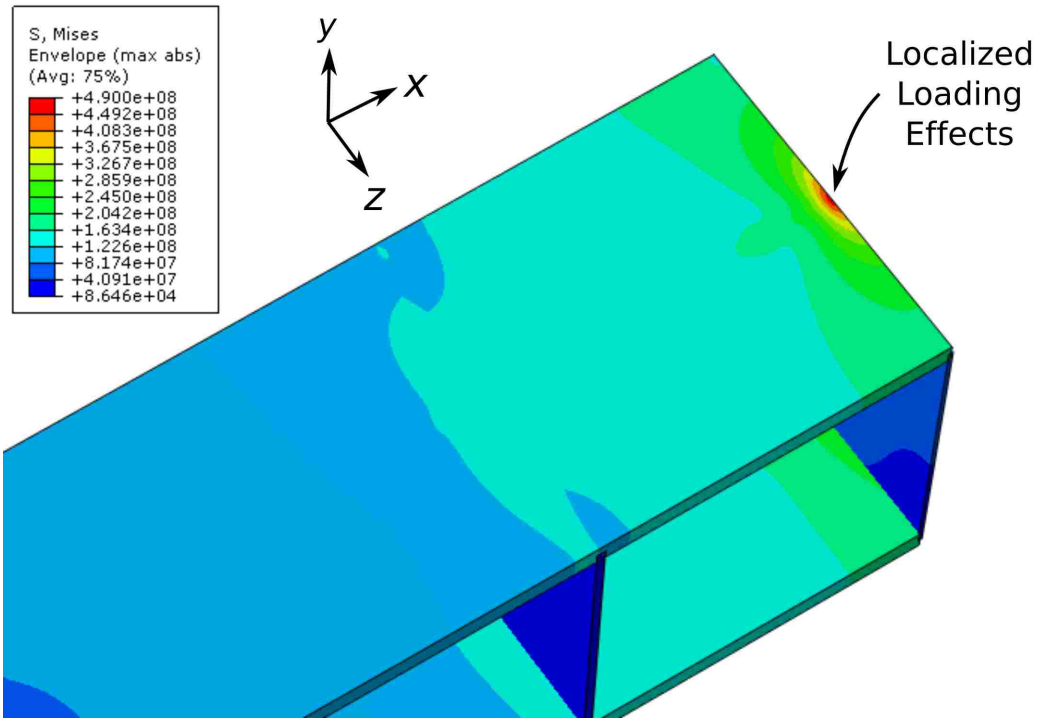

Figure 4.6: Contour plot of von Mises Stress at top face sheet for typical honeycomb geometry.

distance from the load line is mostly linear. As a result, a linear regression was fit through a given group of integration points with spacing L_c in order to determine the projected stress for a corresponding integration point near the load line. Figure 4.7 schematically shows how projections for the first two integration points were constructed.

A parametric study was performed in order to determine the number of integration points that are significantly affected by the stress concentration. Six cases with different panel aspect ratios (l/H_c), cell aspect ratios (L_c/H_c), and face sheet thicknesses (t_f) were investigated. A summary of the selected geometries can be found in Table 4.1. The contribution of the loading effects can be normalized by taking the percent difference between the FEA von Mises stress including the loading effects, and the FEA projected von Mises stress that filters out the loading effects. This percent difference was calculated for all integration points along the top face sheet-longitudinal core member interface, lying within one cell width of the load line, for each geometry in the parametric study. It was determined that using the cell height, H_c, in order to normalize the distance from the load line allowed the results from each geometry to most closely match, and the resulting plot is shown in Figure 4.8. Based on Figure 4.8, integration points within a distance of $0.2 \times H_c$ from the load line are significantly affected by the localized loading stresses,

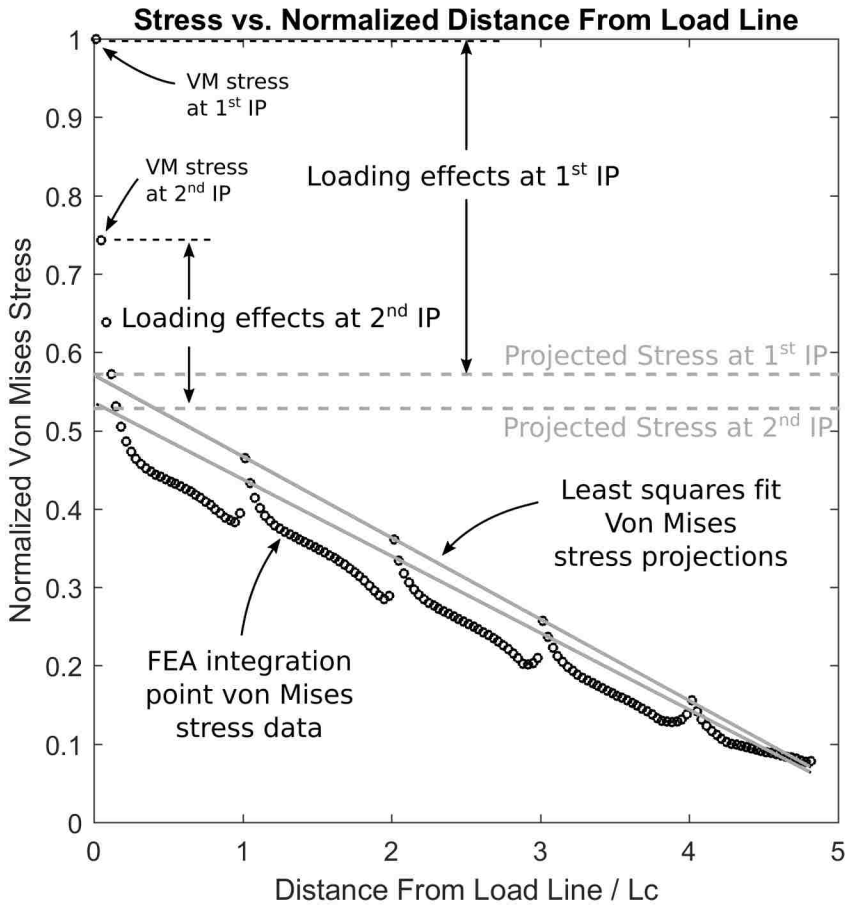

Figure 4.7: Normalized von Mises stress at integration points on top face sheet-longitudinal core interface.

while integration points outside that region are affected by no more than 10%. Clearly, the loading effects are not solely dependent on the cell height, H_c, however for practical ranges of characteristic length scale l, cell aspect ratio H_c/L_c, and face sheet thickness t_f, cell height is the best indicator of the region of the structure that will be significantly impacted. As a result of the parametric study, all integration points within a distance of $0.2 \times H_c$ along the x direction from the load line were ignored when checking for face and core yielding at a local level.

4.3 Evaluating the Performance of Analytical Models Using FEA Results

A parametric study is used to compare the analytical models and finite element results. The range of geometries presented in the failure plots from Section 3.5 were considered, and 19 finite element simulations

Case	H_c/l	L_c/l	t_c/l	t_f/l	Cell Aspect Ratio
1	0.2	0.2	0.02	0.02	1
2	0.1333	0.1333	0.01333	0.01333	1
3	0.0667	0.0667	0.00667	0.0667	1
4	0.2	0.2	0.02	0.01	1
5	0.2	0.1333	0.01333	0.01333	0.667
6	0.1333	0.2	0.01333	0.01333	1.5

Table 4.1: Geometries used in parametric study investigating localized loading effects.

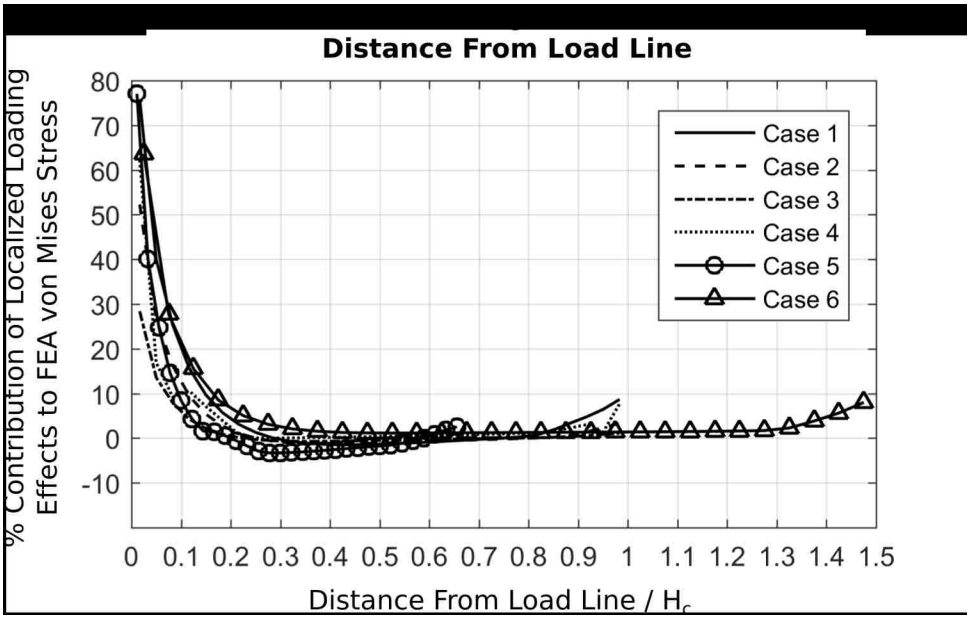

Figure 4.8: Percent contribution of the localized loading effects to the FEA von Mises stress at the top face-longitudinal core interface, as a function of distance from the load line normalized by the cell height, H_c.

were run. The results of the parametric study are shown in Figure 4.9.

The black circles in Figure 4.9 indicate the geometries used in the finite element simulations. Two numbers are located next to each finite element simulation black circles. The top number is the percent difference between the finite element failure load and the traditional decoupled analytical model failure load. The bottom number is the percent difference between the finite element results and the proposed model prediction. The finite element failure modes are listed to the left of each finite element simulation black circle data point. In cases where multiple failure modes were triggered within two subsequent simulation loading steps, both are shown on the plot. For each simulation, the failure modes in bold represent those that were activated on the first of the two simulation steps. The non-bolded failure modes are those that occurred one loading step after the initial failure mode.

The results of the parametric study show that the proposed model is more accurate at predicting which failure mode will be active than the traditional decoupled model. The differences between the models can most clearly be seen in the core yielding regime for the proposed model. While the proposed model is more successful at predicting core yielding, the traditional decoupled model does a slightly better job predicting when core buckling will occur. The core buckling failure zone for the proposed model is expanded because the axial stress in the core is accounted for. Although the traditional decoupled model more accurately predicts the the transition to core buckling being the dominant failure mode, the failure load prediction associated with the onset of core buckling is non-conservative because the axial stress in the core is not accounted for.

In the face and core yielding regimes, the proposed model is more accurate than the traditional decoupled model in predicting both the failure load, and which failure mode will be active. The proposed model is accurate to within 10% across its predicted face and core yielding failure regions, while the traditional decoupled model is anywhere from 30% non-conservative, to 20% conservative. The traditional decoupled model predictions become more conservative as the face sheet thickness is decreased, and much less conservative as the face sheet thickness is increased. This is again because the traditional decoupled model does not account for the axial stress in the core. When the face sheets are thin and more material is devoted to the core, the core's contribution to the cross-sectional moment of inertia of the structure is not captured by the decoupled model, resulting in a very conservative estimate of strength. When the face sheets are thick and the core is relatively weak, the decoupled model fails to account for the yielding caused by the high axial stress at the top and bottom of the core members, and decoupled model prediction is very non-conservative.

While the models differ in their levels of conservatism when predicting the yielding failure modes, both models are very conservative when face and core buckling are the dominant failure modes. The conservatism arises because neither of the models accounts for rotational constraints of adjacent plate members during buckling. As will be shown in the following section, the optimal structure in the low loading regime is governed by both the yielding and buckling failure modes. As a result, it is not desirable for the buckling load predictions to be significantly more conservative than the yielding predictions. In an attempt to reduce the amount of conservatism in the buckling failure load predictions, the discussion section of this work will present some first steps towards considering adjacent plate rotational constraints

in the face buckling failure mode for the proposed model.

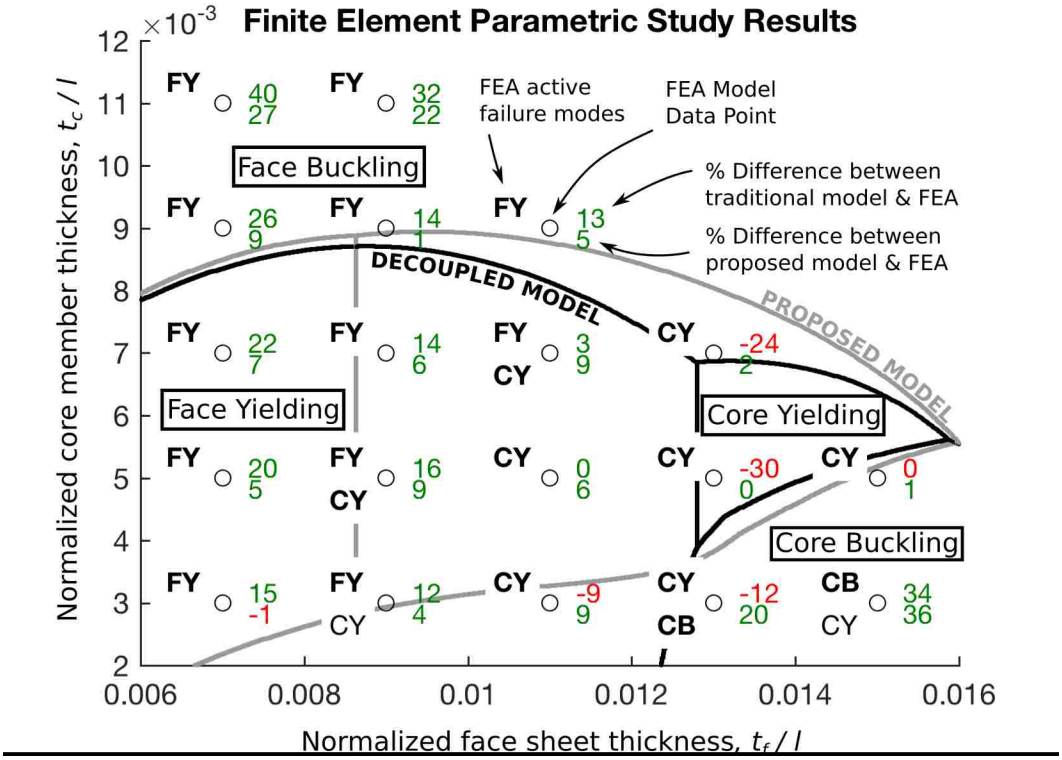

Figure 4.9: Comparison between finite element results and analytical model predictions.

Lastly, the optimal geometries with non-dimensional structural weight, $\Psi = 0.035$, predicted by the analytical models are also compared to the finite element results. Figure 3.11 shows that the optimal (i.e. highest load bearing) geometry predicted by the traditional decoupled model is at the intersection of the face and core yielding regimes. Figure 3.12 shows that the optimal structure predicted by the proposed model is not unique but encompasses $0.01 \leq t_f/l \leq 0.012$, where core yielding is the dominant failure mode. Looking at these two areas on the parametric study map presented in Figure 4.9, it is clear that the optimal geometry predicted by the traditional decoupled model lies in an area where the decoupled model makes non-conservative predictions. The optimal geometry predicted by the proposed model, however, lies in an area where the proposed model makes an accurate and conservative prediction. A further discussion of the optimal geometries suggested by both models and the finite element results will be presented in Chapters 5 and 6.

In summary, while the proposed model still has some areas for improvement, it can be relied upon to consistently provide accurate and conservative predictions for the strength of the honeycomb panel under

three-point-bending. The benefit of the proposed model is that it can more accurately predict the failure load and active failure modes than the traditional decoupled model, while still remaining computationally tractable. As such, it is a valuable tool to be incorporated in optimization protocols to identify generally promising structure geometries for a variety of objectives. Certainly, optimal geometries would need further refinement with parallel more detailed finite element analysis for end use.

Chapter 5

Optimization

While finite element simulations could be used in an optimization scheme that selects the lowest weight structure for a given load, such a brute-force scheme would require an extraordinary amount of processing power. Instead, the analytical models have been incorporated into an optimization scheme in order to identify relationships between minimum weight structures and the loading regime. Optimizations using analytical models have been performed previously by Wicks and Hutchinson [2], Valdevit et al. [15] and Rathbun et al. [3] for various honeycomb and truss structures under combined shear and bending loads. The numerical optimization protocols in this work are similar to those presented by [2, 3, 15], the only difference being that a multi-objective function is required in this work in order to explore the entire range of optimal geometries in the high loading regime. The multi-objective scheme is necessary because the exact geometry of the optimal structure, and not solely the non-dimensional structural weight, is of interest in this work. From a designer's point of view, with a light weighting mandate, it would be practical to select a geometry suggested by the analytical model optimization, and then to run several more detailed finite element cases that vary the geometric parameters in order to determine if any additional weight can be saved.

5.1 Optimization Scheme

The MATLAB® sequential quadratic programming optimization algorithm "FMINCON" was used to optimize the honeycomb geometry to achieve the lowest possible weight for non-dimensional loads ranging from $\Pi = 10^{-6}$ to $\Pi = 10^{-4.5}$. Optimizations were run for both the decoupled (Section 3.2) and the pro-

posed simplified coupled (Section 3.4) analytical models, under the geometric constraints in Table 3.5. In addition, an upper bound on the core height of the panel, H_c, was set at $0.2 \times l$ to ensure that the optimized panel is slender in accordance with the Euler-Bernoulli model assumptions. The maximum core and face sheet thicknesses were also constrained in order to maintain the slender plate assumptions utilized in the derivation of the buckling failure modes. The upper limit on the core sheet thickness, t_c was set to one tenth of the minimum of the cell width and cell height. The upper limit for the face sheet thickness, t_f was one tenth of the cell width, L_c. The constraints imposed to respect the model assumptions are summarized in Table 5.1.

Constraint	Model Assumption
$\frac{H_c}{l} \leq 0.2$	Euler-Bernoulli slender beam assumption
$t_c \leq H_c$	Thin plate assumption
$t_c \leq L_c$	Thin plate assumption
$t_f \leq L_c$	Thin plate assumption

Table 5.1: Constraints in accordance with the model assumptions. Optimization constraints governing structural failure are shown in Table 3.5.

Single and multi-objective optimization approaches, both using "FMINCON" were taken in order to determine the lowest structural weight and the most efficient geometry for a given load. The objective function for the single objective optimization is solely the non-dimensional structural weight, given by equation (2.8). A multi-objective optimization scheme was necessary in order to determine the optimal honeycomb geometry for certain loads; this was because the yielding failure constraints given by the decoupled and proposed simplified coupled models are dependent only on the ratio t_c/L_c, and not on the two design variables independently. As a result, there are a wide range of minimum weight geometries for some loads, and a multi-objective scheme is necessary in order to identify the limits of that range.

In order to reach the global minimum weight and avoid local minima for the single objective optimization, ten optimizations were run for each load case, each one using a different set of initial geometric design variable values. The first optimization for each load was run with initial design variables equal to the optimized variables from the previous load. The initial design variables were randomized for the remaining nine optimizations, each one taking on a value between 50%-150% of the optimal value from the previous load.

Using the lowest structural weights generated by the single-objective optimization approach, a multi-

objective optimization was then used to determine the range of L_c and t_c values that correspond to the allowable structures of minimum weight for a given load. In addition to identifying the allowable range of L_c and t_c, another multi-objective optimization was used to find the structure that achieved the lowest possible weight; however, an additional objective related to minimizing the cumulative failure activity level was added to reduce the chance of structural failure. The multi-objective function is:

$$f(L_c, H_c, t_c, t_f, \Pi) = k_0 \frac{\Psi - \overline{\Psi}}{\overline{\Psi}} \times 100 + k_1 FY^2 + k_2 CY^2 + k_3 FB^2 + k_4 CB^2 + k_5 L_c, \qquad (5.1)$$

where Ψ is the non-dimensional structural weight given by equation (2.8), and $\overline{\Psi}$ is the minimum structural weight for the given load (generated by the single-objective optimization). FY, CY, CB and FB, are all failure constraint activity levels that range between 0 and 1, given by the left hand side of the inequalities in Table 3.5. They have been squared in order to add an additional penalty as the activity level reaches the maximum allowed value of 1. Some tuning parameters (k_{0-5}) are added to control the weights assigned to each objective in the function. To force the structure towards the lowest possible weight, k_0 should be set to a much higher value than k_{1-5}.

5.2 Optimization Results and Discussion

Figure 5.1 shows how the weight of the square honeycomb structure increases with the applied load. Based on the results of the single-objective optimization presented in Figure 5.1, it is clear that the decoupled model suggests a lower optimal weight structure than the proposed simplified-coupled model. This result is in accordance with the comparison of the models in Section 4.3, that suggested that the decoupled model is non-conservative when compared to the proposed simplified model and finite element results.

In order to determine the geometry of the optimal structure over a broad range of loads, three multi-objective optimizations were run to find the minimum weight structure with the maximum cell width, L_c, minimum cell width, L_c, and lowest chance of failure. Determining the entire range of optimal cell width, L_c, and core member thickness, t_c, is important from a designer's point of view because certain cell widths or core member thicknesses may offer benefits such as reduced manufacturing cost. The minimum weight structure with the lowest cumulative failure constraint activity level, on the other hand, can be used as a guideline for designers in selecting a geometry when structures with particular cell widths or

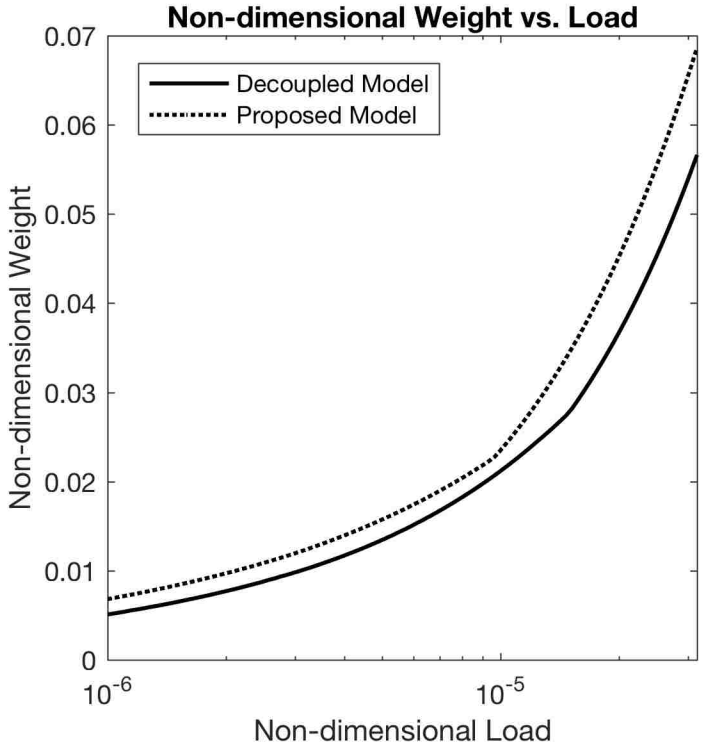

Figure 5.1: Non-dimensional weight vs. load for decoupled and proposed models using single-objective optimization scheme.

core sheet thicknesses do not offer any additional benefits. Table 5.2 shows the tuning parameters used in each optimization. When k_5 is positive, the contribution of the last term in the objective function given by equation (5.1) increases with increasing L_c, so the optimization scheme seeks to minimize L_c, after minimizing the structural weight. When k_5 is negative, the opposite is true. Because the yielding failure criteria are dependent on the ratio t_c/L_c, the maximum allowable value of t_c for a given structural weight and load is obtained when L_c is maximized. The minimum core sheet thickness is obtained when L_c is minimized. For the third multi-objective optimization, preference is given to reducing the structure's proximity to failure. The tuning parameters k_{1-4} are all set at equal values that are substantially lower than k_0, so that after the dominant k_0 term of the objective function is minimized, the geometry of the structure is selected to be as far away as possible from violating the failure constraints. Although decreasing a failure constraint activity level below unity when others are active does not offer any advantages according to the analytical models, in cases where doing so does not sacrifice any weight, it may end up benefiting the structure if there is any coupling between failure modes.

k_0	k_1	k_2	k_3	k_4	k_5	Description
1	0	0	0	0	0.05	Minimize weight with lowest choice of L_c and t_c
1	0	0	0	0	-0.05	Minimize weight with highest choice of L_c and t_c
1	0.01	0.01	0.01	0.01	0	Minimize weight with lowest failure activity levels

Table 5.2: Tuning factors used for multi-objective optimizations.

Figure 5.2 shows how the geometry of the structure changes with the load. The grey lines indicate the maximum and minimum allowable L_c and t_c values that still result in the lowest possible weight, and the black lines show the results given by the minimized failure activity level optimizations. For both models, the point where the minimum and maximum L_c and t_c (grey lines) branch off marks the transition from buckling-dominated to yielding-dominated regimes. The area between the branched grey lines for each model represents all of the allowable minimum weight choices for L_c and t_c. As the value of L_c/t_c is fixed by the minimum weight term in the optimization, once a value of either t_c or L_c is selected, the other one is then fixed and it cannot be freely chosen.

The bounds on the minimum and maximum cell widths, L_c, and core thicknesses, t_c, result from the buckling failure constraints and the constraints necessitated by the model assumptions. For example, consider the maximum core thickness, t_c, and cell width, L_c, line for the proposed model. Initially, t_c and L_c can be increased until the point where the cells are too large and the face buckling constraint is violated. At the same time, the maximum core thickness, t_c, cannot exceed $0.02 \times l$, without violating the constraint that t_c must be less than one tenth of the cell height, H_c. As the load increases and the core thickness is maximized at $t_c = 0.02 \times l$, there is a sharp drop in the maximum cell width, L_c, because more core sections per unit width are required in order to support the increasing load. A similar trend is found in the minimum core thickness, t_c, and cell width, L_c, results. Initially, the cell width and core thickness can be minimized up until the core buckling constraint is violated. The cell width, however, is also constrained to be at least ten times the face sheet thickness ($L_c \geq 10t_f$). As the required face sheet thickness, t_f, increases, this constraint overwhelms the core buckling constraint, and there is a sharp increase in the minimum allowable cell width, L_c, and core sheet thickness, t_c.

For both models, the point where the minimum and maximum L_c and t_c (grey lines) branch off marks the transition from the buckling dominated regime to the yielding regime. This can be visualized by looking at the failure constraint activity levels as a function of the load for the decoupled model and proposed model, in Figures 5.3 and 5.4. In the low loading regime for the decoupled model, face yielding,

core buckling, and face buckling are all active failure modes. As the load increases, the core yielding failure mode becomes active, and the buckling constraints are dependent on the selected core sheet thickness and cell width. If the maximum cell width, L_c, is selected, the core buckling failure activity level is minimized, but the face buckling activity level persists at unity. The reverse is true if the minimum cell width, L_c, is selected. If the cumulative failure constraint activity level is reduced by the multi-objective optimization scheme, the face and core buckling activity levels can be reduced simultaneously.

Figure 5.4 displays buckling and yielding regimes for the proposed model that are similar to those exhibited by the decoupled model. A major difference is that core yielding plays a more active role than face yielding for the proposed model. The buckling regime can be understood in two parts. In the first part, face yielding is active in addition to the buckling modes. In the second part, core yielding becomes active along with the two buckling modes. The activity levels for core yielding and face yielding are determined by the face sheet thickness to cell height ratio, t_f/H_c. Recall that according to the proposed model, the maximum axial stress in the face sheets is proportional to the maximum axial stress in the core (Section 3.4). The linear stress distribution through the cross-section of the structure allows the maximum face sheet normal stress to be written in terms of the maximum core normal stress:

$$\sigma_{f,max} = \left(1 + \frac{2t_f}{H_c}\right) \sigma_{c,max}. \tag{5.2}$$

Also, a shear stress component is predicted in the core, while the shear stress in the face sheets is neglected. For the face sheet yielding failure mode to be active, the maximum von Mises stress at the surface of the face sheets must exceed the von Mises stress at the top of the core. A higher face sheet von Mises stress can only be achieved if the contribution of the $\left(\frac{2t_f}{H_c}\right) \sigma_{c,max}$ term to the face sheet von Mises stress outweighs the contribution of the core shear term (given in Table 3.3), to the core von Mises stress. As the load increases, the cell height, H_c, increases faster than the face sheet thickness, t_f. The increase in H_c/t_f reduces the contribution of the additional axial stress in the face sheets given by equation (5.2), which causes the core yielding failure mode to surpass face yielding failure mode at a relatively low load.

The inactivity of the face yielding failure mode in the yielding regime for the proposed model illustrates the face and core "coupling" effects of the model. In the decoupled model, both face yielding and core yielding are active in the yielding regime. Both yielding modes are active because the face yielding failure criterion is independent of the core thickness, t_c, and the core yielding failure criterion is independent of

the face sheet thickness, t_f. Consider for example, a structure carrying a given load in the yielding regime with core yielding being the only active failure mode. If the decoupled model is used, the weight of the structure could be reduced at the same load level by decreasing the face sheet thickness, t_f. As the core yielding criteria is independent of the face sheet thickness, the face sheet thickness could be reduced until either face yielding or buckling became active. Whereas, if the proposed model is applied, the face sheet thickness, t_f, could not be reduced, because such a reduction would lower the area moment of inertia of the structure, decreasing the load that it could carry.

Along with the inactivity of the face yielding failure mode, the most significant difference between the decoupled model and the proposed model is that the decoupled model maximizes the cell height, H_c, at a much lower load than the proposed model. This difference between the two models can be seen by looking at the cell aspect ratio as a function of load in Figure 5.5. At low loads, the optimal cell aspect ratio, L_c/H_c, identified by the decoupled model is much lower than that identified by the proposed model. The optimal cell aspect ratio identified by the proposed model is close to unity across the entire loading regime, suggesting that cuboidal honeycomb structures are preferred.

The decoupled model predicts that the optimal structure in the buckling regime should have a much lower cell aspect ratio, L_c/H_c, than the proposed model because it does not account for the effect of the axial stress in the core. By neglecting the axial stress in the core, the decoupled model considers the core less prone to buckling than the proposed model, allowing the core sections in the decoupled model to be larger and thinner than in the proposed model. In addition, neglecting the axial stress in the core causes the face sheet stress to be higher because the core's resistance of the internal bending moment is not accounted for. As a result, the decoupled model predicts an increased risk of face buckling, so the optimization scheme identifies geometries with a lower cell width, L_c, than the proposed model. The additional weight placed on the face buckling failure constraint by the decoupled model ends up increasing the cell height, H_c, and decreasing the cell width, L_c, which in turn lowers the cell aspect ratio, L_c/H_c.

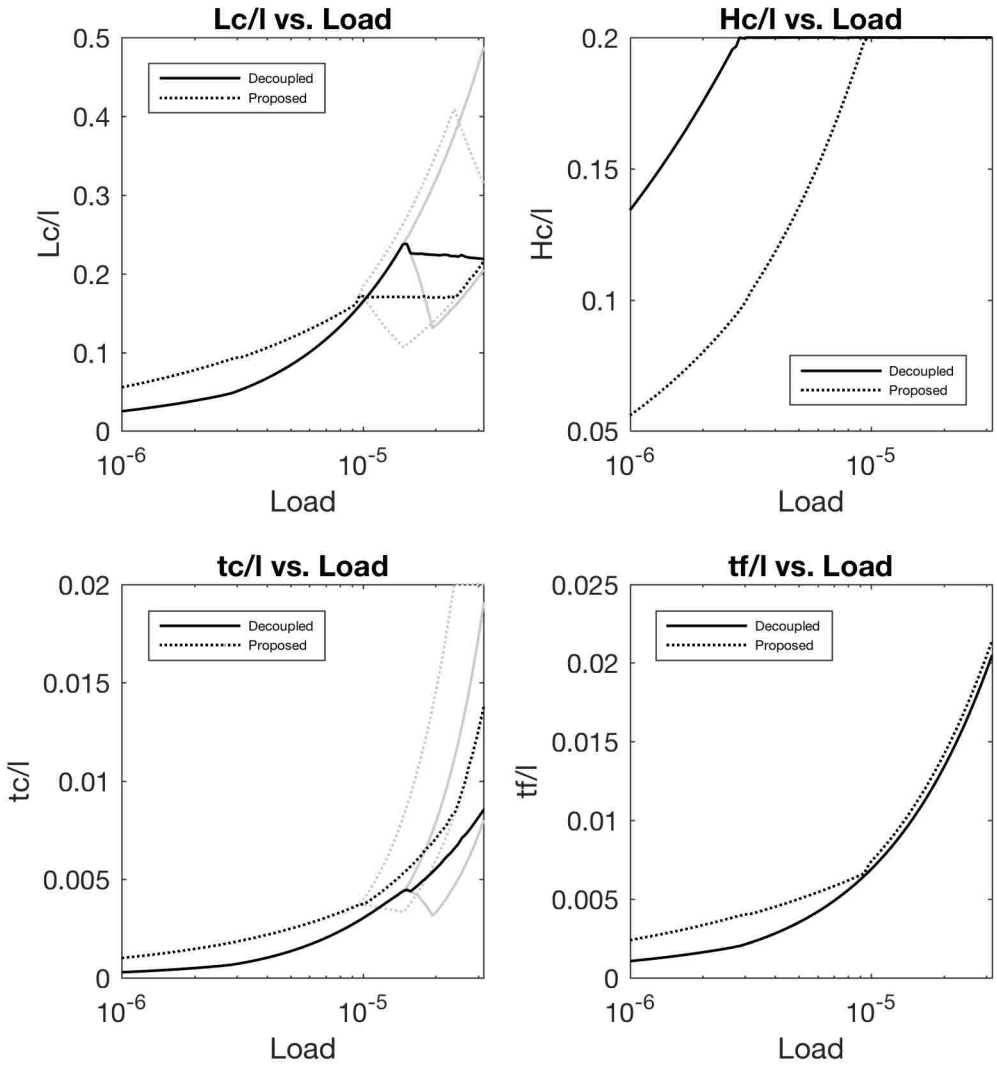

Figure 5.2: Optimal structural geometry for the decoupled and proposed models given by the multi-objective optimization scheme.

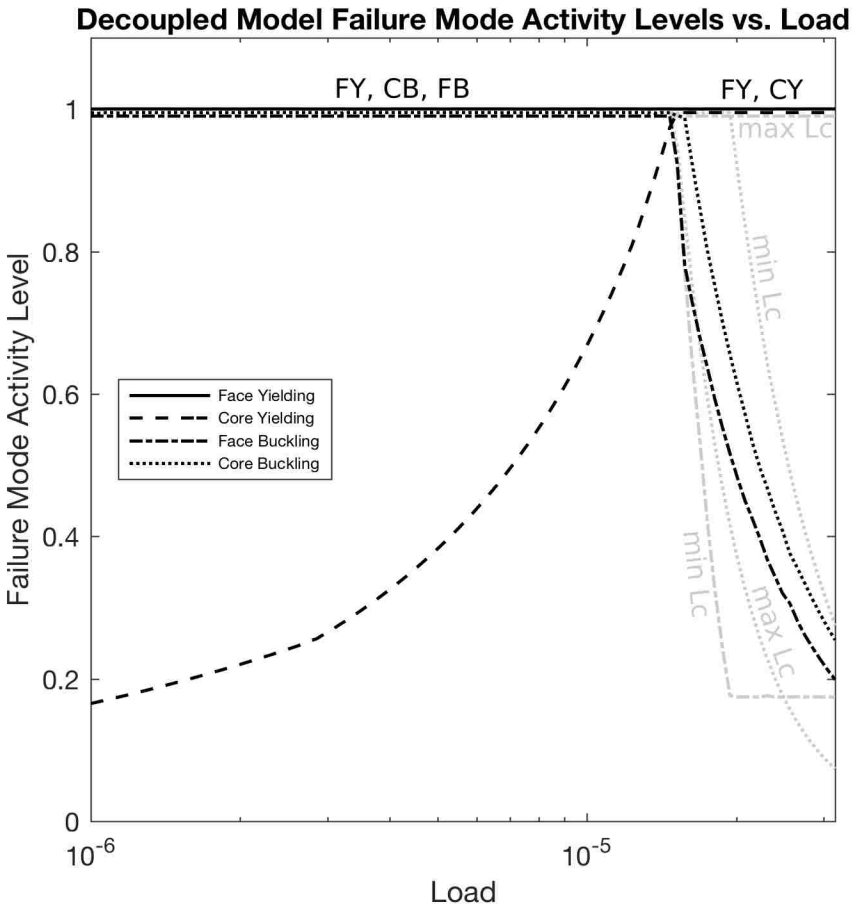

Figure 5.3: Failure constraint activity levels for the decoupled model.

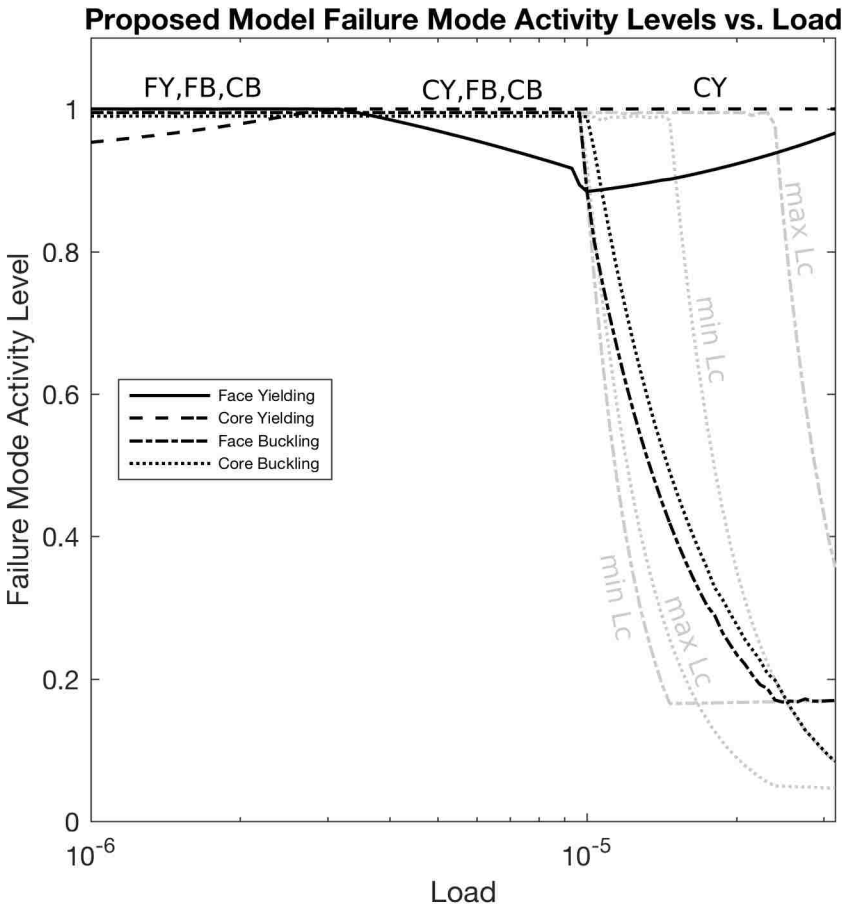

Figure 5.4: Failure constraint activity levels for the proposed model.

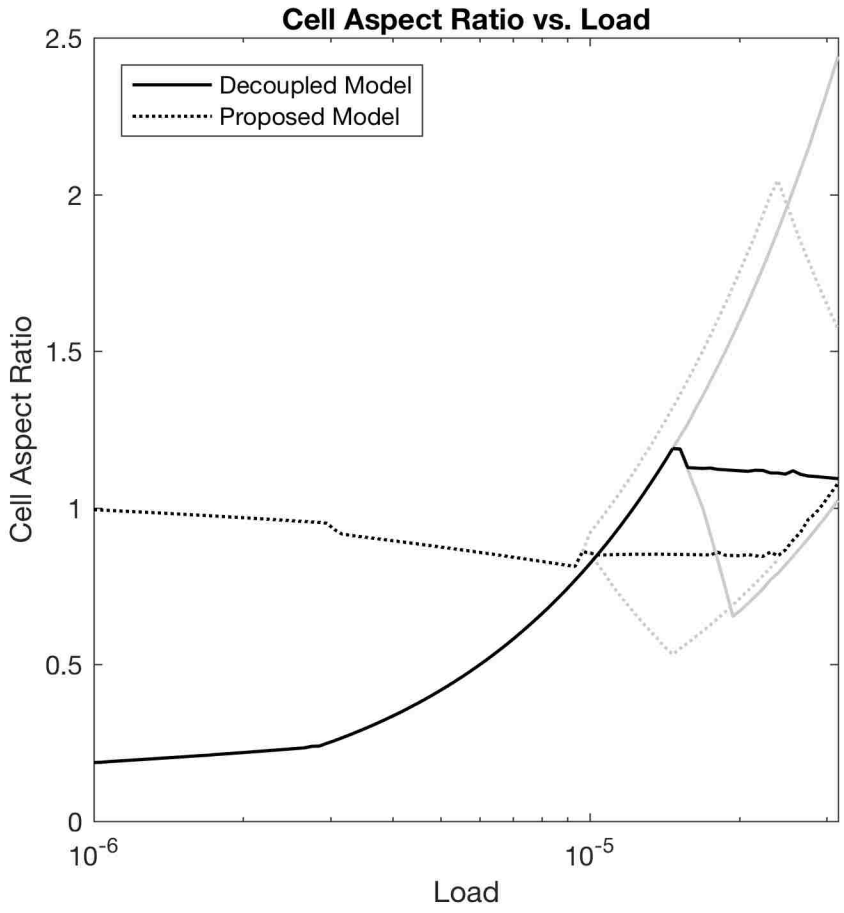

Figure 5.5: Cell aspect ratio, L_c/H_c, vs. non-dimensional load for the proposed and decoupled models.

Chapter 6

Discussion

Through the analysis in Chapters 1-5, the proposed analytical model for the performance and failure of square honeycomb panels has been verified and its benefits compared to existing traditional decoupled models have been outlined. Below, for a given load level, the weight optimal geometries identified by the analytical models are compared to the optimal geometry identified by a parametric finite element study. While the proposed model balances accuracy with simplicity and computational costs, several points for discussion and directions for further improvement are also presented below.

6.1 Comparison of Analytical Model Optimizations to FEA Results

To evaluate the performance of the analytical model optimization schemes, finite element parametric studies were conducted to determine the optimal structural geometry for two different non-dimensional structural weights. Non-dimensional structural weights $\Psi = 0.0123$ and $\Psi = 0.035$ were selected in order to cover both the low and high loading regimes.

6.1.1 Low Loading Regime

In the low loading, buckling dominated regime, the optimal geometry predicted by the decoupled model is very different from the geometry predicted by the proposed model. The most notable difference between the structures is in the cell height, H_c. Figure 5.2 shows that the optimal cell height, H_c, identified by the decoupled model, is higher than the optimal cell height identified by the proposed model in the low loading regime. The cell height, H_c, is the most important geometric parameter because it controls the aspect ratio

of the panel, (l/H_c), and has the largest contribution to the cross-sectional moment of inertia of the panel (see equation 3.7), which is directly related to the stiffness of the panel. Therefore, if a designer can identify the optimal cell height, he or she will have a better idea of how the panel will fit in with other design elements spatially, and how the panel will perform in terms of stiffness.

In order to compare the model results, finite element simulations were run for the optimal geometry with fixed non-dimensional weight ($\Psi = 0.0123$) identified by both the decoupled and the proposed models. In addition, a parametric finite element study was conducted to identify the optimal geometry according to the FEA results. The non-dimensional structural weight $\Psi = 0.0123$, was chosen because the proposed model predicts that all four failure modes are active in the optimal structure at that weight (see Figures 5.1 and 5.4). The optimal honeycomb structure geometry with a non-dimensional weight $\Psi = 0.0123$ identified by the traditional and proposed models, as well as the geometry identified by the finite element parametric study are summarized in Table 6.1. The core height, H_c, identified by the proposed model matches very closely with the optimal core height identified by the finite element parametric study. On the other hand, the optimal cell width, L_c, identified by the finite element study, matches more closely with the decoupled model optimization results. The cell width, however, is not as important as the core height because it does not have a significant effect on the panel's external dimensions or stiffness. The optimal face sheet and core thicknesses identified by the finite element parametric study are in between the optimal face sheet and core thicknesses identified by the analytical model optimizations.

	H_c/l	L_c/l	t_c/l	t_f/l
Decoupled Model	0.2000	0.0698	0.0011	0.0030
Proposed Model	0.1029	0.0954	0.0019	0.0041
Finite Element Study	0.1100	0.0647	0.0015	0.0036

Table 6.1: Optimal geometries for non-dimensional structural weight $\Psi = 0.0123$.

The finite element results for the optimal structures with non-dimensional weight $\Psi = 0.0123$ identified by both analytical models and the finite element parametric study are shown in Figure 6.1. The peak load for the structure identified by the decoupled model is higher than the peak load of the structure identified by the proposed model. However, the core of the structure predicted by the decoupled model buckles well before the peak load is reached. On a global force-displacement level, it could be argued that the structure identified by the decoupled model optimization performs better than the structure identified by the proposed model because the core buckling does not significantly affect the structure's overall per-

formance. However, according to the failure criteria presented in this work, the optimal structure identified by the proposed model fails at a higher load than the structure selected by the decoupled model. Minimal finite element tuning of the proposed model panel geometry was required in order to arrive at the finite element parametric study identified optimal geometry, making the proposed model optimization an excellent starting point for design.

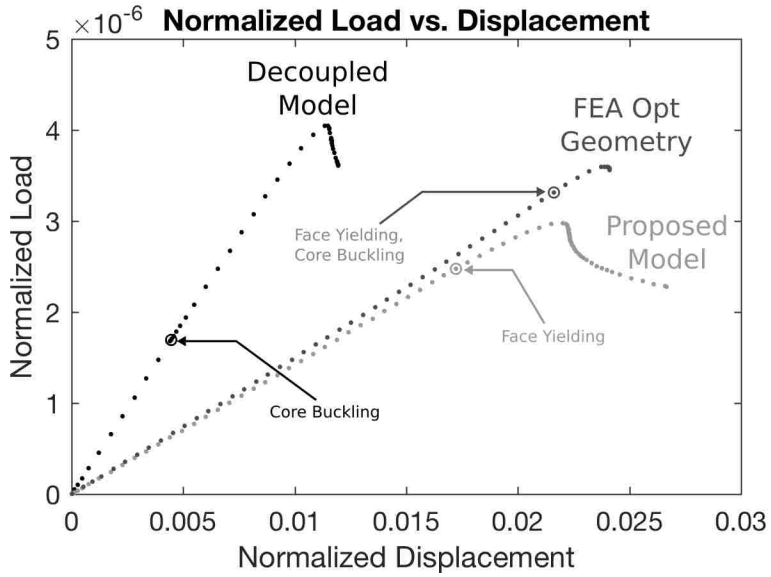

Figure 6.1: Finite element load vs. displacement results for optimal geometries with non-dimensional weight $\Psi = 0.0123$, identified by the decoupled and proposed models.

6.1.2 High Loading Regime

The optimal geometry identified through parametric finite element studies in the high loading regime can also be compared to the analytical model predictions. Figure 6.2 indicates where the optimal geometries predicted by the analytical models and finite element results lie on the constant weight failure mechanism map presented in Section 3.5. The shaded areas for the analytical models indicate geometries with at least 99.5% of the maximum failure load for the decoupled or proposed model. The boundary of the shaded area corresponding to the finite element optimal geometries was approximated based on a parametric study of finite element cases run with a spacing of 0.001in the t_c/l and t_f/l directions.

Figure 6.2 shows that the optimal geometry predicted by the proposed model is closer to the finite element results than the decoupled model. Furthermore, the optimal finite element model geometry range shows a greater dependance on the core thickness t_c, than the decoupled and proposed model predictions.

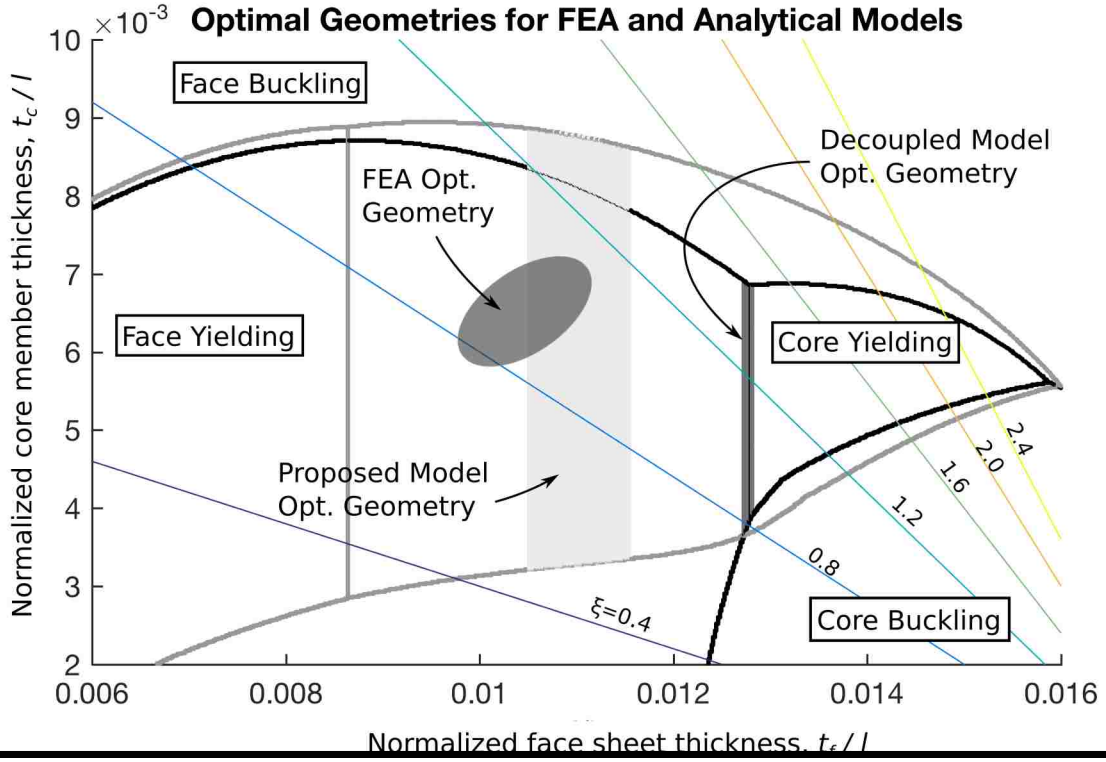

Figure 6.2: Optimal geometries predicted by analytical models, and observed in FEA results. $L_c/l = 0.2$, and $\Psi = 0.035$.

The optimal finite element geometry has a cell aspect ratio L_c/H_c close to unity, and is located midway between the face buckling and core buckling failure zones. The finite element optimal geometry results for a structural weight of $\Psi = 0.035$ agree well with the multi-objective optimization results presented in Figure 5.2. The location of the optimal finite element geometry and its dependance on t_c could indicate that there is some coupling between the failure modes in the finite element results. If there were no coupling between failure modes in the finite element results, all finite element models of geometries located in the face and core yielding failure zones with the same normalized face sheet thickness, t_f/l, would behave identically. By being located in the middle of the proposed model core yielding failure zone, the optimal finite element geometry reduces the failure activity levels of face and core buckling without sacrificing any load bearing capability.

6.2 Consideration of Rotational Constraints in Face Buckling Failure Mode

Thus far, all of the analytical models have neglected the rotational constraints of adjacent plate members in the buckling failure modes. Proper treatment of the boundary conditions for plates subject to buckling is important because the buckling coefficient can vary by as much as 100% depending on the plate edge conditions used in the calculations. In this section, a simplified but conservative approach is taken to determine how the buckling coefficient of a face sheet plate is affected by the consideration of the rotational constraints from adjacent face sheet and core members.

In order to consider the face plate edge constraints, the adjacent members to the plate that will first undergo buckling must be identified. Figure 6.3 shows a quarter-symmetry view of a square honeycomb panel under three-point-bending. In Figure 6.3, assume that plate A carries a significant axial load, and is therefore one of the first plates to buckle. Adjacent face plate members B and C will carry a similar axial load to plate A, and therefore will not rotationally constrain plate A from buckling in the y-direction. Plate E is part of a longitudinal core member, which means that it may be close to buckling or yielding near the shared edge with A. To be conservative, it will be assumed that plate E poses no rotational constraint about the x-axis to the edge of plate A. Plate D however, is part of a lateral core member, which is virtually unstressed according to the present analytical models. As a result, it will be assumed that plate D is able to provide a rotational constraint about the z-axis along the edge of plates A and B. Plate A can therefore be modeled as a square plate that has some rotational constraint on the loaded edges, and is simply-supported along the other two edges.

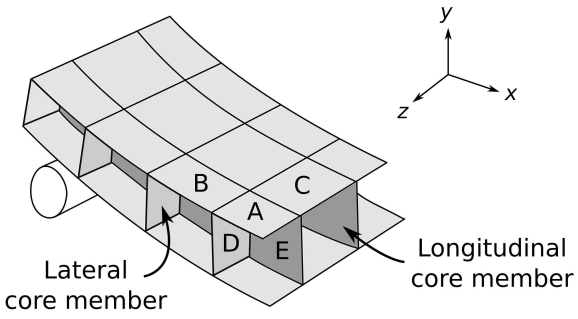

Figure 6.3: Quarter symmetry view of honeycomb panel under three-point-bending.

To simplify the proposed model while maintaining a conservative approach, only the stiffness of the lateral core members with respect to bending moments in the z-direction in Figure 6.3 will be considered.

In order to visualize this approach, each lateral core member can be imagined as a set of thin parallel beams (Figure 6.4). In order to illustrate the concept, the beams in Figure 6.4 have finite width. In the actual model, however, the beams are treated as infinitely thin so that the rotation at the top edge of the core member can be considered a continuous function. Modeling each core member in this way allows the angle of rotation at a point along the top edge of the core member to be directly proportional to the moment applied at that point, which simplifies the analysis of the face plates. The approach is conservative because it does not account for the added stiffness resulting from the plate twisting or bending in the y-direction.

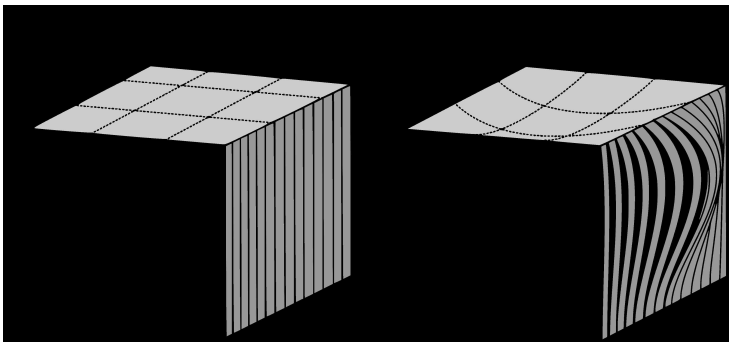

Figure 6.4: Visualization of lateral core sheet and face sheet members before and after buckling.

Furthermore, it will be assumed that the angle of rotation at the edge of the buckled face sheet is equal to the angle of rotation at the top edge of the adjacent core sheet, as shown in Figure 6.5. In other words, it is assumed that all adjacent core and face sheet members meet at an angle of 90 degrees throughout the deformation. Modeling the lateral core members as sets of vertical beams allows the rotationally constrained edges of the face plates to be modeled as though they are supported by torsional springs of constant stiffness, as shown in Figure 6.6. The stiffness of the torsional spring depends on both the geometry and boundary conditions of the lateral core members.

Figure 6.5: 2D schematic of interaction between lateral core members and face sheets during buckling.

The lateral core members require boundary conditions at their intersection with the top and bottom

face sheets. Due to the three-point-bending load, the top face sheets are in compression, while the bottom face sheets are in tension. In such a loading case, only the top face sheets in compression are prone to buckling. Once buckling occurs, the top sheets rotate by an angle θ as a result of the instability caused by the compressive loading. As the tensile stress in the bottom face sheet does not cause any instability, it will be assumed that the bottom face sheet does not undergo any out-of-plane deformation. As a result, the lateral core member can be modeled as though it is clamped at its bottom edge. At the top edge, the lateral core member is pinned in place, but is free to rotate.

Figure 6.5 shows two face sheet plates undergoing a buckling deformation. Due to the nature of the loading, the top face sheet plate marked by the solid line carries a slightly higher axial load, and will buckle before the one marked with the dashed line. Thus, the rotational constraint caused by the plate marked with the dashed line is neglected. The approach of ignoring rotational constraints posed by adjacent members on the verge of buckling is the same as the one taken by Valdevit et al. [15] when analyzing buckling in corrugated diamond prismatic structures. As only one face sheet and one core member contributes to the internal moment at their interface, it is apparent that the moment that causes the bending of the lateral core member will be equivalent to the moment that restrains the face sheet from buckling.

Figure 6.6: Loading and boundary conditions for face plate during buckling.

With the boundary conditions for the lateral core member in mind, the stiffness of the torsional spring employed in the face sheet model can be calculated by superimposing two loads on the infinitely thin beams that make up the lateral core member. As described before, the infinitely thin beams are clamped on one side and simply supported on the other. The goal is to determine proportionality between the angle of rotation of the simply supported end and the moment applied to that end. The two superposed loads are

a moment and a point force acting at the end of a cantilever beam, as shown in Figure 6.7. The magnitude of the point force is chosen so that it exactly balances the displacement caused by the applied moment, in accordance with the pinned/simply-supported boundary condition. For a cantilever beam subjected to a moment at its free end, the end point displacement, δ_M, and rotation, θ_M, are given by Beer and Johnston [24]:

$$\delta_M = \frac{ML^2}{2EI}, \tag{6.1}$$

$$\theta_M = \frac{ML}{EI}. \tag{6.2}$$

For a cantilever beam subjected to a force at its free end, the end point displacement, δ_F, and rotation, θ_F, are given by [24]:

$$\delta_F = \frac{-FL^3}{3EI}, \tag{6.3}$$

$$\theta_F = \frac{-FL^2}{2EI}. \tag{6.4}$$

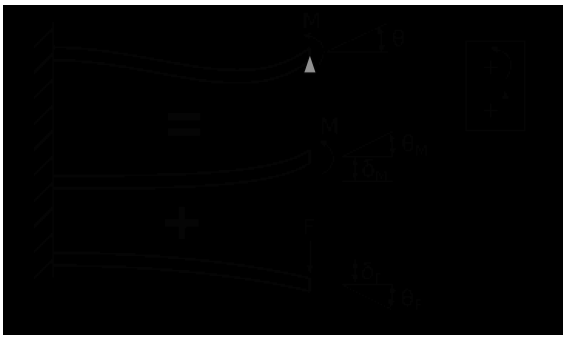

Figure 6.7: Cantilever beam deformations due to point force and moment loading.

Setting the total displacement at the end of the beam equal to zero yields:

$$\delta_M + \delta_F = \frac{ML^2}{2EI} - \frac{FL^3}{3EI} = 0,$$

and solving for F gives the relationship:

$$F = \frac{3M}{2L}. \tag{6.5}$$

Summing θ_M and θ_F, and using equation (6.5) for F allows the total angle at the end of the beam to be expressed:

$$\theta = \frac{ML}{EI} - \frac{\left(\frac{3M}{2L}\right) L^2}{2EI} = \frac{ML}{4EI}, \tag{6.6}$$

where I is the moment of inertia of the beam.

A constant, C, can be used represent the stiffness of the torsional spring acting on the face plate. Using equation (6.6) but expressing the moment on a per unit width basis leads to the following expression for C:

$$C = \frac{M'}{\theta} = \frac{4EI'}{L}, \tag{6.7}$$

where I' is the moment of inertia of the beam per unit width. For the honeycomb geometry, $I' = \frac{1}{12}t_c^3$, and $L = H_c$, so the stiffness of the torsional spring can be expressed:

$$C = \frac{Et_c^3}{3H_c}. \tag{6.8}$$

The governing equation for the buckling of a plate subjected to uniform compression on two sides is given by Timoshenko [22]:

$$\frac{\partial^4 \partial w}{\partial x^4} + 2\frac{\partial^4 w}{\partial x^2 \partial y^2} + \frac{\partial^4 \partial w}{\partial y^4} = \frac{-N_x}{D}\frac{\partial^2 w}{\partial x^2}, \tag{6.9}$$

where N_x is a force per unit length, and compression is defined as positive. D is the flexural rigidity of the plate:

$$D = \frac{Eh^3}{12\left(1-\nu^2\right)}, \tag{6.10}$$

where h is the thickness of the plate.

The loading conditions and dimensions of the rectangular plate are shown in Figure 6.8. The edges at $y = 0$ and $y = b$ are simply supported, while the edges at $x = \pm a/2$ are restrained by torsional springs. In addition, a uniform compressive force per unit length, N_x, is applied to the edges at $x = \pm a/2$. The coordinate axis has been placed so that the loading and boundary conditions of the plate are symmetric in the x-direction. This symmetry will later be used in order to simplify the solution of the problem. It is assumed that the out-of-plane displacement of the plate, w, can be expressed as a sine function:

$$w = f(x) \sin \frac{n\pi y}{b}. \tag{6.11}$$

In this expression $f(x)$ is a function of x only, and n is the number of half waves that form in the y direction when the plate buckles. The boundary conditions for the simply supported edges are:

$$w = 0 \text{ on } y = 0 \text{ and } y = b, \tag{6.12}$$

$$-D\left(\frac{\partial^2 w}{\partial y^2} + \nu \frac{\partial^2 w}{\partial x^2}\right) = 0 \text{ on } y = 0 \text{ and } y = b, \tag{6.13}$$

and equation (6.11) satisfies these boundary conditions.

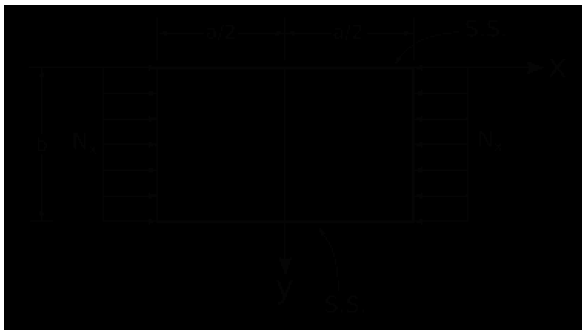

Figure 6.8: Dimensions of rectangular plate under uniform axial load.

Substituting equation (6.12) into (6.11) gives the following fourth order linear ordinary differential equation:

$$\frac{d^4 f}{dx^4} + \left[\frac{N_x}{D} - 2\frac{n^2\pi^2}{b^2}\right]\frac{d^2 f}{dx^2} + \frac{n^4\pi^4}{b^4} f(x) = 0. \tag{6.14}$$

The characteristic roots of equation (6.14) are:

$$\alpha = \sqrt{\frac{-N_x}{2D} + \frac{n^2\pi^2}{b^2} - \frac{\sqrt{N_x}\sqrt{b^2N_x - 4Dn^2\pi^2}}{2bD}}, \tag{6.15}$$

$$\beta = \sqrt{\frac{-N_x}{2D} + \frac{n^2\pi^2}{b^2} + \frac{\sqrt{N_x}\sqrt{b^2N_x - 4Dn^2\pi^2}}{2bD}}, \tag{6.16}$$

both with a multiplicity of 2.

For a square simply supported plate under a constant axial load, it has been by [22] that $N_x = 4\pi^2D/b^2$. The elastic supports on the plates analyzed in this section will increase the buckling load, so it can be stated that $N_x \geq 4\pi^2D/b^2$, or:

$$b^2N_x \geq 4\pi^2D. \tag{6.17}$$

This relation indicates that the last term in equations (6.15-6.16) will always be real, and will approach zero as the stiffness of the elastic restraint decreases.

As the plates being analyzed are square, it will also be assumed that only one half wave forms in the x and y directions during buckling, so $m = n = 1$. From equation (6.17), it becomes clear that $N_x/D \geq 4\pi^2/b^2$, and so the first term under the radical in α (6.15) and β (6.16) will always be greater in magnitude than the second term. As a result, it can be seen that α will always be imaginary.

In order to determine whether β is real or imaginary, a plate with clamped boundary conditions along the loading edges is considered. While very weak torsional springs can be modeled as simple supports, the strongest possible spring can be modeled with a clamped boundary condition. For a plate where the loaded edges are clamped and the other two edges are simply supported, it has been shown that $N_x = 6.74\pi^2D/b^2$ [22]. Substituting this relation into the expression for β (6.16) and setting $n = 1$ yields:

$$\begin{aligned}\beta_{clamped} &= \sqrt{\frac{-6.74\pi^2}{2b^2} + \frac{\pi^2}{b^2} + \frac{\sqrt{\frac{6.74^2\pi^4D^2}{b^2} - \frac{4(6.74)\pi^4D^2}{b^2}}}{2bD}} \\ &= \sqrt{(-2.37)\frac{\pi^2}{b^2} + \frac{\sqrt{6.74^2 - (4)6.74}}{2}\frac{\pi^2}{b^2}} = \sqrt{-0.221}\frac{\pi}{b}\end{aligned} \tag{6.18}$$

From (6.18), it is clear that if the torsional spring is very stiff, β is imaginary. In the case of a torsional spring with very low stiffness, the relation $N_x = 4\pi^2 D/b^2$ for a simply supported plate can be used in equation (6.16) to show that β is still imaginary. Because the torsional spring supported boundary conditions represent the cases between simply supported and clamped, then β must be imaginary for any spring stiffness and plate rigidity.

As both characteristic roots of equation (6.14) are imaginary, the general solution is:

$$f(x) = C_1 \cos \alpha x + C_2 \sin \alpha x + C_3 \cos \beta x + C_4 \sin \beta x. \tag{6.19}$$

Since it is assumed that the square plate buckles in one half wave in each direction, the symmetric torsional spring boundary conditions then cause $f(x)$ given by equation (6.11) to be an even function. As a result, $C_2 = C_4 = 0$, and the general solution to the governing equation is reduced to:

$$f(x) = A \cos \alpha x + B \cos \beta x. \tag{6.20}$$

Using the sign convention shown in Figure 6.9, the boundary conditions for the torsional spring supported edges are:

$$-D\left(\frac{\partial^2 w}{\partial y^2} + \nu \frac{\partial^2 w}{\partial x^2}\right) = -C\frac{\partial w}{\partial x} \text{ on } x = -a/2, \tag{6.21}$$

$$-D\left(\frac{\partial^2 w}{\partial y^2} + \nu \frac{\partial^2 w}{\partial x^2}\right) = C\frac{\partial w}{\partial x} \text{ on } x = a/2. \tag{6.22}$$

The term on the left hand side of equations (6.21) and (6.22) represents the moment applied to the boundary, C is the stiffness of the torsional spring, and $\frac{\partial w}{\partial x}$ is the angle of rotation of the edge. The term on the right hand side of equation (6.21) is negative because according to the sign convention, a positive angle of rotation at the left edge of the plate will result in a negative moment reaction. The term on the right hand side of equation (6.22) is positive because a positive angle at the right edge of the plate will be resisted by a positive moment reaction.

It will also be assumed that the torsional spring supported edges do not displace vertically in the z-

Figure 6.9: Sign convention for moments applied at the boundary of the loaded plate.

direction of Figure 6.3, so:

$$w = 0 \text{ on } x = -a/2 \text{ and } x = -a/2. \tag{6.23}$$

Applying a zero-displacement boundary condition for the edge at $x = a/2$ in equation (6.20),

$$A\cos\alpha x + B\cos\beta x = 0. \tag{6.24}$$

Applying boundary condition (6.22) to equation (6.20),

$$D\left[-\alpha^2 A\cos\frac{\alpha a}{2} - \beta^2 B\cos\frac{\beta a}{2}\right] + C\left[-\alpha A\sin\frac{\alpha a}{2} - \beta B\sin\frac{\beta a}{2}\right] = 0. \tag{6.25}$$

A non-zero solution for A and B can be found by setting the determinant of equations (6.24) and (6.25) equal to zero:

$$\cos\frac{\alpha a}{2}\left[-D\beta^2\cos\frac{\beta a}{2} - C\beta\sin\frac{\beta a}{2}\right] = \cos\frac{\beta a}{2}\left[-D\alpha^2\cos\frac{\alpha a}{2} - C\alpha\sin\frac{\alpha a}{2}\right]. \tag{6.26}$$

Dividing both sides by $\left(-\cos\frac{\alpha a}{2}\right)$ gives:

$$D\beta^2\cos\frac{\beta a}{2} + C\beta\sin\frac{\beta a}{2} = D\alpha^2\cos\frac{\beta a}{2} + C\alpha\tan\frac{\alpha a}{2}\cos\frac{\beta a}{2}. \tag{6.27}$$

Dividing through by $\left(-\cos\frac{\beta a}{2}\right)$ gives:

$$D\beta^2 + C\beta\tan\frac{\beta a}{2} = D\alpha^2 + C\alpha\tan\frac{\alpha a}{2}. \tag{6.28}$$

Recall that α (6.15) and β (6.15) are functions of the critical buckling load, N_x, and the plate geometry. Equation (6.28) can then be solved numerically along with equations (6.15) and (6.16) in order to determine the critical buckling load for any square plate with torsional spring stiffness, C, and flexural rigidity, D.

The non-dimensional buckling coefficient used in the the face buckling failure mode equations is defined as:

$$K_b = \frac{N_x b^2}{\pi^2 D}. \tag{6.29}$$

For a square plate that is restrained by torsional springs on the loaded edges and simply supported along the other two edges, the buckling coefficient depends on a single non-dimensional parameter, Ca/D. In this parameter, a is the side length of the plate, and $a = b$ because the plate is square. Figure 6.10 shows how the buckling coefficient, K_b, varies with Ca/D.

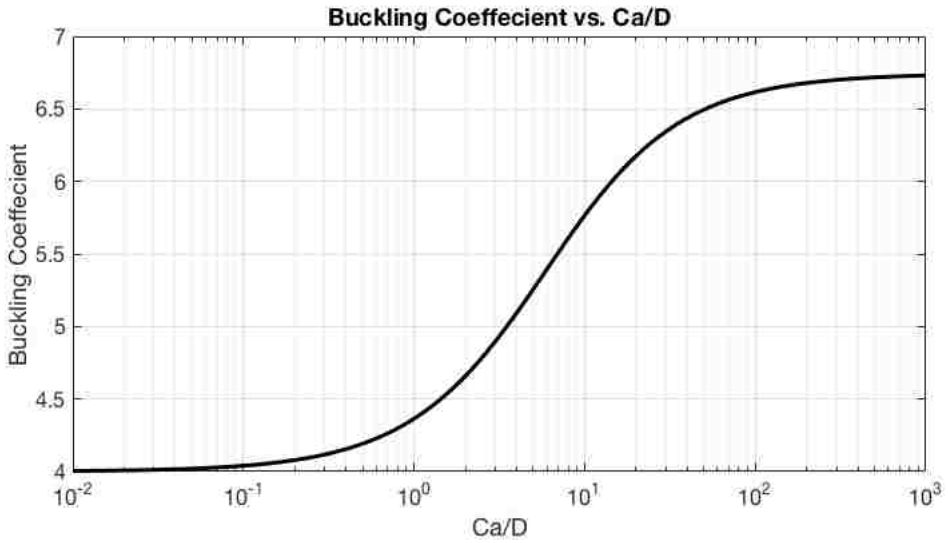

Figure 6.10: Relationship between the buckling coefficient and $\frac{Ca}{D}$.

This buckling coefficient relationship is in agreement with the results for the extreme boundary condition cases presented by Timoshenko [22]. For very low torsional spring stiffnesses, the buckling coefficient approaches the simply supported case value of 4.0. For high spring stiffness relative to plate flexural rigidity, the buckling coefficient approaches the clamped case value of 6.74.

In order to get a better sense of how the buckling coefficient changes with the geometry of the square

honeycomb structure, equations (6.8) and (6.10) can be used for C and D in the solution of equations (6.15), (6.16) and (6.28). In this case, the buckling coefficient is dependent on both the core to face sheet thickness ratio t_c/t_f, and the cell aspect ratio $\xi = L_c/H_c$. Results using these two non-dimensional parameters are shown in Figure 6.11.

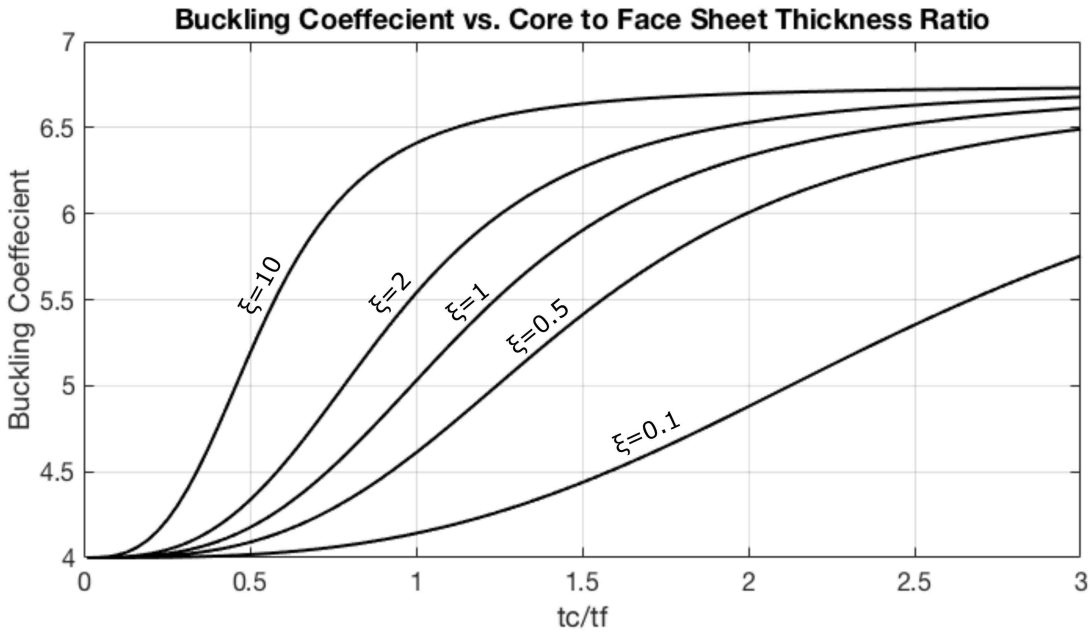

Figure 6.11: Buckling coefficient vs. core to face sheet thickness ratio (t_c/t_f) and cell aspect ratio ($\xi = L_c/H_c$).

The buckling coefficient increases as t_c/t_f increases, and also as L_c/H_c increases. The first trend is fairly straightforward. Holding all else constant, as the core member thickness, t_c, increases, the rotational spring constraining the loaded edges of the face sheet becomes stiffer, and the buckling coefficient therefore increases. For the second trend between the buckling coefficient and the cell aspect ratio: as the cell aspect ratio, L_c/H_c, increases, the height of the core, H_c, decreases relative to the face sheet cell width, L_c. As a result, the cantilever beams comprising the torsional springs decrease in length, and the stiffness of the torsional springs increases. As has already been shown, the spring stiffness increase will result in an increased buckling load. It is worth noting that as the cell aspect ratio, L_c/H_c, decreases, the model assumptions become more conservative. In particular, it was assumed that the core members making up the torsional springs have no stiffness with respect to bending moments in the y-direction in Figures 6.3 and 6.4. As the cell aspect ratio decreases however, stiffness with respect to bending in the y-direction clearly plays more of a role in the core plate's resistance to a moment applied at the top edge.

In the end, it is unclear whether a structure will actually perform better at higher cell aspect ratios, or whether this apparent trend is just a result of the model assumptions. What is clear, however, is that even with the proposed conservative approach, the buckling coefficient increases when the loaded edges of the face plates are modeled with torsional springs as opposed to simply supported edges. For example, based on Figure 6.11, the buckling coefficient for a cuboidal structure ($\xi = 1$) with equally thick core and face sheets ($t_c/t_f = 1$), will increase from 4 to 5 if rotationally constrained boundary conditions are employed. That increase in buckling coefficient corresponds to a 25% increase in the face buckling failure load, which is certainly significant within the scope of this work.

6.3 Additional Directions for Proposed Model Improvement and Perspectives for Future Work

This work has made several limiting assumptions about the characteristics of the square honeycomb sandwich panel analyzed under three-point-bending loading. First of all, it was assumed that the sandwich panel is made of one material. With minimal additional complexity, the analytical models presented in this work could be extended to address panels with different core and face sheet material properties. Multi-material or composite sandwich structures are of interest for a variety of multifunctional applications [23, 27, 28]. Considering core and face sheets with different strengths, stiffnesses and densities would increase the number of design variables in the optimization, but may also lead to the identification of lighter or more efficient structures. It is also important to point out that only a single loading direction was considered in this work. The Euler-Bernoulli "coupled" models proposed in this work cannot be easily extended to different loading directions, because the panel could no longer be treated as a beam of constant cross-section. In considering different loading directions, the optimal analytical model geometries presented in this work could at least be used as starting points for further finite element analysis and fine-tuning.

This work has also assumed that the first instance of yielding or buckling in the face or core of the structure determines when failure has occurred. Although conservative, these failure criteria may not be of interest to all designers, because plates often have post-buckling strength and are able to carry additional loads after they have buckled. Future work could be carried out to extend the model derivations to account for the post-buckling behavior of face and core members of the structure. The effective width method,

first proposed by von Karman in 1932, and later explored by Hu et al. [29], is most commonly used to evaluate the post-buckling strength of plates. Further steps could also be taken in modeling the rotational constraints on the edges of the face and core plates undergoing buckling. Finally, coupling of the failure modes could be considered. It would be very difficult to construct such a model in an analytical sense, but a broad parametric study could be conducted in order to determine tuning factors that penalize structures with multiple active failure modes in a multi-objective optimization scheme.

Lastly, this work could also be strengthened through experimental validation. To validate the work, experimental results for a broad range of square honeycomb geometries would need to be obtained. Several aspects of the physical model, such as the strength of the braze joints and higher order loading effects that have not been explored by the analytical models or the finite element studies presented, would need to be considered. These effects may prove to be significant when the structure is tested experimentally.

Chapter 7

Conclusions

This work has compared the traditional decoupled model for a square honeycomb structure under three-point-bending to a proposed simplified Euler-Bernoulli "coupled" modeling approach. Both models are useful for identifying near-optimal designs that could be refined by more detailed finite element analysis. In the cases considered, the proposed analytical model provides solutions that are closer to optimal geometries identified by finite element parametric study results.

Both the failure maps and optimal geometry plots presented in this work can be used by designers in selecting near-optimal geometries for further FEA refinement. The constant weight failure maps in conjunction with the predicted load contour level sets can be used to understand how changing the geometry of a structure affects its likelihood of initiating different failure mechanisms. The multi-objective optimization scheme presented in this work can be utilized to determine the range of geometries that are optimal for a prescribed load. Furthermore, the multi-objective optimization scheme could be tailored by a designer to weight design factors according to his or her needs. For example, manufacturing cost terms could be included in the multi-objective scheme.

This work has shown that the proposed simplified Euler-Bernoulli-based "coupled" analytical model yields more accurate optimal geometries than the traditional decoupled model, when failure is defined as the first instance of yielding or buckling in the face or core of the honeycomb structure. Two key design guidelines result from the analysis in Chapters 3-6. Both guidelines can be used in combination with the dominant failure mode plots presented in Section 3.5 and the optimization scheme described in Section 5.1 to help designers rapidly identify near-optimal geometries for a given application.

The first guideline is to remain close to cuboidal cell structures: the optimal structure usually has a cell aspect ratio L_c/H_c close to unity over a broad range of loading conditions (see Figure 2.1). By narrowing in on structures with aspect ratios near unity, a designer can speed up any necessary parametric studies and identify the near-optimal geometry more quickly. The second guideline is that when two geometries have the same weight and analytically predicted failure load, it is best to search for geometries that reduce the failure constraint activity levels of the non-dominant failure modes. Although the analytical models do not themselves account for the coupling of different failure modes, this feature can be somewhat moderated by the multi-objective optimization scheme presented in Chapter 5. A pseudo-failure mode coupling can be incorporated into the optimization scheme by penalizing structures in which multiple failure modes are active.

Appendices

Appendix A

Decoupled Model Derivation

The decoupled model assumes that the moment is entirely resisted by the face sheets, while the shear stress is resisted entirely by the core. It is also assumed that the normal and shear stresses are uniformly distributed across the face sheets and core respectively. Figure A.1 shows the stresses that act on a panel of unit cell width for the decoupled model.

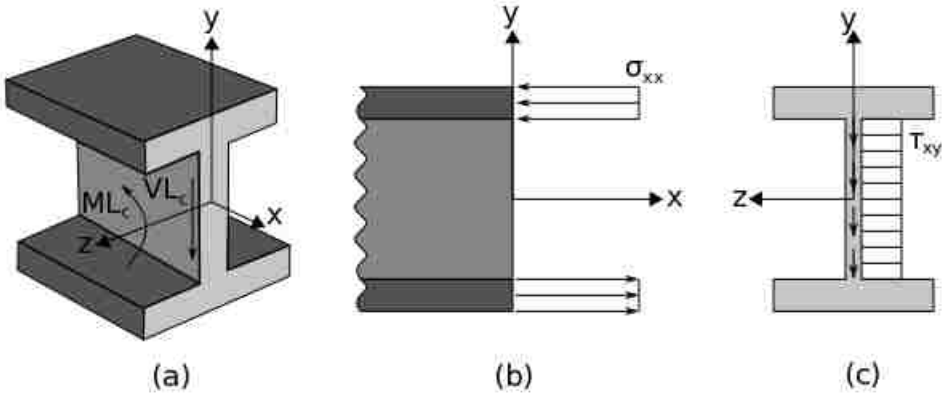

Figure A.1: Stress distribution in unit cell width panel for decoupled model.

The axial stress in the face sheets can be determined by summing the moments around the horizontal axis running through the midpoint of the core. Figure A.2 shows how the evenly distributed axial stress on each face sheet can be expressed as a point load acting in the middle of each face sheet. Equating the moment caused by the axial stress to the maximum internal bending moment on the panel yields the

following expression:

$$ML_c = 2\sigma(t_f L_c)\left(\frac{H_c + t_f}{2}\right). \tag{A.1}$$

Equation (A.1) can be re-arranged in order to give an expression for the axial stress in the face sheets:

$$\sigma_f = \frac{M}{t_f(H_c + t_f)}. \tag{A.2}$$

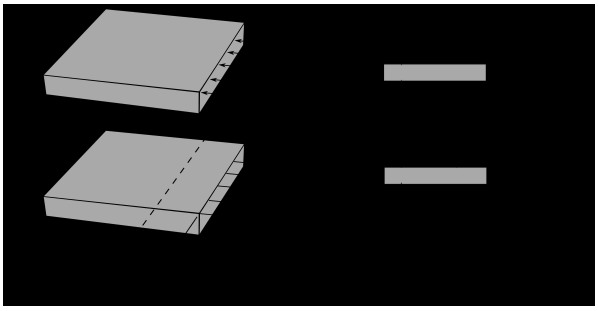

Figure A.2: Expressing the evenly distributed axial stress on the face sheets (left) as point loads (right).

The decoupled modeling approach assumes that the shear load is entirely resisted by the core, and thus there is no shear force in the face sheets. Furthermore, it is assumed that the shear load is distributed uniformly in the core. The magnitude of the shear load acting on a panel of unit cell width is VL_c. The shear stress in the core is calculated by dividing the shear load on the panel by the cross-sectional area of the core:

$$\tau_c = \frac{VL_c}{t_c H_c}. \tag{A.3}$$

The shear stress in the core given by equation (A.3) can be used in the von Mises yield criterion, equation (3.1), in order to determine the core yield criterion for the decoupled model. Note that since there is no axial stress in the core for the decoupled model, the value of σ in equation (3.1) is set to zero. The resulting yield criterion becomes:

$$3\left(\frac{VL_c}{t_c H_c}\right)^2 \leq \sigma_Y^2. \tag{A.4}$$

Taking the square root of both sides, using Hooke's law to set $\sigma_Y = E\epsilon_Y$, dividing through by $E\epsilon_Y$, and

using equation (2.11) for V, the core yield criterion becomes:

$$\Pi \frac{\sqrt{3} L_c l}{\epsilon_Y t_c H_c} \leq 1. \tag{A.5}$$

Since there is only the one axial stress component in the face sheets, face sheet yielding will occur when the stress exceeds the yield stress. Using the axial stress derived in equation (A.2), the yield criterion for the face sheets is:

$$\frac{M}{t_f (H_c + t_f)} \leq \sigma_Y. \tag{A.6}$$

Setting $\sigma_Y = E\epsilon_Y$, and dividing through by $E\epsilon_Y$, as well as using equation (2.12) for M allows the face yielding criterion to be expressed as:

$$\Pi \frac{l^2}{\epsilon_Y t_f (H_c + t_f)} \leq 1. \tag{A.7}$$

Equations (3.2) and (3.4) can be used in order to determine the face buckling criterion for the decoupled model. For a square honeycomb panel, the plates that make up the face sheet will be square, with a side length of L_c. For a simply supported square plate with a uniformly distributed axial load, the buckling coefficient is $K_b = 4$ [22]. For the decoupled model, there is no shear in the face sheets, so only the first term of equation (3.4) will be considered. Using the expression for axial stress in the face sheets derived in equation (3.2), the face buckling criterion can be expressed as:

$$\frac{M}{t_f (H_c + t_f)} \leq \frac{\pi^2 E}{3(1 - \nu^2)} \left(\frac{t_f}{L_c} \right)^2. \tag{A.8}$$

Using equation (2.12) for M and rearranging the terms, the face buckling criterion becomes:

$$\Pi \frac{3 l^2 (1 - \nu^2) L_c^2}{t_f^3 (H_c + t_f) \pi^2} \leq 1. \tag{A.9}$$

Equations (3.3) and (3.4) can be used in order to determine the core buckling criterion for the decoupled model. For a square honeycomb panel, the plates that make up the core members will be rectangular, with a height of H_c, and a width of L_c. For a simply supported rectangular plate under shear loading, the

buckling coefficient is given by Timoshenko [22]:

$$K_s = \begin{cases} 5.35 + 4\left(\frac{H_c}{L_c}\right)^2, & \text{if } L_c \geq H_c, \\ 5.35\left(\frac{H_c}{L_c}\right)^2 + 4, & \text{if } L_c < H_c. \end{cases} \tag{A.10}$$

For core buckling, $t = t_c$, and $b = H_c$. Since the decoupled model does not account for shear in the face sheets, only the second term of equation (3.4) is considered. Using the expression for the shear stress in the core (3.3), the core buckling criterion can be expressed:

$$\frac{V L_c}{t_c H_c} \leq K_s \frac{\pi^2 E}{12(1-\nu^2)} \left(\frac{t_c}{H_c}\right)^2. \tag{A.11}$$

Using equation (2.11) for V and rearranging, the final core buckling criterion becomes:

$$\Pi \frac{12 l L_c (1-\nu^2) H_c}{K_s t_c^3 \pi^2} \leq 1. \tag{A.12}$$

Appendix B

Python Job File and Post-Processing Script for Finite Element Model

```
from part import *
from material import *
from section import *
from assembly import *
from step import *
from interaction import *
from load import *
from mesh import *
from optimization import *
from job import *
from sketch import *
from visualization import *
from connectorBehavior import *
from abaqus import *
from abaqusConstants import *
from caeModules import *
from math import *
from odbAccess import *
from abaqusConstants import *

########################################################## ENTER DATA FOR MODEL ##########################################################

#Enter geometry parameters
l = 0.075
Hc = 0.11*l
Lc = 0.0647*l
tc = 0.0015*l
tf = 0.0036*l

l_extra = 1.3

TotalL = l*l_extra
```

```
#Enter material properties
E=70000000000.0
nu=0.30 #Poisson's ratio
YieldStress=490000000.0

#Enter additional simulation information
R=0.025 #Roller radius
maxdisp=-0.0027 #max load line displacement

myOdbName = 'SquareHComb

###############  CREATE MODEL ###############

#Define model
ModelName = myOdbName+'_Model'

mdb.Model(name=ModelName, modelType=STANDARD_EXPLICIT)

#Create base sketch (in XY plane)
IbeamSketch = beam.ConstrainedSketch(name='IbeamSketch', sheetSize=200.0)
IbeamSketch.Line(point1=(-Lc/2.0, Hc/2.0), point2=(Lc/2.0, Hc/2.0))
IbeamSketch.Line(point1=(-Lc/2.0, -Hc/2.0), point2=(Lc/2.0, -Hc/2.0))
IbeamSketch.Line(point1=(0.0, Hc/2.0), point2=(0.0, -Hc/2.0))

#Extrude base sketch
SquareHComb = beam.Part(name='SquareHComb', dimensionality=THREE_D,
        type=DEFORMABLE_BODY)
SquareHComb.BaseShellExtrude(sketch=IbeamSketch, depth=TotalL)
del IbeamSketch

#Create sketch for horizontal cell partitions on top surface of I beam:
#Define sketching surface
PartitionSketch = beam.ConstrainedSketch(name='PartitionSketch', sheetSize=200.0,
        transform=SquareHComb.MakeSketchTransform(sketchPlane= \
        SquareHComb.faces.findAt(coordinates=(Lc/2.0, Hc/2.0, Lc/2.0)),
        sketchPlaneSide=SIDE1,
        sketchUpEdge=SquareHComb.edges.findAt(coordinates=(0, Hc/2.0, Lc/2.0)),
        sketchOrientation=RIGHT,
        origin=(Lc/2.0, Hc/2.0, 0.0)))

SquareHComb.projectReferencesOntoSketch(filter=
        COPLANAR_EDGES, sketch=PartitionSketch)

#loop to create partitions
Zcoord = 0.0
while Zcoord <= TotalL:
        PartitionSketch.Line(point1=(0.0, -Zcoord), point2=(Lc, -Zcoord))
        Zcoord = Zcoord + Lc

#Extrude partitions
SquareHComb.ShellExtrude(depth=Hc, flipExtrudeDirection=OFF, sketch=PartitionSketch,
        sketchOrientation=RIGHT,
        sketchPlane=SquareHComb.faces.findAt(coordinates=(Lc/2.0, Hc/2.0, Lc/2.0)),
        sketchPlaneSide=SIDE1,
        sketchUpEdge=SquareHComb.edges.findAt(coordinates=(0, Hc/2.0, Lc/2.0)))
del PartitionSketch
```

```
#Partition bottom face where support contact will occur
if abs(l % Lc) > 0.00000001 and abs(l % Lc) < Lc - 0.00000001:
        MyDatum = SquareHComb.DatumPlaneByPrincipalPlane(principalPlane=XYPLANE, offset=l)
        SquareHComb.PartitionFaceByDatumPlane(datumPlane=SquareHComb.datums[MyDatum.id],
        faces=SquareHComb.faces.findAt(coordinates=(Lc/4.0, -Hc/2.0, l)))
        SquareHComb.PartitionFaceByDatumPlane(datumPlane=SquareHComb.datums[MyDatum.id],
        faces=SquareHComb.faces.findAt(coordinates=(-Lc/4.0, -Hc/2.0, l)))

#Partition structure to ignore stress concentration area
if abs(0.2*Hc % Lc) > 0.00000001 and abs(0.2*Hc % Lc) < Lc - 0.00000001:
        MyDatum2 = SquareHComb.DatumPlaneByPrincipalPlane(principalPlane=XYPLANE, offset=0.2*Hc)
        SquareHComb.PartitionFaceByDatumPlane(datumPlane=SquareHComb.datums[MyDatum2.id],
                faces=SquareHComb.faces.findAt(coordinates=(Lc/4.0, -Hc/2.0, 0.2*Hc)))
        SquareHComb.PartitionFaceByDatumPlane(datumPlane=SquareHComb.datums[MyDatum2.id],
                faces=SquareHComb.faces.findAt(coordinates=(-Lc/4.0, -Hc/2.0, 0.2*Hc)))
        SquareHComb.PartitionFaceByDatumPlane(datumPlane=SquareHComb.datums[MyDatum2.id],
                faces=SquareHComb.faces.findAt(coordinates=(Lc/4.0, Hc/2.0, 0.2*Hc)))
        SquareHComb.PartitionFaceByDatumPlane(datumPlane=SquareHComb.datums[MyDatum2.id],
                faces=SquareHComb.faces.findAt(coordinates=(-Lc/4.0, Hc/2.0, 0.2*Hc)))
        SquareHComb.PartitionFaceByDatumPlane(datumPlane=SquareHComb.datums[MyDatum2.id],
                faces=SquareHComb.faces.findAt(coordinates=(0.0, 0.0, 0.2*Hc)))

#Mesh Part
#Create mesh so that elements are close to square, with 20 elements along the shortest edge (default is 20)

#MeshSize = min(Hc,Lc)/MeshList[I]
MeshSize = min(Hc,Lc)/20.0

#Seed part
SquareHComb.seedPart(size=MeshSize, deviationFactor=0.1, minSizeFactor=0.1)
SquareHComb.generateMesh()

#Create sets
SquareHComb.Set(faces=SquareHComb.faces.getByBoundingBox(-Lc,-Hc,-Lc/2.0,Lc,Hc,0.0), name='HalfCore')
SquareHComb.Set(faces=SquareHComb.faces.getByBoundingBox(-Lc/2.0,0.0,0.0,Lc/2.0,Hc/2.0,TotalL), name='TopFace')
SquareHComb.Set(faces=SquareHComb.faces.getByBoundingBox(-Lc/2.0,-Hc/2.0,0.0,Lc/2.0,0.0,TotalL), name='BottomFace')
SquareHComb.Set(faces=SquareHComb.faces.getByBoundingBox(-Lc,-Hc,-1.0,Lc,Hc,TotalL+1.0), name='All')
SquareHComb.SetByBoolean(name='Face', sets=(SquareHComb.sets['BottomFace'], SquareHComb.sets['TopFace']))
SquareHComb.SetByBoolean(name='Core', operation=DIFFERENCE, sets=(SquareHComb.sets['All'],
        SquareHComb.sets['Face'],SquareHComb.sets['HalfCore']))
del SquareHComb.sets['TopFace']
del SquareHComb.sets['BottomFace']
del SquareHComb.sets['All']

#Create sections
beam.HomogeneousShellSection(name='FaceSheet', material='Material-1', thickness=tf, integrationRule=SIMPSON, numIntPts=5)
beam.HomogeneousShellSection(name='HalfCore', material='Material-1', thickness=tc/2.0, integrationRule=SIMPSON, numIntPts=5)
beam.HomogeneousShellSection(name='Core', material='Material-1', thickness=tc, integrationRule=SIMPSON, numIntPts=5)

#Assign sections to sets
SquareHComb.SectionAssignment(region=SquareHComb.sets['Face'], sectionName='FaceSheet', offset=0.0,
        offsetType=MIDDLE_SURFACE, offsetField='', thicknessAssignment=FROM_SECTION)
SquareHComb.SectionAssignment(region=SquareHComb.sets['HalfCore'], sectionName='HalfCore', offset=0.0,
        offsetType=MIDDLE_SURFACE, offsetField='', thicknessAssignment=FROM_SECTION)
SquareHComb.SectionAssignment(region=SquareHComb.sets['Core'], sectionName='Core', offset=0.0,
```

```
        offsetType=MIDDLE_SURFACE, offsetField='', thicknessAssignment=FROM_SECTION)

#Create Material
beam.Material(name='Material-1')
beam.materials['Material-1'].Elastic(table=((E, nu),))
beam.materials['Material-1'].Plastic(table=((YieldStress, 0.0),))

#Create contact surface
SupportSketch = beam.ConstrainedSketch(name='__profile__', sheetSize=200.0)
SupportSketch.Arc3Points(point1=(-(R/2.0)*(2.0**(0.5)), (R/2.0)*(2.0**(0.5))),
        point2=((R/2.0)*(2.0**(0.5)), (R/2.0)*(2.0**(0.5))), point3=(0.0, R))
Support = beam.Part(name='Support', dimensionality=THREE_D, type=ANALYTIC_RIGID_SURFACE)
Support.AnalyticRigidSurfExtrude(sketch=SupportSketch, depth=Lc*2.0)
del beam.sketches['__profile__']
XYDatum = Support.DatumPlaneByPrincipalPlane(principalPlane=XYPLANE, offset=0.0)
YZDatum = Support.DatumPlaneByPrincipalPlane(principalPlane=YZPLANE, offset=0.0)
Support.PartitionFaceByDatumPlane(datumPlane=Support.datums[XYDatum.id], faces=Support.faces.findAt(coordinates=(0.0,R,0.0)))
Support.PartitionFaceByDatumPlane(datumPlane=Support.datums[YZDatum.id], faces=Support.faces.findAt(coordinates=(0.0,R,Lc/2.0)))
Support.PartitionFaceByDatumPlane(datumPlane=Support.datums[YZDatum.id], faces=Support.faces.findAt(coordinates=(0.0,R,-Lc/2.0)))
RP1 = Support.ReferencePoint(point=Support.vertices[1])
Support.Set(referencePoints=(Support.referencePoints[RP1.id],), name='Fixed')

#Create assembly
Assembly = beam.rootAssembly
Assembly.DatumCsysByDefault(CARTESIAN)
HCombIns = Assembly.Instance(name='SquareHComb-1',part=SquareHComb, dependent=ON)
SupportIns = Assembly.Instance(name='Support-1',part=Support, dependent=ON)
Assembly.EdgeToEdge(movableAxis=SupportIns.edges.findAt(coordinates=(0.0, R, Lc/4.0)),
        fixedAxis=HCombIns.edges.findAt(coordinates=(Lc/8.0, -Hc/2.0, 1)), flip=ON)
Assembly.FaceToFace(movablePlane=SupportIns.datums[XYDatum.id],
        fixedPlane=HCombIns.faces.findAt(coordinates=(0.0, 0.0, 1)), flip=OFF, clearance=0.0)

#Create step
beam.StaticStep(name='Displacement', previous='Initial', description='Displacement at load line',
        initialInc=0.02, maxInc=0.02, nlgeom=ON)

#Create interaction property
#session.viewports['Viewport: 1'].assemblyDisplay.setValues(interactions=ON, constraints=ON, connectors=ON,
        engineeringFeatures=ON, adaptiveMeshConstraints=OFF)
beam.ContactProperty('Contact')

beam.interactionProperties['Contact'].TangentialBehavior(formulation=PENALTY, directionality=ISOTROPIC, slipRateDependency=OFF,
        pressureDependency=OFF, temperatureDependency=OFF, dependencies=0, table=((0.02, ), ), shearStressLimit=None,
        maximumElasticSlip=FRACTION, fraction=0.005, elasticSlipStiffness=None)

beam.interactionProperties['Contact'].NormalBehavior(pressureOverclosure=HARD, allowSeparation=ON, constraintEnforcementMethod=DEFAULT)

#Create interaction
session.viewports['Viewport: 1'].assemblyDisplay.setValues(step='Displacement')

slavesurf=regionToolset.Region(side1Faces=HCombIns.faces.getByBoundingBox(-Lc/2.0,-Hc,1-2.0*Lc,Lc/2,0.0,1+2.0*Lc))
mastersurf=regionToolset.Region(side1Faces=SupportIns.faces.getByBoundingBox(-Lc,-Hc/2.0-R,1-R,Lc,0.0,1+R))

beam.SurfaceToSurfaceContactStd(name='SupContact', createStepName='Displacement', master=mastersurf,
        slave=slavesurf, sliding=FINITE, thickness=OFF, interactionProperty='Contact',
        adjustMethod=NONE, initialClearance=OMIT, datumAxis=None, clearanceRegion=None)
```

```
#Create BC's
SupportRP = Assembly.Set(referencePoints=(SupportIns.referencePoints[RP1.id], ), name='SupportRP')
beam.DisplacementBC(name='FixSupport', createStepName='Displacement', region=SupportRP, u1=0.0, u2=0.0, u3=0.0,
        ur1=0.0, ur2=0.0, ur3=0.0, amplitude=UNSET, fixed=OFF, distributionType=UNIFORM, fieldName='', localCsys=None)

beam.ZsymmBC(name='Zsymm', createStepName='Displacement', region=Assembly.sets['SquareHComb-1.HalfCore'], localCsys=None)

Assembly.Set(edges=HCombIns.edges.getByBoundingBox(Lc/4.0, -Hc, 0.0, Lc, Hc, TotalL), name='HCombSide1')
beam.XsymmBC(name='Xsymm', createStepName='Displacement', region=Assembly.sets['HCombSide1'], localCsys=None)

Assembly.Set(edges=HCombIns.edges.getByBoundingBox(-Lc, Hc/4.0, -Lc/2.0, Lc, Hc, 0.0), name='LoadLine')
beam.DisplacementBC(name='LoadDisp', createStepName='Displacement', region=Assembly.sets['LoadLine'], u1=UNSET, u2=maxdisp,
        u3=UNSET, ur1=UNSET, ur2=UNSET, ur3=UNSET, amplitude=UNSET, fixed=OFF, distributionType=UNIFORM, fieldName='', localCsys=None)

Assembly.Set(edges=HCombIns.edges.getByBoundingBox(-Lc, -Hc, 0.0, -Lc/4.0, Hc, TotalL), name='HCombSide2')

GPE_RP = Assembly.ReferencePoint(point=(-Lc/2.0, Hc, 0.0))
Assembly.Set(referencePoints=(Assembly.referencePoints[GPE_RP.id], ), name='GPE_RP')
beam.Equation(name='Generalized_Plane_Strain', terms=((-1.0, 'HCombSide2', 1), (1.0, 'GPE_RP', 1)))

#Create additional sets for post processing
SquareHComb.Set(faces=SquareHComb.faces.getByBoundingBox(-Lc/4.0, -Hc, 0.2*Hc, Lc/4.0, Hc, 0.2*Hc+2*Lc), name='PP_YieldLoadCore')
SquareHComb.Set(faces=SquareHComb.faces.getByBoundingBox(-Lc/4.0, -Hc, 0.0, Lc/4.0, Hc, Lc), name='PP_BuckleLoadCore')
SquareHComb.Set(faces=SquareHComb.faces.getByBoundingBox(-Lc,-Hc,-Lc/2.0,Lc,Hc,0.0), name='PP_HalfCore')
SquareHComb.Set(faces=SquareHComb.faces.getByBoundingBox(-Lc/2.0,0.0,0.2*Hc,Lc/2.0,Hc/2.0,0.2*Hc+2*Lc), name='PP_YieldLoadTopFace')
SquareHComb.Set(faces=SquareHComb.faces.getByBoundingBox(-Lc/2.0,0.0,0.0,Lc/2.0,Hc/2.0,Lc), name='PP_BuckleLoadTopFace')
SquareHComb.Set(faces=SquareHComb.faces.getByBoundingBox(-Lc/2.0,-Hc/2.0,0.2*Hc,Lc/2.0,0.0,0.2*Hc+2*Lc), name='PP_YieldLoadBotFace')
SquareHComb.Set(faces=SquareHComb.faces.getByBoundingBox(-Lc/2.0,-Hc/2.0,1-2.0*Lc,Lc/2.0,Hc/2.0,1+2.0*Lc), name='PP_ContactRegion')
SquareHComb.Set(edges=SquareHComb.edges.getByBoundingBox(-Lc/2.0,0.0,-Lc/4.0,Lc/2.0,Hc,0.2*Hc), name='PP_LoadLineArea')

#Write .txt file containing specimine geometry
mySaveFileName = myOdbName + '_Geometry.txt'
mySaveFile = open(mySaveFileName,'w+')

newline = str(Hc) + '\n' + str(Lc) + '\n' + str(l) + '\n' + str(tf) + '\n' + str(tc) + '\n' + str(maxdisp)
mySaveFile.writelines(newline)
mySaveFile.close()

##################################################### CREATE AND SUBMIT JOB ######################################################

#Create job
mdb.Job(name=myOdbName, model=ModelName, description='', type=ANALYSIS, atTime=None)

#Submit job and wait for completion before post processing
mdb.jobs[myOdbName].submit(consistencyChecking=OFF)
mdb.jobs[myOdbName].waitForCompletion()

##################################################### BEGIN POST PROCESSING ######################################################

#Open Odb
myOdb = openOdb(path=(myOdbName+'.odb'), readOnly = False)

#Create frame repository
frameRepository = myOdb.steps['Displacement'].frames
```

```
#Collect force vs. displacement data
ForceNode = myOdb.rootAssembly.instances['SUPPORT-1'].nodeSets['FIXED']
force=[]
displacement=[]
time=[]
for i in range(len(frameRepository)):
        fr = frameRepository[i]
        RF = fr.fieldOutputs['RF'].getSubset(region=ForceNode).values
        RF2 = RF[0].data[1]
        force.append(RF2)
        t=fr.frameValue
        time.append(t)
        disp = t*maxdisp*(-1.0)
        displacement.append(disp)

#Calculate slope for data points
SLOPE = [0.0,]
slope = 0.0
for i in range (1,len(force)):
        if ((displacement[i]-displacement[i-1]) != 0.0):
                slope = (force[i]-force[i-1])/(displacement[i]-displacement[i-1])
        SLOPE.append(slope)

#Determine data points in linear regime
linearPoints=[]
for i in range (len(SLOPE)):
        if (force[i] >= max(force)/15.0):
                if (abs((SLOPE[i]-SLOPE[i-1])/SLOPE[i]) <= 0.01) or linearPoints==[]:
                        linearPoints.append(i)
                else:
                        break

#Select first and last points of linear regime to define slope
Force1 = force[linearPoints[0]]
Disp1 = displacement[linearPoints[0]]
Force2 = force[linearPoints[-1]]
Disp2 = displacement[linearPoints[-1]]

if Disp1==Disp2:
        Disp1 = displacement[linearPoints[0]-1]
        Force1 = force[linearPoints[0]-1]

#Create list of projected displacements corresponding to forces in force list
Slope12 = (Force2-Force1)/(Disp2-Disp1)
ProjDisp = []
for i in range(len(force)):
        projdisp = (force[i]-Force1)/Slope12+Disp1
        ProjDisp.append(projdisp)

OffsetFrame = 0
SlopeFrame = 0

#Find first frame where there is a 2% offset from linearity
for i in range(len(force)):
        if (force[i] >= max(force)/10.0):
                if (abs((displacement[i]-ProjDisp[i])/displacement[i]) >= 0.02):
```

```
                        OffsetFrame = i
                        break

#Find first frame where there is a 10% change in slope
for i in range(len(force)):
        if (force[i] >= max(force)/10.0):
                if (abs((SLOPE[i]-Slope12)/Slope12) >= 0.1):
                        SlopeFrame = i
                        break

#Write force vs. displacement data to .txt file
mySaveFileName = myOdbName + '_ForceDisp.txt'
mySaveFile = open(mySaveFileName,'w+')
newline = str()
for i in range(len(force)):
        newline = newline + str(force[i]) + '\t\t' + str(displacement[i]) + '\n'
mySaveFile.writelines(newline)
mySaveFile.close()

#Check for yielding on top face by load line
##########################################################################################################################################
LoadTopFace = myOdb.rootAssembly.instances['SQUAREHCOMB-1'].elementSets['PP_YIELDLOADTOPFACE']
LoadTopFaceYield = 0
LoadTopFaceYieldFrame = 0

for i in range(len(frameRepository)):
        fr = frameRepository[i]
        s = fr.fieldOutputs['S'].getSubset(region=LoadTopFace, position=INTEGRATION_POINT, elementType='S4R').values
        for j in s:
                s11 = j.data[0]
                s22 = j.data[1]
                s33 = j.data[2]
                s12 = j.data[3]
                mis=(1.0/(sqrt(2.0))*sqrt((s11-s22)**2 + (s22-s33)**2 + (s33-s11)**2 + 6*(s12**2 + 0**2 + 0**2)))
                if (LoadTopFaceYield == 1):
                        break
                elif (mis >= 490000000.0):
                        LoadTopFaceYield = 1
                else:
                        continue
        if (LoadTopFaceYield == 1):
                LoadTopFaceYieldFrame = i
                break

#Check for yielding on bottom face by load line
##########################################################################################################################################
LoadBotFace = myOdb.rootAssembly.instances['SQUAREHCOMB-1'].elementSets['PP_YIELDLOADBOTFACE']
LoadBotFaceYield = 0
LoadBotFaceYieldFrame = 0

for i in range(len(frameRepository)):
        fr = frameRepository[i]
        s = fr.fieldOutputs['S'].getSubset(region=LoadBotFace, position=INTEGRATION_POINT, elementType='S4R').values
        for j in s:
                s11 = j.data[0]
                s22 = j.data[1]
```

```
                s33 = j.data[2]
                s12 = j.data[3]
                mis=(1.0/(sqrt(2.0))*sqrt((s11-s22)**2 + (s22-s33)**2 + (s33-s11)**2 + 6*(s12**2 + 0**2 + 0**2)))
                if (LoadBotFaceYield == 1):
                        break
                elif (mis >= 490000000.0):
                        LoadBotFaceYield = 1
                else:
                        continue
        if (LoadBotFaceYield == 1):
                LoadBotFaceYieldFrame = i
                break

if LoadBotFaceYieldFrame==0:
        LoadFaceYieldFrame=LoadTopFaceYieldFrame
elif LoadTopFaceYieldFrame==0:
        LoadFaceYieldFrame=LoadBotFaceYieldFrame
else:
        LoadFaceYieldFrame = min(LoadTopFaceYieldFrame,LoadBotFaceYieldFrame)

#Check for yielding at core
#############################################################################################################################
LoadCore = myOdb.rootAssembly.instances['SQUAREHCOMB-1'].elementSets['PP_YIELDLOADCORE']
LoadCoreYield = 0
LoadCoreYieldFrame = 0

for i in range(len(frameRepository)):
        fr = frameRepository[i]
        s = fr.fieldOutputs['S'].getSubset(region=LoadCore, position=INTEGRATION_POINT, elementType='S4R').values
        for j in s:
                s11 = j.data[0]
                s22 = j.data[1]
                s33 = j.data[2]
                s12 = j.data[3]
                mis=(1.0/(sqrt(2.0))*sqrt((s11-s22)**2 + (s22-s33)**2 + (s33-s11)**2 + 6*(s12**2 + 0**2 + 0**2)))
                if (LoadCoreYield == 1):
                        break
                elif (mis >= 490000000.0):
                        LoadCoreYield = 1
                else:
                        continue
        if (LoadCoreYield == 1):
                LoadCoreYieldFrame = i
                break

#Check for core buckling [normalized by plate thickness]
#############################################################################################################################
BuckleLoadCore = myOdb.rootAssembly.instances['SQUAREHCOMB-1'].nodeSets['PP_BUCKLELOADCORE']
LoadCoreBuckle = 0
LoadCoreBuckleFrame = 0
unorm = 0

for i in range(len(frameRepository)):
        fr = frameRepository[i]
        u = fr.fieldOutputs['U'].getSubset(region=BuckleLoadCore).values
        for j in u:
```

```
                u1 = j.data[0]
                u2 = j.data[1]
                u3 = j.data[2]
                unorm = u1
                if (LoadCoreBuckle == 1):
                        break
                elif (abs(unorm) >= tc/10.0):
                        LoadCoreBuckle = 1
                else:
                        continue
        if (LoadCoreBuckle == 1):
                LoadCoreBuckleFrame = i
                break

#Check for face buckling [normalized by plate thickness]
#############################################################################################################################################
LoadTopFace = myOdb.rootAssembly.instances['SQUAREHCOMB-1'].nodeSets['PP_BUCKLELOADTOPFACE']
LoadTopFaceBuckle = 0
LoadTopFaceBuckleFrame = 0
LoadTopFaceBuckleFrame1 = 0
LoadTopFaceBuckleFrame2 = 0
unorm = 0.0
maxunorm = -10.0
minunorm = 10.0
node1 = 0
node2 = 0
FaceBuckleDisp = []

fr = frameRepository[-1]
u = fr.fieldOutputs['U'].getSubset(region=LoadTopFace).values
for j in u:
        u1 = j.data[0]
        u2 = j.data[1]
        u3 = j.data[2]
        unorm = u2
        if (unorm > maxunorm):
                maxunorm = unorm
                node1 = j.nodeLabel
        if (unorm < minunorm):
                minunorm = unorm
                node2 = j.nodeLabel
        else:
                continue

for i in range(len(frameRepository)):
        fr = frameRepository[i]
        u = fr.fieldOutputs['U'].getSubset(region=LoadTopFace).values
        for j in u:
                if (j.nodeLabel == node1):
                        u1 = j.data[0]
                        u2 = j.data[1]
                        u3 = j.data[2]
                        FaceBuckleDisp.append(u2)

#Calculate slope for data points
SLOPE = [0.0,]
```

```
slope = 0.0
for i in range (1,len(FaceBuckleDisp)):
        if ((time[i]-time[i-1]) != 0.0):
                slope = (FaceBuckleDisp[i]-FaceBuckleDisp[i-1])/(time[i]-time[i-1])
        SLOPE.append(slope)

#Determine data points in linear regime
linearPoints=[]
for i in range (len(SLOPE)):
        if (force[i] >= max(force)/15.0):
                if (abs((SLOPE[i]-SLOPE[i-1])/SLOPE[i]) <= 0.01) or linearPoints==[]:
                        linearPoints.append(i)
                else:
                        break

#Select two points to define linear regime
FaceBuckleDisp1 = FaceBuckleDisp[linearPoints[0]]
time1 = time[linearPoints[0]]
FaceBuckleDisp2 = FaceBuckleDisp[linearPoints[-1]]
time2 = time[linearPoints[-1]]

ScaledFaceBuckleDisp = []
Slope12 = (FaceBuckleDisp2-FaceBuckleDisp1)/(time2-time1)
for i in range(len(FaceBuckleDisp)):
        scaledDisp = Slope12*(time2-time[i])+FaceBuckleDisp[i]-FaceBuckleDisp2
        ScaledFaceBuckleDisp.append(scaledDisp)

for i in range(len(ScaledFaceBuckleDisp)):
        if (ScaledFaceBuckleDisp[i] >= tf/10.0):
                LoadTopFaceBuckleFrame1 = i
                break

FaceBuckleDisp = []
for i in range(len(frameRepository)):
        fr = frameRepository[i]
        u = fr.fieldOutputs['U'].getSubset(region=LoadTopFace).values
        for j in u:
                if (j.nodeLabel == node2):
                        u1 = j.data[0]
                        u2 = j.data[1]
                        u3 = j.data[2]
                        FaceBuckleDisp.append(u2)

#Calculate slope for data points
SLOPE = [0.0,]
slope = 0.0
for i in range (1,len(FaceBuckleDisp)):
        if ((time[i]-time[i-1]) != 0.0):
                slope = (FaceBuckleDisp[i]-FaceBuckleDisp[i-1])/(time[i]-time[i-1])
        SLOPE.append(slope)

#Determine data points in linear regime
linearPoints=[]
for i in range (len(SLOPE)):
        if (force[i] >= max(force)/15.0):
                if (abs((SLOPE[i]-SLOPE[i-1])/SLOPE[i]) <= 0.01) or linearPoints==[]:
```

```
                        linearPoints.append(i)
                else:
                        break

#Select two points to define linear regime
FaceBuckleDisp1 = FaceBuckleDisp[linearPoints[0]]
time1 = time[linearPoints[0]]
FaceBuckleDisp2 = FaceBuckleDisp[linearPoints[-1]]
time2 = time[linearPoints[-1]]

ScaledFaceBuckleDisp = []
Slope12 = (FaceBuckleDisp2-FaceBuckleDisp1)/(time2-time1)
for i in range(len(FaceBuckleDisp)):
        scaledDisp = Slope12*(time2-time[i])+FaceBuckleDisp[i]-FaceBuckleDisp2
        ScaledFaceBuckleDisp.append(scaledDisp)

for i in range(len(ScaledFaceBuckleDisp)):
        if (ScaledFaceBuckleDisp[i] >= tf/10.0):
                LoadTopFaceBuckleFrame2 = i
                break

if LoadTopFaceBuckleFrame1==0:
        LoadTopFaceBuckleFrame=LoadTopFaceBuckleFrame2
elif LoadTopFaceBuckleFrame2==0:
        LoadTopFaceBuckleFrame=LoadTopFaceBuckleFrame1
else:
        LoadTopFaceBuckleFrame = min(LoadTopFaceBuckleFrame1,LoadTopFaceBuckleFrame2)
```

Bibliography

[1] H. N. Wadley, "Multifunctional periodic cellular metals," *Philosophical Transactions of the Royal Society of London A: Mathematical, Physical and Engineering Sciences*, vol. 364, no. 1838, pp. 31–68, 2006.

[2] N. Wicks and J. W. Hutchinson, "Optimal truss plates," *International Journal of Solids and Structures*, vol. 38, no. 30, pp. 5165–5183, 2001.

[3] H. Rathbun, F. Zok, and A. Evans, "Strength optimization of metallic sandwich panels subject to bending," *International journal of solids and structures*, vol. 42, no. 26, pp. 6643–6661, 2005.

[4] N. Wicks and J. W. Hutchinson, "Performance of sandwich plates with truss cores," *Mechanics of Materials*, vol. 36, no. 8, pp. 739–751, 2004.

[5] H. Rathbun, D. Radford, Z. Xue, M. He, J. Yang, V. Deshpande, N. Fleck, J. Hutchinson, F. Zok, and A. Evans, "Performance of metallic honeycomb-core sandwich beams under shock loading," *International Journal of Solids and Structures*, vol. 43, no. 6, pp. 1746–1763, 2006.

[6] D. J. Sypeck and H. N. Wadley, "Cellular metal truss core sandwich structures," *Advanced Engineering Materials*, vol. 4, no. 10, pp. 759–764, 2002.

[7] H. N. Wadley, N. A. Fleck, and A. G. Evans, "Fabrication and structural performance of periodic cellular metal sandwich structures," *Composites Science and Technology*, vol. 63, no. 16, pp. 2331–2343, 2003.

[8] F. Cote, V. Deshpande, N. Fleck, and A. Evans, "The out-of-plane compressive behavior of metallic honeycombs," *Materials Science and Engineering: A*, vol. 380, no. 1, pp. 272–280, 2004.

[9] F. Cote, V. Deshpande, and N. Fleck, "The shear response of metallic square honeycombs," *Journal of Mechanics of Materials and Structures*, vol. 1, no. 7, pp. 1281–1299, 2006.

[10] B. G. Compton and J. A. Lewis, "3d-printing of lightweight cellular composites," *Advanced materials*, vol. 26, no. 34, pp. 5930–5935, 2014.

[11] C. B. Williams, J. K. Cochran, and D. W. Rosen, "Additive manufacturing of metallic cellular materials via three-dimensional printing," *The International Journal of Advanced Manufacturing Technology*, vol. 53, no. 1, pp. 231–239, 2011.

[12] P. Zhang, J. Toman, Y. Yu, E. Biyikli, M. Kirca, M. Chmielus, and A. C. To, "Efficient design-optimization of variable-density hexagonal cellular structure by additive manufacturing: theory and validation," *Journal of Manufacturing Science and Engineering*, vol. 137, no. 2, p. 021004, 2015.

[13] M. K. Ravari, M. Kadkhodaei, M. Badrossamay, and R. Rezaei, "Numerical investigation on mechanical properties of cellular lattice structures fabricated by fused deposition modeling," *International Journal of Mechanical Sciences*, vol. 88, pp. 154–161, 2014.

[14] A. G. Evans, J. W. Hutchinson, N. A. Fleck, M. Ashby, and H. Wadley, "The topological design of multifunctional cellular metals," *Progress in Materials Science*, vol. 46, no. 3, pp. 309–327, 2001.

[15] L. Valdevit, J. W. Hutchinson, and A. G. Evans, "Structurally optimized sandwich panels with prismatic cores," *International Journal of Solids and Structures*, vol. 41, no. 18, pp. 5105–5124, 2004.

[16] F. W. Zok, H. Rathbun, M. He, E. Ferri, C. Mercer, R. M. McMeeking, and A. G. Evans, "Structural performance of metallic sandwich panels with square honeycomb cores," *Philosophical Magazine*, vol. 85, no. 26-27, pp. 3207–3234, 2005.

[17] A. Petras and M. Sutcliffe, "Indentation failure analysis of sandwich beams," *Composite Structures*, vol. 50, no. 3, pp. 311–318, 2000.

[18] M. F. Ashby, T. Evans, N. A. Fleck, J. Hutchinson, H. Wadley, and L. Gibson, *Metal foams: a design guide*. Elsevier, 2000.

[19] J. Guedes and N. Kikuchi, "Preprocessing and postprocessing for materials based on the homogenization method with adaptive finite element methods," *Computer methods in applied mechanics and engineering*, vol. 83, no. 2, pp. 143–198, 1990.

[20] Z. Xue and J. W. Hutchinson, "Crush dynamics of square honeycomb sandwich cores," *International Journal for Numerical Methods in Engineering*, vol. 65, no. 13, pp. 2221–2245, 2006.

[21] A. Catapano and M. Montemurro, "A multi-scale approach for the optimum design of sandwich plates with honeycomb core. part i: homogenisation of core properties," *Composite Structures*, vol. 118, pp. 664–676, 2014.

[22] S. P. Timoshenko and J. M. Gere, *Theory of elastic stability*. Courier Corporation, 2009.

[23] G. A. Howard, "Analysis and design of structural sandwich panels," 1969.

[24] F. P. Beer, E. R. Johnston, and J. T. DeWolf, "Mechanics of materials," *MacGraw-Hill Engineering Series,*, 1992.

[25] A. Petras and M. Sutcliffe, "Failure mode maps for honeycomb sandwich panels," *Composite structures*, vol. 44, no. 4, pp. 237–252, 1999.

[26] "C393: Standard test method for core shear propoerties of sandwich constrcution by beam flexure," ASTM International, Tech. Rep., April 2016.

[27] L. J. Gibson and M. F. Ashby, *Cellular solids: structure and properties*. Cambridge university press, 1999.

[28] F. Cã, B. Russell, V. Deshpande, N. Fleck *et al.*, "The through-thickness compressive strength of a composite sandwich panel with a hierarchical square honeycomb sandwich core," *Journal of Applied Mechanics*, vol. 76, no. 6, p. 061004, 2009.

[29] P. C. Hu, E. E. Lundqui, and S. Batdorf, "Effect of small deviations from flatness on effective width and buckling of," 1946.

Biography

Ziv Arzt received his B.S. and M.S. degrees in mechanical engineering from Lehigh University in 2016 and 2017, respectively. Ziv won the Elisha P. Wilbur scholarship prize at Lehigh in 2014, and he received the Ferdinand P. Beer award for excellence in solid mechanics as an undergraduate student at Lehigh in 2016. Ziv is currently working as a design engineer for Ingersoll Rand.